UNIVERSITÉ DU LUXEMBOURG

PhD-FSTC-2018-33
The Faculty of Sciences, Technology and Communication

DISSERTATION

Defence held on 20/04/2018 in Aachen

to obtain the degree of

DOCTEUR DE L'UNIVERSITÉ DU LUXEMBOURG

EN SCIENCES DE L'INGÉNIEUR

by

Christoph SCHOPP
Born on 23 July 1982 in Eschweiler (Germany)

CHARACTERIZATION AND MULTI-PHYSICAL ANALYSIS OF RF-DRIVEN MICROWAVE PLASMA APPLICATIONS FROM 1.3 TO 3.5 GHZ

Dissertation defence committee

Prof. Dr. Rony Snyders, dissertation supervisor
Professor, Université de Mons

Prof. Dr.-Ing. Holger Heuermann
Professor, Aachen University of Applied Sciences

Prof. Dr.-Ing. Jean-Régis Hadji-Minaglou, Chairman
Professor, Université du Luxembourg

Dr. Lars Juul, Deputy Chairman
LuxSpace Sàrl

Dr.-Ing. Arash Sadeghfam
Aachen University of Applied Sciences

Dr.-Ing. Stephan Holtrup
pinkRF

Abstract

This thesis presents the analysis of microwave plasma frequency-dependence based on the investigation of multi-physical parameters.
Fundamentals of a microwave plasma and high-frequency technology are explained. Frequency-dependent effects on the base point impedance are presented in combination with the description of the used measuring hardware.
Development of a bi-static network for the main plasma states (ignition and operation) is presented on the example of two high-pressure lamps at 2.45 GHz. Networks of both lamps are custom-built during the course of this thesis. An efficacy of 135 lm W^{-1} is achieved exceeding the efficacy of most LEDs.
Frequency-dependent electrical properties are analyzed by reflection measurements of three different prototypes (argon plasma jet, phosphor-coated lamp and hollow glass cylinder filled with xenon) for the first time. A novel and simple lumped element and 3D-model are developed for the fitting of the plasma. A series resonance circuit substitutes the frequency-dependency of the capacitive plasma. The models are extended for S_{21} measurements by a novel developed transmission prototype. A simple frequency-dependent capacitor lumped element model fits the transmission parameters of the plasma. The novel core/cone3D-model is capable of fitting the plasma in an FEM simulator by only using the conductivity.
A significant influence of the frequency on the spatial properties of all prototypes is measured for the first time by a simple CMOS camera and a custom image registration routine. The spatial extension is inversely proportional to the frequency. Optical measurements identify the participating ion species. Influence of the frequency on single spectral bands are presented in an in-depth analysis using optical emission spectroscopy. A proportionality of the frequency and the energy density in the microwave plasma is revealed. This is supported by the thermal measurements. The plasma jet rotational temperature is determined by the hydroxyl band at 310 nm and shows a maximum values of 1350 K at only 15 W.

Acknowledgements

This thesis is dedicated in memory to Hilke Rink and Prof. Michel Marso.

I would like to thank Prof. Holger Heuermann for his longtime support during all of my degree theses. He is a great source of information and sight. Thank you for being my guide from the basics of high-frequency technology, through my time at the FH Aachen to my doctoral thesis for more than ten years.

A special thanks goes to Prof. Rony Snyders and Prof. Hadji-Minaglou for filling the spot of Prof. Marso in the CET and for the possibility to cooperate with the University of Mons.

My gratitude goes out to the whole team of the Institute for Microwave and Plasma Technology at the University of Applied Sciences in Aachen, especially to Dr.-Ing. Stephan Holtrup, Dr.-Ing. Arash Sadeghfam and Thomas Harzheim for their continued support and help with the development. Thank you to Dr.-Ing. Nikolay Britun for a great co-operation at the University of Mons.

I would like to thank you to all my friends and my family, for accompanying me on the long way to this thesis. Among them are Dr.-Ing. Stephan Holtrup, Dr.-Ing. Ulrike Leyn, and Rosemarie Schopp. Thank you for your open ears, long discussions, new perspectives and proof-reading.

Contents

Abstract iii

Acknowledgements iv

Contents v

List of Figures x

List of Tables xvii

Abbreviations xviii

Physical Constants xx

Symbols xxi

1 Introduction 1
- 1.1 Thesis Overview 2
- 1.2 Special Requirements for the Development of Microwave Plasma Applications 4
- 1.3 General Overview of Research on Microwave Plasmas 5

2 Theory of Microwave Plasma Physics 8
- 2.1 Fundamentals of Plasma Physics 8
  - 2.1.1 Description of a Plasma 9
  - 2.1.2 Plasma Ignition and Townsend Process 9

2.1.3 Cross Section 11
2.1.4 Plasma Frequency 11
2.1.5 Mean Free Path and Electron Collision Frequency 12
2.1.6 Effective Conductivity 13
2.1.7 Effective Permittivity 14
2.1.8 Spectral Line Emissions of a Plasma 15
2.2 Fundamentals of Lighting Technology 20
2.2.1 Luminous Flux 20
2.2.2 Illuminance 21
2.2.3 Luminous Efficacy 21
2.3 Wave-Guide and Network Theory 23
2.3.1 Transmission Line Theory 23
2.3.2 Characteristic Impedance 23
2.3.3 Scattering Parameters 24
2.3.4 De-Embedding and Extraction of Plasma Base Point Impedance 25
2.3.5 Plasma Fitting using Lumped Elements and Lossy Dielectrics . 27
2.4 Theory for Different Frequencies 29
2.4.1 Frequency Effects on Electrons 29
2.4.2 Particle Interaction in a Plasma 30
2.4.3 Hot-S Measuring Environment 32
2.4.4 Analysis of System Error 34

3 Microwave Plasma Basics and Applications at 2.45 GHz 36
3.1 Bi-Static Network for Ignition and Operation of a Microwave Plasma 38
3.1.1 Introduction of the Main Plasma States 38
3.1.2 Amplitude Locked Loop as a Requirement for the Bi-Static Network 39
3.1.3 Meta-States in a Microwave Plasma 39
3.1.4 Generation of Free Charge Carrier to Ignite a Microwave Plasma 40
3.1.5 Operation of a Microwave Plasma by Electric Fields 43
3.1.6 Hardware Description of the Bi-Static Network for Ignition and Operation 45
3.2 Determination of the Base Point Impedance by Plasma Fitting 47
3.2.1 Lumped Element Model for Microwave Plasma Fitting in a Circuit Simulation 48

3.3 Bi-Static Network Development of RF-Driven High-Pressure Plasma Lamps . . . 53
3.3.1 Bi-Static Network Development of a High-Pressure UV-Lamp 53
3.3.2 Bi-Static Network Development for the Domestic High-Pressure Lamp (DHPL) . . . 59
3.3.3 Hardware Description of the DHPL Bi-Static Network . . . 61
3.4 Optical and Thermal Measurement Results of the UV-Lamp and DHPL 65
3.4.1 Efficacy Optimization of the Microwave Plasma by Signal Modulation of the Electric Field . . . 65
3.4.2 Measurement Results of the High-Pressure UV-Lamp . . . 69
3.4.3 Measurement Results Presentation for the High-Pressured DHPL . . . 73
3.5 Discussion of the Results . . . 75

4 Frequency Dependence of Microwave Plasma Electrical Properties 77
4.1 Lumped Element and 3D-Model for the Fitting of Reflection and Transmission Properties of a Microwave Plasma . . . 78
4.2 Extension of the Large Signal S-Parameter Measuring Environment . 80
4.2.1 Common Hardware Components and Measuring Equipment of the Extension . . . 80
4.2.2 Balanced Amplifier Stages of the Large Signal Measuring Test-Set-Up . . . 82
4.2.3 Summary of Extensions of the Large Signal Measuring Environment . . . 84
4.2.4 Large Signal S-Parameter Measuring Environment Extension for Plasma Transmission Properties . . . 85
4.2.5 Frequency Dependency Measuring Error . . . 85
4.3 Frequency Dependence of an Atmospheric Pressure Microwave Plasma Argon Jet . . . 88
4.3.1 Plasma Modeling for the Jet using Lumped Elements and Lossy Dielectrics . . . 88
4.4 Frequency Dependence of Low-Pressure Microwave Plasma Sources 97
4.4.1 Shared Network in Circuit and FEM Simulation for DUTs . . . 97
4.4.2 PC-Lamp Plasma Representation . . . 99
4.4.3 Measurement and Simulation Results of the PC-Lamp Base Point Impedance . . . 101

4.5 Frequency-Dependent Electrical Properties of the Low-Pressured Xenon Hollow Cylinder (XHC) . . . 108
4.5.1 Measurement and Simulation Results of the XHC-device . . . 109
4.6 Modeling of Argon Microwave Plasma By Electrical Transmission Properties . . . 117
4.6.1 Description of the Transmission Measurement Adapter Prototypes . . . 117
4.6.2 Fitting of Microwave Plasma Transmission Parameters using Lumped Element- and 3D-Modeling . . . 123
4.7 Discussion of the Results . . . 134

5 Multi-Physical Analysis of the Microwave Plasma's Frequency Dependence 136
5.1 Numeric Method for the Plasma Size Determination . . . 137
5.1.1 Image Registration Routine . . . 137
5.1.2 Ion Species Analysis Recognition . . . 139
5.2 Frequency Dependence of the Geometrical Expansions . . . 141
5.2.1 Frequency Dependence of the Plasma Jet's Geometric Expansion 141
5.2.2 Frequency Dependence of the PC-Lamp Plasma . . . 145
5.2.3 Geometrical Expansion of the Xenon Hollow Cylinder Plasma 148
5.2.4 Summary of the Geometrical Expansion Measurements . . . 150
5.3 Microwave Plasma Frequency Dependence Analysis by Optical Emission Spectroscopy . . . 151
5.3.1 Optical Properties and Optical Emission Spectroscopy of the Plasma Jet . . . 151
5.3.2 Frequency Dependency of the PC-Lamp's Optical Properties . 157
5.3.3 Frequency Dependency of the Xenon Hollow Cylinder's Optical Properties . . . 160
5.3.4 Summary of the Optical Properties Measurements . . . 163
5.4 Frequency Dependence of Microwave Plasma Thermal Properties . . 164
5.4.1 Frequency-Dependent Thermal Properties of the Plasma Jet . 166
5.4.2 Frequency Dependency of the PC-Lamp's Thermal Properties 169
5.4.3 Frequency-Dependent Thermal Properties of the XHC . . . 171
5.4.4 Summary of the Frequency-Dependent Thermal Measurement Results . . . 172
5.5 Discussion of the Measurement Results . . . 173

6 Conclusion **175**

Bibliography **177**

List of Figures

2.1 Paschen curve for atmospheric air, 1 bar = 750 Torr. Below the minimum, the decreased particle density requires a higher voltage. 10
2.2 Different spectra visualizing the different physical effects on a plasma spectrum. All spectra are set relative to the spectra at 43 W. 16
2.3 Graphical representation of the de-embedding process using the example of a plasma jet during operation. Different reference planes A and B are indicated as well as the different forward and reflected waves (a, b). 26
2.4 Electric field strength of an electron in a one-dimensional electric field excited to a field strength of $1 \times 10^{6}\,\mathrm{V\,m^{-1}}$ at the respective frequency. 30
2.5 Resulting RF conductivity over the frequency for different temperatures. 31
2.6 Block diagram of the large signal S-parameter measuring environment for the determination of microwave plasma properties. 32
2.7 Large S-parameter measuring environment. 34

3.1 Schematic view of a circuit simulation for the ignition state. 40
3.2 Simulated ignition field strength for the unbalanced electrode configuration using a non-fused and a fused set-up at 2.45 GHz and 15 W. Local electric field of the fused electrode is higher in the burner. The outlines are highlighted in black. 41
3.3 Balanced topology to simulate the ignition field strength at 2.45 GHz and 15 W. Fusing the electrode into the glass increases the maximum field strength by a factor of 1.5. Outlines are highlighted in black, . . 41
3.4 Simulated electric field strength inside the burner and glass body for the high-pressure lamp with a pressure of 20 mbar using argon. . . . 42

3.5 Schematic view of the operation network for probing the plasma. . . 43
3.6 Unbalanced and balanced probe approaches to transfer power from the amplifier to the plasma. 43
3.7 Schematic view of the Marchand balun and parallel transmission line. It has a length of $\lambda/4$ to enable variable wave impedance on the indicated X-axis. Sheath waves are suppressed by the extra outer conductor, which also converts the common to the differential mode. . . 44
3.8 Different construction forms for the bi-static network. 46
3.9 Schematic of the de-embedding process inside the circuit simulator to retrieve the base point impedance of the plasma. Reference planes A and B are indicated 48
3.10 Lumped element simulation of the UV-Lamp's base point impedance including a capacitor for the quartz-glass representation. 49
3.11 Comparison of the de-embedded magnitude and phase of the measurement (dashed line) and the circuit simulation (solid line) made in ADS. 49
3.12 FEM simulation of the UV-Lamp's de-embedding process. 51
3.13 Comparison of the de-embedded magnitude and phase of the 3D FEM simulation (dashed line) and the measurement (solid line). 52
3.14 First generation UV-Lamp and annotated schematic. 53
3.15 Cross-section and prototype of the second generation UV-Lamp. . . 54
3.16 Bi-Static network prototype of the first generation UV-Lamp. Metallic knitted fabric provides shielding and prevents radiation. 55
3.17 Cross-cut through the 3D-model of the bi-static network prototype of the first generation UV-Lamp. 55
3.18 Fitting (solid line) and measured (dashed line) S-parameters for the UV-Lamp. 56
3.19 Simulated electric field distribution of the UV-Lamp's ignition state. A maximum amplitude of $3.2 \times 10^5\,\mathrm{V\,m^{-1}}$ at 40 W is calculated. . . . 56
3.20 First generation UV-Lamp plasma with a low pressure at 200 W and 2.39 GHz. The electrode is located on the left side. 57
3.21 S_{11}-parameter fitting (solid line) and measurement (dashed line) of the UV-Lamp for an input power of 200 W. 57
3.22 Different geometries of the high-pressure lamp. 59
3.23 Bi-Static network prototype of the DHPL without radiation shielding. 61
3.24 Measurement (dashed line) and the simulation (solid line) of the DHPL lamp ignition. 62

3.25 Electric field distribution of the DHPL at 20 W and 2.43 GHz. Maximum field strength of $1.5 \times 10^6\,\mathrm{V\,m^{-1}}$ is achieved, allowing re-ignition for a measured surface temperature of 750 K. 62
3.26 DHPL during operation at 40 W and 2.43 GHz. High-pressure is achieved. The greenish look of lamp indicates that not all of the salts have entered the gas stage. Based on HFSS, about 35 W are coupled into the plasma. 63
3.27 S_{11} magnitude and phase comparison of simulation (solid line) and measurement (dashed line) for operation. 64
3.28 Low loss wave-guide tuning set-up containing shorting plunger, mounted shielded D8S lamp in fitting, 3-stub tuner and coax-wave-guide transition (left to right) 65
3.29 Output response of the photo diode for different duty cycles. 66
3.30 Efficacy changes of the wave-guide and the coaxial line set-up. . . . 67
3.31 Temperature of the UV-Lamp for an input power of 200 at 2.45 GHz. A maximum temperature of 740 K is reached on the glass surface. . . 69
3.32 First generation UV-Lamp Spectrum at 200 W and 350 W. Single spectral lines only differ in their intensity. Line broadening at 250 nm is visible and is more pronounced at 350 W. Spectrum indicates not high-pressure. 70
3.33 Spectrum of coaxial prototype using 350 W input power at 2.43 GHz. 71
3.34 Measured thermal distribution of the DHPL at input powers from 25 to 40 W. Maximum glass surface temperature is 995 K. Wires of the metallic knitted fabric are visible by the drops in temperature. 73
3.35 DHP lamp spectra at input power levels from 25 to 43 W. High pressure operation of the lamp at higher power levels is visible through an increased value and line broadening. 73

4.1 Transmission line set-up with plasma impedance representation for the reflection and transmission value. 79
4.2 Block diagram of the large signal S-parameter environment extension for the additional bands. 80
4.3 Input power vs output power of the amplifier stages for the extension of the large signal measuring environment at the indicated frequencies. 82
4.4 Graphical overview of the maximum linear output power available from 1.3 GHz to 3.5 GHz. 84
4.5 Block-diagram for the transmission measurement test-set based on the large signal S-parameter environment at different frequencies. . 85

4.6 Large signal S_{11} measurement and simulation comparison for the PC-lamp (2.5 GHz and 5 W with a resulting relative error of 3.7%). 86
4.7 Plasma jet with an argon plasma driven with 20 W at 2.43 GHz and a matching of −5 dB 88
4.8 Circuit simulation model of the jet represented by coaxial lines. Corresponding positions in the FEM simulation model are annotated. . . 89
4.9 Annotated FEM simulation model of the jet. The indicated positions are for visualization purposes of the circuit simulation model. 89
4.10 Comparison of the S_{11}-parameter of the measurement, circuit simulation and FEM simulation model. 90
4.11 Comparison of the plasma and its representation in an FEM simulator 91
4.12 Different models of the jet for the simulation of the plasma at 1.3 GHz and 5 W input power as an example for the FEM simulation. 91
4.13 Magnitude and phase of the measurement with additional data. . . . 92
4.14 Complex reflection values of a de-embedded jet for different frequency ranges. 94
4.15 FEM simulation of the electric field distribution of the plasma jet using a single plasma body and the conductivities presented in Tab. 4.1. 95
4.16 Representation of the measuring adapter inside the circuit simulator consisting of five different coaxial lines. At the end, an inductor and capacitor to ground are located which substitute the plasma of the PC-lamp and the XHC. 97
4.17 FEM simulation model of the shared network for the PC-Lamp and the XHC. Areas are indicated to identify the corresponding areas in the circuit simulation model. 97
4.18 S_{11} values of the fitting of the measuring network used for the PC-lamp and the XHC. 98
4.19 Prototype of the PC-lamp including the measuring network, metallic knitted fabric for shielding and a polyoxymethylene (POM) frame for fixation. 99
4.20 Cross-section of the FEM simulation model of the PC-lamp, including the N-plug and the measuring network. 99
4.21 S_{11} results of the plasma simulation for the PC-lamp using a single conductivity body inside the burner for a frequency of 1.3 GHz and an input power of 5 W. 100
4.22 De-embedded measured complex reflection values of the PC-lamp at 2 W, 5 W and 10 W. 101

4.23 PC-Lamp plasma model for the representation in the circuit simulator. It consists of a series resonance circuit. 103
4.24 Fitted values of the PC-Lamp plasma representation network in the circuit simulator. The network consists of a series resonance circuit of a capacitor and an inductor with a tunable Q-value. 104
4.25 Electric field distribution of the shielded PC-lamp at different frequencies and power levels. 105
4.26 Photograph of the set-up XHC including the probe network and metallic knitted fabric. 108
4.27 FEM model of the XHC to simulate the conductivity of the plasma. . . 108
4.28 Frequency-dependent S_{11} reflection values of the XHC at different power levels from 2 W to 5 W and frequencies from 1.3 GHz to 3.5 GHz.109
4.29 Series resonance circuit schematic for the plasma representation of the XHC in the circuit simulator. The resistor substitutes the losses of the circuit. 111
4.30 Values of the XHC plasma representation by lumped elements in the circuit simulator at power levels from 2 W to 5 W from 1.3 GHz to 3.5 GHz. 112
4.31 Electric field distribution of the shielded XHC at frequencies of 1.3 GHz, 2.4 GHz and 3.5 GHz and power levels from 5 W to 10 W. . . . 114
4.32 First prototype for the transmission measurements to explore and prepare the boundary conditions for the operation of a microwave plasma. 117
4.33 Second plasma transmission prototype using a coaxial topology to imprint a fixed and known wave impedance for the whole test fixture. 118
4.34 Overview of the impact of power and gas flow changes on the magnitude and phase of S_{21}. Measurements are made using the second transmission prototype for visualization purposes and verify the influence of the investigated parameters. 119
4.35 Built-Up prototype for the final transmission measurements. It consists of the plasma jet and a network for the HFD-lamp, which are connected by a custom-built screwable interconnection. 121
4.36 3D-model of the final transmission prototype with annotated areas. . 121
4.37 Argon plasma at different gaps. Input power of 10 W is constant at an excitation frequency of 3.4 GHz and a gas flow of 0.8 L min^{-1}. 122
4.38 Overview of the S_{21} transmission values for the FTNP with a closed gap. Both measurements and model in the circuit simulator are shown.123

4.39 De-embedded transmission plasma base point impedance of the FTNP for 10 and 15 W input power at different distances of the electrodes. 124
4.40 Lumped element model for the fitting fitting of the FTNP plasma. A series conductor with a tunable q-factor is utilized. The q-factor is represented by the series resistance. 125
4.41 Overview of the broadband S_{21} transmission values of the magnitude and phase for the FTNP from 1 GHz to 4 GHz. Measurement (dashed line) and fitting (solid line) are presented. 128
4.42 Overview of the measurement and the different plasma fitting models. The single cylinder model is simulated with a diameter of 1 mm. . . 129
4.43 HFSS plasma models for the different gaps between the electrodes from 1 mm to 3 mm. The power is coupled in from the left side. 129
4.44 Relative errors for the different power levels of the transmission fitting in the FEM simulator. Fitting is made for a gap of 1 mm at 2.4 GHz. 130
4.45 Fitted S_{21} transmission values for the FTNP conductivity of the plasma body at power levels from 5 W to 15 W and electrode distance from 1 mm to 3 mm. 132

5.1 Different stages of the Matlab image registration routine. 137
5.2 Plasma size at different frequencies and input power levels for the plasma jet and the PC-lamp. 138
5.3 Gray scale images of different microwave plasmas generated by the jet at 1.3, 2.4 and 3.5 GHz at power levels from 2 W to 10 W. 141
5.4 Comparison of the jet's plasma size at different frequencies and input power levels. 142
5.5 Size of the jet plasma at all measured frequencies, power levels along with numerical values of the relative size changes compared to the results of the 1.3 GHz band. 143
5.6 Inverted gray image comparison of the measured frequencies and power levels for the PC-Lamp plasma. Black represents the areas of highest brightness. 145
5.7 Overview at different frequencies and input power levels for the PC-Lamp plasma. 146
5.8 Size of all measured frequencies, power levels, and relative size changes compared to the results of the 1.3 GHz band. 147
5.9 Inverted gray image comparison of the XHC plasma size at different frequencies and power levels. 148

5.10 Absolute size of the plasma inside the XHC. 149
5.11 Spectrum and zoomed spectrum of the plasma jet at different frequencies for a constant input power of 10 W. 152
5.12 Measured irradiance and resulting ratio of the irradiance to the surface of the jet plasma. 153
5.13 Plasma at different frequencies and input powers from 1.3 GHz to 3.5 GHz and 2 W to 10 W input power using pure argon as process gas. 155
5.14 Different spectral components of a pure argon plasma at 310, 370, 696 and 777 nm using a constant input power of 10 W. Photographs are taken with a band-pass dichroic filter at each wavelength. 155
5.15 Frequency- and gas-flow-dependent behavior of a pure argon plasma from 1.3 GHz to 3.5 GHz and flows from 1 L min^{-1} to 4 L min^{-1} at the OH-band around 310 nm. 155
5.16 Dependency of the gas-mixture of argon and nitrogen at different frequencies and a constant gas-flow of 4 L min^{-1}. Percentage of nitrogen added to the plasma is indicated on the left side. 155
5.17 Spectrum and annotated spectrum at 10 W input power. 157
5.18 Comparison of optical measurement results for the PC-Lamp. 158
5.19 Spectra at different frequencies and spectrum with annotated ion species for the XHC. 160
5.20 Irradiance and irradiance per surface ratio. 161
5.21 Recorded temperature of the jet's inner brass conductor for all measured frequencies and power levels. 166
5.22 Measured and fitted OH-band around 310 nm to determine the rotational temperature T_{Rot}. Residuals display the difference between the measured and the fitted results. 167
5.23 Fitted temperature for frequencies from 1.3 GHz to 3.5 GHz and input powers from 5 W to 15 W for a constant pure argon gas flow. Upper plot shows the results for a gas flow of 2 L min^{-1}, the lower plot for 4 L min^{-1}. Measuring accuracy of the input power is within a 5% window. 168
5.24 Comparison of the PC-Lamp glass surface temperature from 1.3 GHz to 3.5 GHz at power levels from 2 W to 10 W. 169
5.25 Temperature of the XHC device for all frequencies and power levels ranging from 320 K to 390 K. 171

List of Tables

2.1 Plasma ions of three highest UV wavelength peaks within in the spectral area from 230 nm to 380 nm. 18
2.2 Light efficacy for several lighting sources. 20
2.3 Light efficacy for several lighting sources. 22
2.4 Overview of period times, wavelength and the relative changes of the wavelength to the 1.3 GHz band for the investigated bands around: 1.3, 2.45 and 3.5 GHz. All values are calculated for vacuum conditions. 29

3.1 Measured and calculated properties of the DHPL at 2.39 GHz 74

4.1 Fitted RF conductivities using the plasma body model at power levels from 5 W to 15 W and frequencies from 1.3 GHz to 3.5 GHz. 95
4.2 Fitted PC-Lamp Plasma RF conductivities obtained from the FEM simulator. 106
4.3 Overview of the fitted values for the extracted RF conductivities at different power levels and frequencies for the XHC-device. 115
4.4 Circuit simulation results for the transmission network using a single capacitor and a tunable frequency-dependent q-factor. 126

5.1 Summary of the settings of the CMOS camera and the resulting calculated variances of the plasma jet size analysis measurements. . . . 142
5.2 Overview of the photograph properties and resulting systematic relative error for the PC-Lamp spatial results. 145
5.3 Comparison of the photograph properties and resulting systematic relative error for the XHC plasma size measurements. 148

Abbreviations

ASCII **A**merican **S**tandard **C**ode for **I**nformation **I**nterchange

AC **A**lternating **C**urrent

ADS **A**dvanced **D**esign **S**ystem

ALL **A**mplitude **L**ocked **L**oop

AM **A**mplitude **M**odulation

CMOS **C**omplementary **M**etal-**O**xide-**S**emiconductor

CW **C**ontinuous **W**ave

DC **D**irect **C**urrent

DHPL **D**omestic **H**igh **P**ressure **L**amp

DUT **D**evice **U**nder **T**est

EM **E**lectro-**M**agnetic

FEM **F**inite **E**lement **M**ethode

FTNP **F**inal **T**ransmission **N**etwork **P**rototype

GaN **G**allium **N**itrite

HFSS **H**igh **F**requency Electromagnetic Field **S**imulation **S**ystem

KIT **K**arlsruhe **I**nstitute of **T**echnology

LTI **L**icht**t**echnisches **I**nstitut

MHCD	**M**icro **H**ollow**C**ylinder**D**ischarge
IR	**I**nfra**r**ed
ISM	**I**ndustrial **S**cientific **M**ilitary
LDMOS	**L**atteraly **D**iffused **M**etal **O**xide **S**emiconductor
LED	**L**ight **E**mitting **D**iode
NIST	**N**ational **I**nstitute of **S**tandards and **T**echnology
NOx	**N**itrogen-**O**xyde
OES	**O**ptical **E**mission **S**pectroscopy
OSM	**O**pen **S**hort **M**atched
PC-Lamp	**P**hosphor **C**oated Lamp
PCB	**P**oly**c**hlorierte **B**iphenyle
PWM	**P**ulse **W**idth **M**odulation
RF	**R**adio **F**requency
SMA	**S**ub**M**iniature Type **A**
UV	**U**ltra-**V**iolet
XHC	**X**enon **H**ollow **C**ylinder

Physical Constants

Boltzmann constant	k	=	$1.3806 \times 10^{-23}\,\mathrm{J\,K^{-1}}$
Electron Charge	e	=	$1.602\,176 \times 10^{-19}\,\mathrm{C}$
Electron Mass	m_{e}	=	$9.109 \times 10^{-34}\,\mathrm{g}$
Loschmidtsch's Number	N_{L}	=	$2.686\,777\,4 \times 10^{19}\,\mathrm{cm^{-3}}$
Magnetic Permeability	μ_{r}	$=$	$4\pi \times 10^{-7}$ H/m (exact)
Speed of Light	c	$=$	$2.997\,924\,58 \times 10^{8}$ ms^{-2} (exact)
Planck's constant	h	$=$	$4.13556\pi \times 10^{-15}$ eV/s
Vacuum permittivity	ε_0	=	$8.854 \times 10^{-12}\,\mathrm{F\,m^{-1}}$

Symbols

α	attenuation factor	Ω
β	angle measure	Ω
C	capacity	F
d	distance	m
E_{V}	illuminance	lx
σ_{C}	cross-section	m^2
σ_p	current density	$\mathrm{A\,m}^{-3}$
γ	propagation	Ω
G	conductance	S
I	current	A
L	inductivity	H
λ_{MFP}	mean free path	m
ν_{e}	electron oscillation frequency	Hz
n	particle density	m^{-3}
P	power	W (Js^{-1})
p	pressure	bar
Φ_{Light}	luminous flux	lm

r	radius	m
R	resistance	Ω
t	time	s
T	temperature	K
V	voltage	V
v_e	drift velocity	$\mathrm{m\,s^{-1}}$
ω	angular frequency	$\mathrm{rads^{-1}}$
Z_0	characteristic impedance	Ω

Chapter 1

Introduction

A plasma describes a gas, which is partly ionized and therefore consists of free electrons, ions, and neutral particles. Technologies based on a plasma date were first invented more than 200 years ago.
An arc based carbon lamp was invented around 1805, as the first practical light. The predecessor of the gas discharge lamp was created in form of the Geissler tube in 1857 ([1]). Neon tube lighting was developed based on observations of the Geissler tube ([2]). The mercury-vapor lamp was invented in 1892 and commercialized in the early 1900s ([3]). High-pressure xenon lamp was created in 1951 ([4]) with a high light efficiency.
First microwave plasma applications have been developed since the 1950s ([5]) and were used as surface wave plasma source from 1 MHz to 10 GHz ([6]).
Radio frequency glow discharges have been in use for material manipulation at 13.56 MHz ([7]).
The microwave frequencies range from 1 GHz to 100 GHz with most applications located up to 40 GHz. Inside the industrial, scientific and military (ISM) band around 2.45 GHz [1] applications do not require any permission to be operated. Therefore up-coming microwave sources are located primarily in the ISM frequency bands. Hence all generated microwave plasma applications regardless of their size are restricted to the invariable wavelengths of these ISM bands. For existing applications,

[1]Worldwide usable ISM bands in the radio frequency area are located at 433 MHz and 5.65 GHz

the behavior of the microwave plasma at their nominal input power has not been investigated yet at frequencies in between the ISM bands. Therefore the frequency-dependent effects on the properties of a microwave plasma are investigated and analyzed in this thesis.
The electro-magnetic field behavior at microwave frequencies offers several advantages, such as contact-less energy transfer and compact design due to the small wavelength. These advantages can be used in plasma jets for physical manipulation such as cutting, welding or cleaning material from unwanted residues. Surface activation is another application area, where the plasma can improve the adhesiveness. In the medical sector, microwave jets are employed for the disinfection of human tissue ([8]). Apart from the jet, microwave plasma applications range from lighting purposes to spark plugs for the ignition of lean mixture engines ([9]).
Analyses on the frequency-dependence of the multi-physical parameters are performed in this thesis. This is done to determine the influence on the applications and identify possible advantages by adapting the frequency to the application.
The challenge for these purposes is to design specific networks for ignition and operation of the plasma by reducing the required power due to the cost of the amplifier. Low priced hardware to generate radio-frequency (RF) signals at higher power levels has improved the market position of microwave plasmas. Many cheaper amplifier generations like LDMOS-transistors ([10]) are surpassed by the newer generation GaN transistors ([11]). These new amplifiers perform with a higher efficiency at higher frequencies.

1.1 Thesis Overview

In this thesis, the scientific frequency-dependent investigation and analysis of microwave plasmas from 1.3 GHz to 3.5 GHz is presented. These frequency-dependency analyses are made for the first time.
Chapter 2 explains basics of plasmas, optical emission spectroscopy, lighting technology, and high-frequency technology for the characterization of the microwave plasmas. A simple mathematical model illustrates the frequency-dependent effects on an electron. The large signal scattering parameter measuring environment for the determination of the plasma base point impedance is presented.

In Chapter 3 the development of a bi-static network for the two main states of a microwave plasma is explained[1]. After probing the plasma, the base point impedance is extracted by de-embedding the fitting of the plasma using a lumped element model in a circuit simulator and a 3D-model in an FEM simulator. On the example of two novel high-pressure lamps at 50 W and 400 W, the development workflow for a bi-static is explained and analyzed in detail. For the first time, a high-pressure in a hollow-cylinder electrode-less UV-Lamp and an efficacy of more than $135\,\mathrm{lm\,W^{-1}}$ for a coaxially driven electrode-less lamp is achieved.
Chapter 4 introduces the necessary extensions of the measuring hardware to analyze the frequency-dependence of microwave plasma electrical properties. Three different plasma applications[2] at different pressures are investigated and it is shown that the development workflow for a bi-static network can be applied to other frequencies. Analyses of the frequency-dependency reveal that most investigated microwave plasmas exhibit a capacitive dominated base point impedance. A new lumped element model is introduced based on a series resonance circuit. This model is capable of fitting two different plasma gases: argon and xenon. A new 3D-model for the fitting of the plasma conductivity in the FEM simulator is introduced. It is shown, that this model fits the plasma only by varying the conductivity. This model is based on the analysis of the microwave plasma transmission electrical properties. The transmission analysis is made for the first time during the course of this thesis.
In Chapter 5 the analysis of the frequency-dependence of spatial, optical and thermal plasma properties is presented for the prototypes from Chapter 4 for the first time. Spatial properties are investigated using a simple CMOS camera in combination with a custom-written image registration routine. The frequency has a significant influence on the size of the microwave plasma and it is shown that energy density is proportional to the frequency. Optical properties are analyzed with a spectroscope. The optical results underline the observation, that the proportionality of the energy density to the frequency. Optical emission spectroscopy determines the frequency-dependent changes on single spectra lines of the plasma jet. It is shown, that the frequency affects all spectral wavelengths. The dependence of the gas flow, gas mixture, and power on the spectral properties is presented too. Thermal properties of all prototypes are investigated using an IR-camera. For

[1] ignition and operation
[2] plasma jet, phosphor-coated lamp and a hollow cylinder glass filled with low-pressured xenon

the jet, the rotational temperature is determined based on the OH line at 310 nm. Temperatures of up to 1350 K are measured at only 15 W of input power.
The thesis is concluded in Chapter 6 by a summary of the analyses.

1.2 Special Requirements for the Development of Microwave Plasma Applications

Plasma properties are influenced by many external factors like power, kind of coupling, frequency, pressure, temperature, and material. Therefore the values of some parameters, the design of the network and dimensioning of the amplifier have to be chosen appropriately and are based on the application. For example, the structural form, starting and operating pressure, temperature and luminous output during operation are parameters for the design of a lamp. Custom microwave lamps like the mercury-free energy saving lamp ([12]) are reliant on a specific cold-spot temperature for the specified efficacy. In this case, the input power has to be optimized for a specific temperature range. Due to different lamp topologies, each plasma has to be characterized and measured. Several physical properties of the used process gas, filling pressure and topology specify the operation window.
Since a plasma at microwave frequencies does not require the contact of an electrode to transfer the power into the plasma, a different gas mixture for lamps is possible. In former lamp generations, gases were not appropriate for the test because they would interact with the metal of the electrode leading to degradation and finally to the destruction of the lamp. A circular glass body is hollowed and filled with the desired gas mixture to create the first lamp prototype. Mercury is used for the first experiments since it offers the highest gas pressure at the lowest temperatures. In later prototypes, metal halogenides are added to fill gaps in the optical spectrum.
The microwave plasma jet requires a matching of the RF-network to the impedance of each process gas. Based on the ionization energy of the gas, the geometry of the inner conductor has to be adjusted. Different process gases exhibit different temperatures, to which the material has to be chosen accordingly.

1.3 General Overview of Research on Microwave Plasmas

First experiments on the electrical breakdown of gases using frequencies from 1 GHz up to 9 GHz were carried out in [13]. The influences of the pulse width and pressure are presented. The connection of a microplasma[3] and a microwave plasma source is explained in [14] including a summarized history of microplasma applications. First applications of a microplasma are described in [15] presenting an atmospheric pressure operation of a micro discharge in a cylindrical hollow cathode geometry (MHCD). Further applications were located in the area of chemical analysis such as plasma atomic spectrometry and chromatography. Other applications can be found in [16] such as remediation of NOx from car exhaust gases.
An argon plasma jet is used to determine the frequency-dependent effects at atmospheric pressure. These jets can be found in different areas such as surface manipulation or devitrification of water.
A general overview of a microwave plasma jet and a comparison to other plasma sources is given in [8]. [17] covers the benefits of plasma jets for medical therapy and provides a risk estimation. An analysis of possible security standards is given. The medical usage of a plasma jet and the characterization of an argon/air mixture to treat wounds are shown in [18]. In [19] a microwave line plasma using a loop-structured wave-guide is described and analyzed using a high-speed camera. A 60 cm plasma is achieved using 1 kW input power. The optical spectrum properties of an argon plasma jet at 2.45 GHz using different input gas pressures is explained in [20].
Several characteristics of a plasma at 2.45 GHz are shown in [21]. Spectral properties of different process gases ionized with a microwave source at 2.45 GHz and 5.5 kW are presented in [22]. In [23] an investigation of a microplasma up to the THz region is presented. [24] describes the effects of the gas flow on several plasma properties at 2.45 GHz. For an automotive plasma ignition system, a real-time impedance measurement is shown in [25]. The frequency dependence on microwave plasma has also been described in [26]. An analytical approach to calculate the plasma properties and the frequency influence is presented in [27]. Another approach to determine the electron kinetics of microwave plasma is shown in [28]. A general overview of the optical spectroscopy is given in [29]. A method to

[3] Plasma of small dimensions close to the Debye-length

drive a plasma jet more efficiently using a hairpin copper wire is described in [30]. Interaction of the microwave radiation and the plasma showing characteristic interference patterns are explained in [31]. An enhanced efficiency of the plasma jet using power modulations and gas mixing is presented in [32].
Microwave plasma sources provide new approaches for lighting purposes. A history of these microwave-driven lamps can be found in [33]. [12] shows an electrode-less energy-saving lamp with an input power of 10 W. Electrode-less UV-lamps driven with an input power of 200 W has been developed in [34]. Influence of RF-excitation on automotive D8S headlights (80 $\mathrm{lm\,W^{-1}}$) has been investigated in [35] and an efficacy increase of up to 95 $\mathrm{lm\,W^{-1}}$ by a superimposed AM signal is reported in [36]. Existing lighting products for floodlight or industrial hall applications are powered by a resonant cavity. At the cavity's resonant frequency, power is coupled to the lamp by a waveguide mode. The ellipsoid lamp exhibits a typical length of 20 mm and a maximum diameter of 10 mm. Due to the power level of 50 W and more, the heat sink is big and shades the upper half space of the lamp. More details on the resonator lamp can be found in [37].
In [38] the investigation of the differences between switched-DC[4] and RF-operation of an automotive D-lamps is presented. It is shown that the luminous efficacy of the RF operation almost equals the switched-DC operation. A new operation mode for a high-pressure lamp[5] is explored where the contact of the plasma arc and the electrode is merely capacitively, and the temperature of this mode is lower than in switched-DC. In addition, the RF power can be reduced to 10 W, when an amplitude modulated signal is superimposed. There is a different problem taken into consideration: For Switched-DC modes, the required current is very high thus the amplifiers have to be designed accordingly. This issue does not occur for the RF-operation since only the power is necessary for the generation of the plasma.
Fundamentals of plasma materials and discharges are also taken from [39]. In [40] the electrical properties of an argon microwave plasma in a circular resonator structure are presented. Frequencies at 0.9 GHz and 1.8 GHz and an input power of 1 W have been characterized. Electron density increases with the frequency of

[4] Direct current pulsed at about 500 Hz
[5] The plasma arc is coupled capacitively without contact to the electrodes

the investigated plasma, whose size is close to the Debye length. In [41] the conductivity of a plasma in a circular ring resonator structure has been shown for frequencies from 350 MHz up to 8 GHz. [42] describes the generation of a plasma by a dielectric resonator an array up to 1.1 GHz. The excitation frequency effects from 0.01 GHz to 2.45 GHz at a simulated power per unit area of 2.5 $\mathrm{W\,cm^{-2}}$ on plasma properties for a plasma in a 0.5 mm gap has been shown in [43]. A non-monotonic connection between the frequency and electron density is indicated along with a relationship between the mean plasma density and impedance. Further details on plasma properties at 900 MHz and 1.8 GHz can be found in [44], where an argon microplasma is analyzed using a split-ring resonator structure and a laser diode. A study on the breakdown of gases at 800 MHz and 900 MHz in two resonators has been shown in [45].

Chapter 2

Theory of Microwave Plasma Physics

In this chapter, the fundamentals of plasma physics and high-frequency technology are presented along with the experimental set-up required for the characterization of a plasma during operation. The matching of the wave impedance to the plasma base point impedance[1] is of great interest for the simulation and development of a network for a plasma. Special techniques are used to represent the plasma inside a circuit and FEM simulator. A model to describe the influence of the frequency on the electron's energy in a fixed time frame is shown, since frequencies differ in their wavelength only. The large-signal S-parameter measuring environment is presented along with the extension to operate and characterize microwave plasma around 1.3 and 3.5 GHz in order to determine the base point impedance. A detailed description on the used hardware and the principle of the large signal S-parameter measuring environment is given.

2.1 Fundamentals of Plasma Physics

In this section, several principles are explained to understand the frequency-dependent effects on microwave plasma. The focus is on the description of

[1]Base point impedance describes the input impedance of the plasma and can be compared to the feed point impedance of an antenna.

the electric properties conductivity and permittivity. Plasma basics are taken from [46], [47] and [48]. More details on plasma basics and the interactions with high-frequency electric fields and the RF-conductivity can be found in [49],[38] and [50]. The ignition of a plasma using high-frequency electric fields is described in [13] and [51].

2.1.1 Description of a Plasma

In a plasma the ratio of positive to negative charge carriers is almost equal. This is called quasi-neutral. Physical properties of a plasma are determined by the complex interaction of its particles. The particle density n_p is dependent on the energy level within the plasma. In Eq. (2.1) the connection between the pressure p and the temperature T of the plasma is given.

$$p = n_{\mathrm{p}}\, k_B\, T \tag{2.1}$$

k_B is the Boltzmann constant.
A higher particle density leads to higher collision probability, which also influences the properties of the plasma. Section 2.1.3 will explain this in more detail.
Further calculations will make use of the electron density n_{e}, which is equal or almost equal to the ion density n_{i}. In a plasma, only a portion of particles is ionized and therefore $n_{\mathrm{e}} << n_{\mathrm{p}}$.
A plasma is not self-sustaining and requires a constant energy input. One way to sustain the desired energy level is coupling the power into the plasma via an external electro-magnetic field. This thesis will investigate and analyze the influence of the electro-magnetic field frequency in the range of frequencies around 1.3 GHz, 2.4 GHz and 3.5 GHz on the properties of the plasma.

2.1.2 Plasma Ignition and Townsend Process

The existence of free charge carriers is a foundation for a plasma. Breakdown of the gas causes the generation of charge carriers. These can be electrons or ionized particles of the gas. The breakdown voltage describes the minimum amount required for an electric insulator to become electrically conductive. In other words: when the energy level of electrons is above the ionization energy. Paschen's law can calculate the breakdown voltage $V_{\mathrm{Breakdown}}$. It is an empirically discovered equation

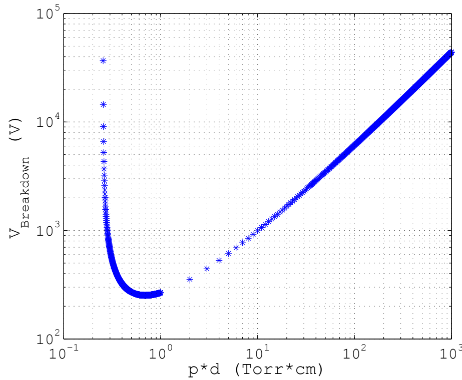

Figure 2.1: Paschen curve for atmospheric air, 1 bar = 750 Torr. Below the minimum, the decreased particle density requires a higher voltage.

describing the connection of the breakdown voltage, pressure p in a gap with a distance d.

$$V_{\text{Breakdown}} = \frac{a\,p\,d}{\ln(p\,d) + b} \tag{2.2}$$

Material constants a and b are dependent on the gas composition and are an interpolation for the Townsend coefficient.
It has been shown in [52] that Paschen's law can be applied to AC and even RF-sources, if they meet special conditions, such as a small gap width between the electrodes from 25 µm to 70 µm. For larger gap widths additional models are required, therefore Paschen's law can only estimate the breakdown voltage at radio frequencies.
In Fig. 2.1 the Paschen curve for air is plotted. There is a minimum for the breakdown voltage at a certain combination of pressure and distance, which is often called Paschen minimum. It is for example about 330 V for air. If the distance between the electrodes is increased, the voltage increases too. By decreasing the distance and pressure combination the voltage increases. Paschen's law describes the effect of impact ionization. The probability of impact ionization is lowered by a decrease of the particle amount. A reduction is caused by pressure or length reduction. Since the particle density of the investigated microwave plasmas is not determined, the following examples are based on an ideal gas at a pressure of

$p = 1\,\mathrm{bar}$. The particle density can be described by Loschmidtsch's Number $N_\mathrm{L} = 2.686\,777\,4 \times 10^{19}\,\mathrm{cm}^{-3}$.
The free charge carriers are accelerated by an external electric field. Upon colliding with another particle, a free charge carrier can generate more free charge carriers. Due to the law of conservation of energy, this can only occur, if the energy exceeds the work function of the other particle. This avalanche-like process is called the Townsend process. A higher overall energy level within the plasma leads to an increase in probability for the generation of free charge carriers.
More information on the ignition process can be found in [51], [53], [54], and [55]. Breakdown of gases and the development of an electron avalanche are described in more detail in [56], [57] and [58].

2.1.3 Cross Section

A plasma is sustained by the generation of new free charge carriers through particle collisions. To calculate the probability of a collision, the effective cross-section of the involved species is used. The effective cross-section σ_c is expressed by the radii r_1 and r_2 of the different species.

$$\sigma_\mathrm{c} = \pi \left(r_1^2 + r_2^2\right) \tag{2.3}$$

The involved species may be an electron, ionized atom core of one of the species, a neutral atom or a single proton or neutron. Based on the different size of the radii, an effective cross-section for each particle combination is calculated. Smaller particles have a lower cross-section and this leads to a smaller probability of a collision. An increase of the particle density also increases the collision probability.

2.1.4 Plasma Frequency

Electrons represent the most movable particles in a plasma and therefore take part in most collisions. They are the primary charge carriers of the plasma too. In Chapter 4 a specific capacity for microwave plasmas is introduced, which is mainly influenced by the frequency. If all electrons could travel freely through the plasma body, the resulting impedance would approach zero[2]. Each particle collision and thus the generation of new charge carriers increases the impedance of the plasma.

[2] Conductivity of the plasma would approach infinity.

After the generation of electrons, Coulomb's force tries to re-establish a neutral distribution of the charges. Caused by the inertia of the particle mass, the electrons oscillate around a neutral state, leading to an oscillation ω_p of the electron charge density n_e which is described by

$$\omega_\mathrm{p} = \sqrt{\frac{n_\mathrm{e}\, e^2}{\varepsilon_0\, m_\mathrm{e}}} \tag{2.4}$$

m_e is the electron mass. This oscillation is called the plasma frequency and is based on the assumption that ion mass is infinite. An electro-magnetic wave inserting the plasma interacts with the electrons and stimulates the plasma frequency. Therefore the plasma frequency along with the local electron density and energy of the electrons influence the impedance of the plasma directly.

2.1.5 Mean Free Path and Electron Collision Frequency

The mean free path λ_MFP describes the distance a free charge carrier is able to travel before statistically colliding with another particle. It is described by the cross section σ_c, and the overall particle density n_p in

$$\lambda_\mathrm{MFP} = \frac{1}{\sqrt{2}\, n_\mathrm{p}\, \sigma_\mathrm{c}}. \tag{2.5}$$

For an ideal gas at 1 bar the mean free path is calculated by

$$\lambda_\mathrm{MFP} = \frac{1}{\sqrt{2}\, p\, N_\mathrm{L}\, \sigma_\mathrm{c}}. \tag{2.6}$$

For all parting plasma species[3], different collision probabilities and frequencies exist.
Since the electrons are the agilest species within the plasma, the electron collision frequency is given by Eq. (2.9). This equation is just an approximation for a fixed probability.

[3] ions, neutral molecules and electrons

The mean free path can also be expressed by the Debye length: λ_{D}.

$$\lambda_{\mathrm{MFP}} = \frac{2\,\omega_{\mathrm{P}}\lambda_{\mathrm{D}}}{\nu_{\mathrm{e}}} \tag{2.7}$$

using

$$\lambda_{\mathrm{D}} = \sqrt{\frac{\varepsilon_0\,k_{\mathrm{B}}\,T}{n_{\mathrm{e}}\,e^2}}. \tag{2.8}$$

It is a characteristic quantity of the sphere of influence, in which the electric field of a local charge impacts other charge carriers. Combining the Debye length λ_{D} and the mean free path λ_{MFP} of a plasma, one is able to calculate the electron collision frequency ν_{e}, which depends on the temperature and electron density, by using

$$\nu_{\mathrm{e}} = \frac{2\,\omega_{\mathrm{P}}\,\lambda_{\mathrm{D}}}{\lambda_{\mathrm{MFP}}}. \tag{2.9}$$

Another expression of the mean free path uses the drift velocity $|\vec{v_{\mathrm{d}}}|$

$$\nu_e = \frac{|\vec{v_{\mathrm{d}}}|}{\lambda_{\mathrm{MFP}}} \tag{2.10}$$

2.1.6 Effective Conductivity

An objective of this thesis is the characterization of a microwave plasma by its electrical properties. It is necessary to take a closer look at the influence of the plasma on an electro-magnetic wave at the same time traveling through and exciting it. Doing so the effective conductivity and permittivity of a plasma can be concluded. To simplify the derivation a plane wave solution along with a steady-state plasma is assumed. More details can be found in [48].
If electrons in a steady-state are exposed to an electric field $\vec{E}$, the drift velocity $\vec{v}$ can be described as

$$\vec{v_{\mathrm{d}}} = -\frac{e\,\vec{E}}{m_{\mathrm{e}}\,\nu_{\mathrm{e}}} \tag{2.11}$$

using the electron collision frequency ν_{e} and the mass of the electrons m_{e}.
The current density $\vec{J}$ is defined as the amount of charge carriers n_{e} flowing through a defined surface per time. Using Eq. (2.11) the current density $\vec{J}$ can be

expressed by

$$\vec{J} = -n_\mathrm{e}\, e\, \vec{v} \tag{2.12}$$

and also by

$$\vec{J} = \frac{n\, e^2}{m_\mathrm{e}\, \nu_\mathrm{e}}\, \vec{E}. \tag{2.13}$$

The current density can also be expressed by the conductivity σ_p

$$\vec{J} = \sigma_\mathrm{p}\, \vec{E}. \tag{2.14}$$

A parameter comparison of Eq. (2.14) and Eq. (2.12) results in

$$\sigma_\mathrm{p} = \frac{n\, e^2}{m_e\, \nu_e}. \tag{2.15}$$

A one-dimensional electric field with an angular speed ω_RF of

$$\omega_\mathrm{RF} = 2\,\pi\, f_\mathrm{RF} \tag{2.16}$$

is expressed by

$$\vec{E}(\vec{z}, t) = \vec{A}\, e^{-j\,\omega_\mathrm{RF}\, t}. \tag{2.17}$$

The drift velocity $\vec{v}_\mathrm{d}$ of a plasma can be explained using

$$\vec{v}_\mathrm{d} = -\frac{e\,\vec{E}}{m_\mathrm{e}(\nu_\mathrm{e} - j\,\omega_\mathrm{RF})}. \tag{2.18}$$

Following the same principle as in Eq. (2.15), the RF conductivity σ_RF of a plasma can be expressed via

$$\sigma_\mathrm{RF} = \frac{n_\mathrm{e}\, e^2}{m_\mathrm{e}\,(\nu_\mathrm{e} - j\,\omega_\mathrm{RF})}. \tag{2.19}$$

2.1.7 Effective Permittivity

Based on the work of [48] the effective permittivity of a plasma for an electric field described in Eq. (2.17) can be derived using the plane wave solution. Therefore Maxwell's equation

$$\nabla \times \vec{H} = \vec{J} + \frac{\delta \vec{D}}{\delta t} \tag{2.20}$$

is used. Inserting Eq. (2.14) and

$$\vec{D} = \varepsilon_0 \, \vec{E} \tag{2.21}$$

into Eq. (2.20) leads to

$$\nabla \times \vec{H} = \sigma_{\mathrm{RF}} \, \vec{E} - j \, \omega_{\mathrm{RF}} \, \varepsilon_0 \, \vec{E} \tag{2.22}$$

and to

$$\nabla \times \vec{H} = -j \, \omega_{\mathrm{RF}} \, \varepsilon_0 \, (1 + j \frac{\sigma_{\mathrm{RF}}}{\omega_{\mathrm{RF}} \, \varepsilon_0}) \, \vec{E}. \tag{2.23}$$

The parameter comparison results in the following equation:

$$\varepsilon_{\mathrm{eff}} = 1 + j \frac{\sigma_{\mathrm{RF}}}{\omega_{\mathrm{RF}} \, \varepsilon_0}. \tag{2.24}$$

After inserting σ_{RF} the effective electric permittivity is calculated by

$$\varepsilon_{\mathrm{eff}} = 1 - \frac{n_{\mathrm{e}} \, e^2}{m_{\mathrm{e}} \, \varepsilon_0 \, \omega_{\mathrm{RF}}^2 (1 + j \frac{\nu_{\mathrm{e}}}{\omega_{\mathrm{RF}}})}. \tag{2.25}$$

2.1.8 Spectral Line Emissions of a Plasma

Most of the plasma properties are caused by the interaction of ionized particles. Upon these interactions, the energy level changes and electro-magnetic radiation is emitted from the ionized media. Based on the species of the plasma, characteristic spectral lines are pronounced. Plasma properties like species, ionization degree, pressure and particle density can be extracted from the spectral data. A measured spectrum is the superimposed result of different physical effects: peaks are caused by discrete spectral lines, while the continuum consists of recombination radiation and bremsstrahlung.

Optical emission spectroscopy, or OES[4], is based on the measurement of light generated as a result of spontaneous relaxation of excited species in the plasma. The phenomenon of stimulated emission can also be of use for diagnostic purposes. More information on plasma spectrometry can be found in [59].

In the following list the different effects are elucidated:

[4] also known as atomic emission spectroscopy-AES

Discrete Spectral Lines Energy is transferred between the particles during a collision leading to a shift in the energy level of each particle. If the energy level of an electron e surpasses the work function of the atom A, the electron is removed from the atom and can act as a free charge carrier. The energy of the second electron is reduced by the power level of the newly generated one. This process can be expressed by

$$A + e^- \rightleftarrows A^+ + e^- + e^-. \tag{2.26}$$

Transfer of an electron's energy is possible by the spontaneous emission, which describes the quantum mechanical transition from a higher energy state h to a lower while emitting a photon with a light frequency ν_l.

$$A^{hl5} \rightleftarrows A^{l6} + h\,\nu_l \tag{2.27}$$

h is Planck's constant. The emitted wavelength λ of the photon is extracted using the speed of light c_0

$$\lambda_l = \frac{c_0}{\nu_l}. \tag{2.28}$$

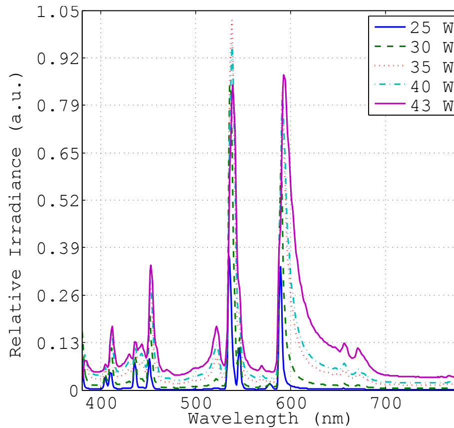

Figure 2.2: Different spectra visualizing the different physical effects on a plasma spectrum. All spectra are set relative to the spectra at 43 W.

[5] Atom with energy level hl
[6] Atom with energy level l

In Fig. 2.2 single spectral lines are visible at different wavelengths. In Chapter 5 the emission lines employ the ionization degree of an argon and xenon plasma.

Bremsstrahlung Interaction of particles inside a plasma is not limited to collisions. Due to the charge of the different particles, the impulse is continuously changing. Any impulse change causes radiation of energy. It is called bremsstrahlung. The amount of radiated energy is proportional to the modification of impulse and thus to change of kinetic energy.
In Fig. 2.2 the continuum is pronounced between the spectral lines. An increase in the input power leads to an increase in energy level and the amount of continuum radiation.

Recombination Radiation This effect describes the radiation, which is emitted when a free electron recombines with the valence shell of an atom. A pronounced single spectral line is formed based on the discrete energy level of the atom. Since the electrons exhibit different kinetic energies, a Maxwell distributed broad spectrum is created.

High-Pressure and Line Broadening Another emission effect is the broadening of spectral lines, which describes the spread of photon energy around the single spectral line. This fact represents the extent of the single spectral line to a range of wavelengths. Both temperature and pressure are raised with the energy level. This causes a higher collision probability. Energy levels are slightly offset by emission. This effect is called Stark broadening.
Line broadening is an indicator of the increase in the energy levels caused by an increase in temperature and pressure. Fig. 2.2 visualizes the effect of the spectral lines, as more particle collisions occur, broadening the spectral lines as explained above.
Natural broadening is another effect, which is caused by Heisenberg's law of uncertainty. The energy level and lifetime of a particle are not exactly known. Upon the spontaneous decay of a non-discrete energy level, a spread is created. Furthermore, there is the thermal Doppler effect, describing the broadening caused by the growth of the overall energy level in the plasma ([60]).

Table 2.1: Plasma ions of three highest UV wavelength peaks within in the spectral area from 230 nm to 380 nm.

Wavelength [nm]	**Ion**
313.9	Ar II
383.5	Ar II
357.6	Ar II

The NIST[7] atomic lines database is used to identify the ions in the plasma by defining the process gas and the spectral window ([61]). The obtained data from the NIST database is compared to the measured spectral data. As an example Tab. 2.1 shows the photon generation of argon II ions.
The optical properties of the plasma are measured non-invasively via OES. It is a method analyzing the spectrum of an emitting source (in this case the plasma) at certain wavelengths. A conical or cylindrical region of the plasma is measured in line-of-sight. From the obtained data the amount of a given element contained in the source can be extracted. Based on specific characteristics of the element different temperature types can be calculated: rotational T_{Rot}, vibrational T_{Vib} and electron T_{El}. The vibrational and electron temperature are not calculated within this work.
The rotational temperature T_{Rot} is caused by the redistribution of the rotational states, which can be estimated by a Boltzmann distribution. This temperature is proportional to the distribution function $N(J)$ of the rotational states around a molecule.

$$N(J) \sim (2J+1)e^{\frac{-ghc}{kT_{\text{Rot}}}} \tag{2.29}$$

J describes the rotational quantum number, g the statistical weight, c the speed of light c, h Planck's constant and k the Boltzmann constant. In most cases, the rotational temperature is almost equal to the gas temperature, if the translational-rotational equilibrium is fulfilled. It is assumed, that the investigated plasmas in this paper fulfills this equilibrium.
To calculate the rotational temperature from a rotational emission band the intensity distribution I is defined as

$$I = \frac{C}{Q_{\text{rot}}}\frac{S_{\text{J}}}{\lambda^4}\,\exp\,(-\frac{F(J')\,h\,c}{k\,T_{\text{rot}}}). \tag{2.30}$$

[7]National Institutes for Standards and Technology

C is a constant, Q_{rot} is the statistical sum, S_{J} is the Hönl-London factor, λ is the transition wavelength, $F(J')$ is the rotational energy term and J' is the upper rotational level. This equation allows the calculation of T_{rot} by the Boltzmann plot. More details on the rotational temperature can be found in [62], [63] and [64].
For a given molecule, rotational constants are accessible for the determination of the rotational temperature. In this paper the rotational temperature is determined by the hydroxyl-line around 310 nm. The rotational peaks are extracted from the spectral measurements and then fitted in a Boltzmann plot.
Spectral emission are also caused by vibrational movements of particles within a molecule. From these movements, the vibrational temperature T_{vib} can be determined by assuming a Boltzmann distribution of the vibrational bands. The vibrational temperature is defined as the sum of the vibrational quantum number ν'' and is given by

$$\sum_{\nu''} \frac{I_{\mathrm{li}}}{\nu^4} \sim \exp\left(-g(\nu'')\,\frac{h\,c}{k\,T_{\mathrm{vib}}}\right). \tag{2.31}$$

I_{li} is the line emission intensity, ν the frequency of the spectral line and g the statistical weight.

2.2 Fundamentals of Lighting Technology

This section explains the basic lighting properties based on the plasma energy emissions characterized in the prior section. Basic definitions of lighting properties are given to categorize the results of the spectral measurements.
An important distinction has to be made for the perception of the light between radiometric and photometric. Radiometry describes the measurements of the electro-magnetic spectrum, e.g. the visible light spectrum. Photometry is the measurement of light as perceived by the human eye. The measurements are weighted by the spectral luminous efficiency function to be converted from the radiometric units (e.g. radiant energy) to their photometric counterparts. This function represents the sensitivity of the human eye. All measurements in this chapter are photometric. More details on the basic units can be found in [65].

2.2.1 Luminous Flux

The luminous flux is defined as the amount of light emitted from a light source during a given time interval. Its SI unit is Lumen. In contrast to the radiant flux, which specifies the energy emitted, transmitted or reflected per unit time, the luminous flux is weighted by the sensitivity curve ($V(\lambda)$) of the human eye, with λ for the wavelength. The luminous flux Φ_{Light} is photometric, while the radiant flux is a radiometric measure. More details on this curve can be found in [66].

$$\Phi_{\mathrm{Light}} = K_{\mathrm{m}} \int_{380nm}^{760nm} V(\lambda) \, \frac{\mathrm{d}\Phi_{\mathrm{e}}(\lambda)}{\mathrm{d}\lambda} \, \mathrm{d}\lambda \tag{2.32}$$

K_{m} is a scaling factor ($683\,\mathrm{lm\,W^{-1}}$) for the human eye.

Table 2.2: Light efficacy for several lighting sources.

Light source	**Luminous flux** lm
candle	10
100 W incandescent light bulb	1300
D8S automotive headlight	2000
sun	3.7×10^{28}

An Ulbricht sphere is a measuring device, consisting of a hollow sphere into which the lamp is mounted to measure the luminous flux. By coating the inner wall with a reflective paint, the integrated illuminance is bundled into one point to be measured.
Typical values for the luminous flux of different light source are given in 2.2. All values are taken from [67].

2.2.2 Illuminance

The illuminance E_{illum} of a light source is defined as the luminous flux $\partial\phi_{\text{e}}$ incident on a surface ∂A:

$$E_{\text{illum}} = \frac{\partial\phi_{\text{e}}}{\partial A}. \tag{2.33}$$

For the measurements, the detector surface of the spectrometer $\partial A = A_{\text{Det}}$ is used. All calculations are made by the Ocean Optics Spectra Suite software, which integrates the intensity ϕ_{e} of all spectral lines in a specified interval based on the Eq. (2.33).

2.2.3 Luminous Efficacy

For lighting sources, the efficacy η_{Light} describes the ratio of the radiant flux to the input power. The electric efficiency η of a system is defined as the ratio of output to input power

$$\eta = \frac{P_{\text{out}}}{P_{\text{in}}}, \tag{2.34}$$

$$\eta_{\text{Light}} = \frac{\Phi_{\text{Light}}}{P_{\text{in}}}. \tag{2.35}$$

Its SI unit is Lumen per watt.
In this thesis, the efficacy is defined as the RF input power to the light output. Since all light properties are determined using a spectrometer, only the illuminance is measured. The integral of Eq. (2.32) is simplified to a 4-pi-approximation with the measured illuminance of Eq. (2.33) to calculate the luminous flux:

$$\Phi_{\text{Light}} \approx 4\,\pi\, r_{\text{Sphere}}^2\, E_{\text{illuminance}} \tag{2.36}$$

It results in the surface of a sphere with a radius r_{Sphere}, which is also the distance of the spectrometer to the lamp. It is assumed that the illuminance is constant on the sphere. Therefore this method is only an approximation.

Table 2.3: Light efficacy for several lighting sources.

Lamp	**Efficacy** lmW^{-1}
incandescent light bulb	10
domestic halogen lamp	15-27
D8S automotive headlight	80
LED	60-140

Typical values for the efficacy of commercial lamps are described in Tab. 2.3.

2.3 Wave-Guide and Network Theory

This section deals with the theoretical background of the high-frequency technology required to characterize the electrical parameters of the plasma. Furthermore, the base point impedance[8] is determined to simulate and design purposed-built networks for the ignition and operation. Moreover, the basics of the large-signal S-parameter measuring technique are given. Measurements with this technique allow the determination of the plasma impedance during operation. Further details can be found in [68], [69] and [70].

2.3.1 Transmission Line Theory

To calculate the electrical properties of a given circuit at DC and lower frequencies, lumped elements are used. By increasing the frequency the wavelength of a signal decreases, leading to phase differences and thus different signal strengths on the circuit. Therefore circuit theory cannot be applied. At this point, the telegrapher's equation is used. It is derived from Maxwell's equations, and it is assumed that a transmission line consists of an infinitesimal size two-port network in series. A transmission line describes a two-port network connecting a source to a load. These small networks are composed of a series resistance representing the losses of the line and a series inductance for the self-induction. Dielectric losses are represented by a shunt resistance connected to ground. A shunt capacitance describes the coupling between the conductor and ground. More details on the transmission line theory can be found in [69].

2.3.2 Characteristic Impedance

The ratio of the electric and magnetic field of a transverse EM-wave traveling through a medium is constant. This constant is called the characteristic impedance Z_0 and represents the propagation of EM waves for this medium. It is described as

$$Z_0 = \frac{\vec{E}}{\vec{H}} \tag{2.37}$$

[8] For antennas this is called feed-point impedance

The wave impedance of free space is determined by the plane-wave solution of Maxwell's equation.

$$Z_0 = \frac{1}{\varepsilon_0 \, c_0} = 120 \cdot \pi \Omega \tag{2.38}$$

Any transmission line exhibits a characteristic wave impedance determined by its topology and configuration.
The transmission line theory ([71]) describes the characteristic wave impedance of a line as the influence of the line on an electro-magnetic wave passing through.

$$\gamma = \alpha + j\,\beta = \sqrt{(R' - j\,\omega\,L')(G' + j\,\omega\,C')} \tag{2.39}$$

γ is the propagation, α the attenuation factor, β the angle measure, R' the resistance coating, L' the inductance covering, G' is the conductance and C' is the capacitance per length unit.
In this thesis, all prototypes consist of a coaxial transmission line to transfer the power from the source to the plasma. The characteristic impedance of the coaxial transmission line is calculated via

$$Z_{\mathrm{Coax}} = \sqrt{\frac{\mu_{\mathrm{r}}}{\varepsilon_{\mathrm{r}}}} 60 \ln \frac{D}{d} = \frac{Z_0}{2\pi\sqrt{\varepsilon_{\mathrm{r}}}} \ln \frac{D}{d}. \tag{2.40}$$

Further information can be found in [72] and [68] and [71].

2.3.3 Scattering Parameters

The behavior of waves in the GHz area can be expressed by the same principles and laws as for optical waves. Microwaves are reflected by an abrupt change of the wave impedance or a change in the dielectric constant of the material like optical waves. At the interface between materials, the microwaves are refracted changing amplitude and phase. This behavior represents the electrical properties of linear electrical networks and components. Each part consists of some port where microwaves are either incident or reflected. The ratios of these waves are normalized to the wave impedance and called scattering parameters (S-parameters). Their indices describe the origin and the goal of the waves. For example, S_{11} is defined as

the ratio of the reflected b_1 from port 1 to the inserted a_1 power at port 1

$$S_{11} = \frac{b_1}{a_1}. \tag{2.41}$$

These parameters specify the impedance of a plasma. More details on these parameters can be found in [68].
As referred to [40] the reflection coefficient S_{11} is used to calculate the plasma impedance Z_{in} in relation to a reference impedance Z_0 and is defined as

$$S_{11} = \frac{Z_{\text{in}} - Z_0}{Z_{\text{in}} + Z_0}. \tag{2.42}$$

Often S-parameters are expressed logarithmically by

$$S_{11}^{\text{dB}} = 20 \cdot \log |S_{11}| dB. \tag{2.43}$$

Scattering parameters of a network are written in a matrix. The following matrix shows the scattering parameters of a special[9] two-port network

$$[S_{\text{T}}] = \begin{bmatrix} 0 & 1 \\ 1 & 0 \end{bmatrix} \tag{2.44}$$

Results of a network chain are calculated by summing the single matrices. Standard matrix operations can be applied.

2.3.4 De-Embedding and Extraction of Plasma Base Point Impedance

Since chained S-parameter matrices $[\Sigma]$ characterize the serial connection of their corresponding network, the inverse multiplication of a matrix can be used to extract the single matrix within a chain.
This process is called de-embedding and describes the technique of virtually moving a reference plane to extract the desired S-parameters. This process is illustrated in Fig. 2.3 using the example of a plasma jet.
Based on the reference plane A the S-parameters are the combined S-parameters Σ_{Jet} of the RF network $\Sigma_{\text{a, Measurement}}$ and the plasma Σ_{b}. First, the plasma jet is

[9]Thru-Connection: perfect match, free from losses and 0° electrical length

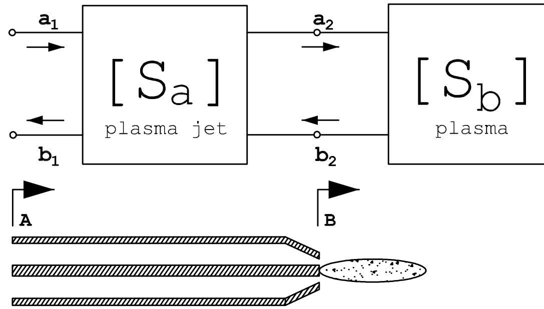

Figure 2.3: Graphical representation of the de-embedding process using the example of a plasma jet during operation. Different reference planes A and B are indicated as well as the different forward and reflected waves (a, b).

measured without an active plasma and then modeled in a circuit simulator. Now, the assessment of the jet during plasma operation is de-embedded by subtracting the model of the jet from the second measurement. The matrix operation for this de-embedding process is

$$[\Sigma_{\mathrm{b}}] \cdot [\Sigma_{\mathrm{Jet}}] = [\Sigma_{\mathrm{a,\,Measurement}}]. \tag{2.45}$$

The network consists of a series of coaxial lines which are modeled in ADS using the real geometrical properties of the probe. This is done by changing the line length of each element to its negative counterpart (2 mm becomes −2 mm).
The probe's accordance is verified against the simulation model using a vector network analyzer. Reference measurements are obtained by shortening the end with a metal cap. Next, the test object, which generates the plasma, is mounted onto the probe. A vector network analyzer measures the combined impedance response of both the system topologies within the desired frequency range. The measurement data is transferred into the circuit simulator for extraction of the plasma parameters. A full de-embedding of the probe requires a transmission measurement. Since the probe is asymmetric the simulation is only fitted to the measurement. More details on the de-embedding technique can be found in [73].

The measured value of (2.41) is inserted into (2.42) and transposed into

$$Z_{\text{in}} = Z_0 \cdot \frac{1 + \frac{b_1}{a_1}}{1 - \frac{b_1}{a_1}}, \tag{2.46}$$

so that the plasma impedance can be calculated. Eq. (2.45) provides the impedance for the reference plane at the plug of the jet. The results obtained from the de-embedding process are used to develop a purpose-built RF network. It is fitted to the plasma base point impedance at the specified input power. More details on the development are described later in Chapter 3.
The accuracy of the plasma's electrical properties is dependent on the measuring error. The vector network analyzer is calibrated before every measurement. This procedure is repeated with the same calibration standards (open, short and match). A ripple of the amplitude on a calibrated transmission line verifies the calibration. It provides information on the measuring error for both amplitude and phase. In addition, the repeatability of the measurement is verified.

2.3.5 Plasma Fitting using Lumped Elements and Lossy Dielectrics

Electric properties of plasmas are dependent on many variables such as temperature, input power, species, and pressure. To develop an RF network, the representation of the plasma in a simulator is required. Each change in the variables has to be adjusted in its simulator equivalent. Therefore the plasma has to be assessed at the desired requirements.
As described in Section 2.1.6 and 2.1.7 the electric properties of a plasma can be represented using conductivity, permittivity, and electric loss tangent. Simulations have shown that these electrical parameters are sufficient to serve as the main plasma representations.
The fitting process is split into two parts: the simulation of the circuit and FEM[10]. For the plasma, the circuit simulation is based on a combination of lumped elements to match the base point impedance. It is shown, that a series resonance circuit satisfies the needs of a frequency-dependent circuit simulation. In FEM simulations the physical dimensions of the plasma are rebuilt in combination with a lossy dielectric material[11], where a relative permittivity of smaller than 1 exists.

[10] Finite Element Method
[11] Bulk conductivity and relative permittivity are adapted to the plasma

These artificial materials were first introduced in [74] to fit the simulated electrical properties of a plasma to those measured. In this work, the plasma is represented by a rodded medium, which substitutes the plasma to a set of thin parallel wires. Further analysis of this phenomena is described in [75]. Lossy dielectrics to simulate a plasma are also described in [76], [77], [78] and [79]. It has to be noted that this is a simplified characterization, since the plasma parameters such as temperature, particle density and pressure are not taken into account.

Table 2.4: Overview of period times, wavelength and the relative changes of the wavelength to the 1.3 GHz band for the investigated bands around: 1.3, 2.45 and 3.5 GHz. All values are calculated for vacuum conditions.

Frequency GHz	**Period Time** ns	**Wavelength** mm	**Relative Change**
1.3	0.77	230	100 %
2.45	0.4	122	49 %
3.5	0.285	86	29 %

2.4 Theory for Different Frequencies

Commercial applications are limited to the ISM band around 2.45 GHz[12] because no regulations are required concerning the radiation of the energy. Dimensions of both plasma and generator are restricted to the frequency of the ISM band. As described in [40], the frequency influences the size of the plasma and the electron density. This thesis focuses on the investigation of different frequencies from 1.3 to 3.5 GHz to generate microwave plasmas. Frequencies are chosen due to the persistent gap of about 1 GHz to the ISM band, which is sufficient to show the impact. This section focuses on the effects causing the difference in geometrical expansion of the plasma.

During the measurements, the amplitude of the electric field generating the plasma is corrected by the impedance matching. The amplitude is assumed to be constant at the calibrated reference plane to compare the consequences of the different frequencies. This assumption is based on the measurements using a calibrated power meter with a 50 Ω load. In Tab. 2.4 the different properties of the frequencies and their relative changes to 1.3 GHz are described.

2.4.1 Frequency Effects on Electrons

Within a plasma, the geometrical expansion is mainly determined by the movement of an electron as charge carrier. A simplified model is created to visualize the frequency-dependent effects on a single electron in a one-dimensional electric field of constant amplitude at different excitation frequencies. The model is based

[12] (2.4 GHz to 2.485 GHz

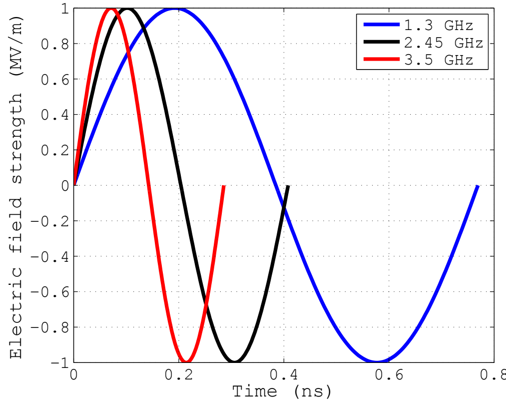

(a) Electric field strength of an electron at different frequencies

Figure 2.4: Electric field strength of an electron in a one-dimensional electric field excited to a field strength of $1 \times 10^6\,\mathrm{V\,m^{-1}}$ at the respective frequency.

on the work of [80], where it was calculated for a fixed frequency of 2.45 GHz. Although the model cannot be applied directly to a plasma, because of the complex interaction with other particles, it visualizes the frequency-dependent changes described in Chapter 5.
The effective force on a free-floating electron caused by an electric field is calculated by

$$m_e \frac{dv_e}{dt} = -e\,\vec{E}\,e^{j\,\omega_{\mathrm{RF}}\,t}. \tag{2.47}$$

v_e is the velocity of the electron per time unit t. In Fig. 2.4 the electric field strength of a free-floating electron is plotted. As shown in Tab. 2.4, the wavelength is smaller at higher frequencies. The gradient of the electric field is also steeper at higher frequencies.

2.4.2 Particle Interaction in a Plasma

In a plasma, the movement of an electron as free charge carrier is influenced by many factors such as collisions with other particles, changes of inner energy or recombination. Therefore the model presented in the previous chapter is shown

for visualization purposes only. In this thesis, the visible effects of the different frequencies on the plasma are described only. It provides explanations and suggestions based on the observations.
Sec. 2.1.6 explains how the effective conductivity and effective permittivity of a plasma depend on the excitation frequency of the electric field $\vec{E}$ (Eq. (2.19) and (2.25)). Therefore the influence of these parameters is the first to be analyzed in this thesis. FEM simulations of several plasma applications will be presented in combination with a detailed analysis of the parameters in Chapter 4. By determining the RF conductivity, it might be possible to extract other plasma parameters such as the mean free path λ_{MFP} or the plasma frequency ω_{p}.

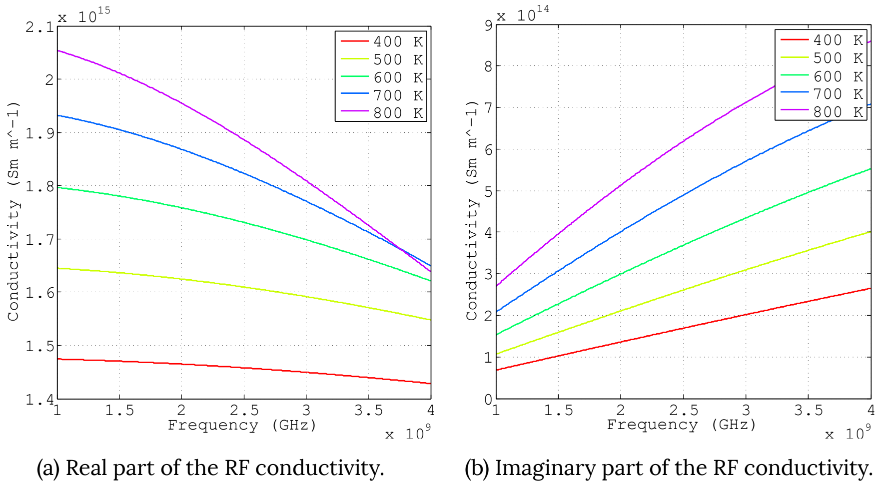

(a) Real part of the RF conductivity. (b) Imaginary part of the RF conductivity.

Figure 2.5: Resulting RF conductivity over the frequency for different temperatures.

To emphasize the influence of the frequency on the RF conductivity, the real and the imaginary part are plotted in Fig. 2.5. For this, Eq. (2.19) presented earlier in this chapter has been used. It is assumed that an argon plasma at 1 bar has an ionization rate of 1×10^{-8}. All other values are derived from the equations. Since these values are chosen arbitrarily the plot is serving quantity purposes only. For the investigated interval from 1.3 GHz to 3.5 GHz the highest values are located at 1.3 GHz for the real part. The imaginary part increases almost linearly with the frequency being in good agreement with Eq. (2.19).

The real part of the conductivity decreases in inverse proportion to the frequency, while the imaginary part is not influenced in this way. This supports the fact that a reduction of the wavelength has an influence on the plasma properties such as the mean free path and the plasma frequency. Considering the direct influence, an overall reduction of the plasma size is apparent at higher frequencies.
The different lines represent different temperatures from 300 K to 800 K. Particle density increases with the temperature and thus the conductivity. The influence of the temperature on the real and imaginary part is not linear. An increase from 300 to 800 K raises the real part from 1.5×10^{12} to $2.1 \times 10^{12}\,\mathrm{S\,m^{-1}}$ and the imaginary part from 1×10^{12} to $3 \times 10^{12}\,\mathrm{S\,m^{-1}}$. Therefore the frequency-dependent effects are independent of changes of the temperature.

2.4.3 Hot-S Measuring Environment

All plasma measurements are executed using the hot S-parameter technique, which is presented in [81]. This technique is usually for in-action measurements for the impedance matching of active amplifiers by superimposing a large signal on the small signal sweep of the network analyzer. It enables extraction of the plasma S-parameters during operation.
The large signal drives the DUT[13] at a particular frequency. In this thesis, the plasma represents the device.

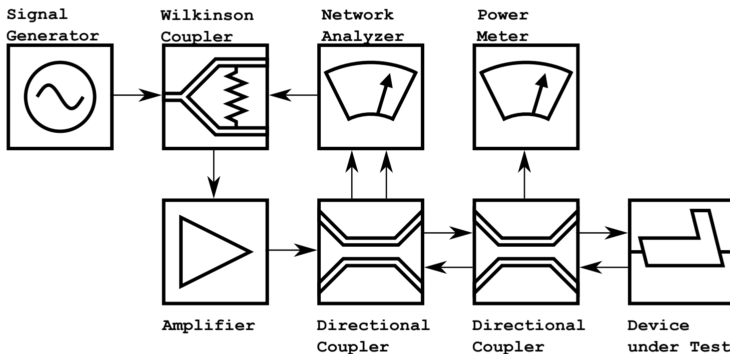

Figure 2.6: Block diagram of the large signal S-parameter measuring environment for the determination of microwave plasma properties.

[13] Device Under Test

A simplified box diagram can be found Fig. 2.6. The network analyzer signal sweep (small signal) is overlayed by the large signal. As described in Section 2.3.4 the ratio of the forward and reflected wave calculates the complex S_{11}-parameter.
For the extraction, a directional coupler provides these two wave quantities after the output port of the amplifier. Then, these waves are routed back to the network analyzer where the frequency dependent complex impedance is measured and displayed. The power is also measured with a mono-directional coupler at the output of the amplifier.
The single port calibration of the network analyzer can be made with calibration kit[14]. It moves the reference plane of the impedance to the desired point.
The equipment at Aachen University of Applied Sciences consists of a Rohde & Schwarz ZVM vector network analyzer for S-parameters measurements on user-defined ports. An Agilent E4421B signal generator drives a custom IMP 200 W amplifier for the large-signal. The signal passes through the Narda 3043B-20 coaxial directional coupler, where the output power is measured using a Gigatronics 8543C power meter in combination with an HP 80401A power head.
Frequencies can be swept over a 300 MHz bandwidth with a 20 dB difference of the large and small signal. The system has a dynamic of 85 dB at an IF bandwidth of 1 kHz. More information on the equipment used and further technical details can be found in [38].

[14] Open, Short and Matched

Figure 2.7: Large S-parameter measuring environment.

Fig. 2.7 shows the measuring hardware, which is limited to the ISM-band around 2.45 GHz. The extension to 1.3 and 3.5 GHz is presented in Section 4.2 along with the hardware used and a more detailed explanation of the measuring dynamics. Power measurements are made with an HP power meter, an HP 8481, an HP 8481D power sensor and a Narda 3022 bi-directional coupler.
The power meter was calibrated and the offset was set to match the different losses of the directional coupler at the different frequency bands to gauge the absolute power levels.

2.4.4 Analysis of System Error

Most of the RF-measurements presented in this thesis are made using a vector network analyzer (VNWA). As described in Chapter 2.4.3 the VNWA is calibrated before each measurement. With the acquired data the de-embedding process is started, whose accuracy is described in Chapter 2.3.4. All measurements in this chapter using the VNWA have a source matching of 30 dB and better. More details on this method can be found in [82]
All measurements presented in Chapter 5 are conducted with a wave-guide tuner. The tuner elements are set in a way that the best matching of the amplifier to the base point impedance of the plasma is possible. Since the wave-guide and the probe network have losses, the relative amount of the matching is added to the overall variance. The measuring accuracy of the power meter is recognized in this measuring error. S_{11} has a minimum matching of -15 dB, which is about 1% of the reflected power.

In addition, thermal and optical measurements are presented for each of the plasmas. All optical measurements are recorded using a BWTek Exemplar Plus spectrometer. In the final configuration report, a maximum deviation of 0.88 nm for the whole spectrum from the calibration source is measured. It adds a maximum error of 0.4% to the relative system error.
The distance of the spectrometer sensor to the DUT is stated for each measurement. Since the distance is measured manually using a caliper a variation of ± 0.01 m is assumed. This amount adds 1% to the overall relative measuring error. In the case of the plasma jet, an additional lens focuses the radiant intensity on the cosine corrector of the spectrometer. The combined overall systematic error is 5.4% for all optical measurements.
Thermal measurements are made using a FLIR T-335 infrared camera, which has an inaccuracy of ± 2%. To measure the glass surface temperature the emissivity factor is set to 0.97. A combined error of 6.4% for all measurements using the infrared camera has to be added to the results.

Chapter 3

Microwave Plasma Basics and Applications at 2.45 GHz

This chapter deals with the development of microwave plasma applications inside the ISM-band around 2.45 GHz. The basics of microwave plasmas are introduced as well as the two main plasma states: ignition and operation. Based on these states, RF-networks are presented along with an investigation on the ignition field strength.
The development is based on the large signal S-parameter measurements using a purpose-built 50 Ω probe. After this, the de-embedding and plasma fitting process in a circuit and FEM simulation is presented. This process is important since it results in the determination of the plasma base point impedance that is necessary for the development of a matching and bi-static network.
On the example of an electrode-less UV-Lamp, the basics of a bi-static[1] network is presented, which is a combined network for ignition and operation at different frequencies. For the ignition, a high field strength at the tip of the driving electrode is required, and for the operation a proper matching of the plasma base point impedance to the network wave impedance is necessary, usually around 50 Ω. These states are located at different frequencies within the ISM-band around

[1]The term bi-static is derived from the ignition and the operation state of the plasma, which are mono-static states

2.45 GHz. This process has been used and validated in several publications ([9], [34] and [38]).
Based on the example of a domestic electrode-less high-pressure for general lighting purposes (short form: DHPL) and the electrode-less UV-Lamp, the results of the bi-static network development is presented. All of these works have been made in the course of this thesis.
The chapter is concluded by the presentation of an optimization technique using a superimposed modulated signal as well as the optical and thermal measurement results of both lamp prototypes. In case of the UV-Lamp, a high-pressure is achieved within the burner and an UV-efficacy of 50%. The DHPL achieves an efficacy of 135 $\mathrm{lm\,W^{-1}}$ at 40 W which higher than commercially available light emitting diodes (LEDs).

3.1 Bi-Static Network for Ignition and Operation of a Microwave Plasma

This section deals with the different states[2] of a microwave plasma and which ensued requirements for an RF-network. Main goal is the fusion of the mono-static[3] states into a single bi-static[4] network.

3.1.1 Introduction of the Main Plasma States

The main goal of every workflow is a working prototype of a network, that is suitable for at least one of the states listed below.

- Ignition: electric field strength has to surpass the breakdown strength of the gas.
- Operation: typical 50 Ω impedance of the amplifier output has to be matched to plasma base point impedance.
- Bi-static: combined network for both states, each state is located at a different frequency.

Goals are set by the applications themselves. Ignition networks are typically used for the RF spark plug ([83]), while operation networks can be used in a plasma jet and a lamp. The first free charge carriers of a mono-static network for the operation state are generated by an external high-voltage impulse. These mono-static operation networks are used for research purposes mostly and to probe the plasma for the development of the final bi-static network. More information on each network type and examples for different applications will be presented later in this chapter.
Simulation of the network is conducted in the circuit and FEM simulator. In both simulators, the networks for ignition and operation comprise of a 50 Ω plug to which a coaxial conductor is connected. Depending on the state, the network substituted by different terminations. These details are included in the description of the particular state.

[2]Ignition and operation
[3]Mono-static refers to a single state of the plasma
[4]Bi-static combines the two states at different frequencies

3.1.2 Amplitude Locked Loop as a Requirement for the Bi-Static Network

By design the two states of a bi-static network are located at different frequencies. A constant energy flow has to be ensured if a plasma is to be sustained. If a plasma is ignited at one frequency and operated at another, the plasma would collapse, since the power for the operation is not sufficient. Adjustments of the frequency have to be made manually. Detection of changes is enabled by an amplitude locked loop (ALL) controlling the frequency of the oscillator. The functionality can be compared to a phase locked loop (PLL): In a pre-set interval the frequency is swept and the ratio of the transmitted and reflected wave is detected. At the point of the best matching, the ALL locks and the oscillator is set to the detected frequency. The ALL compensates for changes of the frequency due to thermal drift of an oscillator or variances in the RF-network. More details on the ALL are described in [84] and [85].

3.1.3 Meta-States in a Microwave Plasma

For a plasma in an enclosed vessel, like the bulb of a lamp, further states are existing. The transition between the ignition of the plasma and the operating point is called the start-up phase. During this phase the energy level inside the plasma increases. This results in a raise of the vapor pressure of the involved species until ionization reaches a certain threshold. During start-up, the impedance of the microwave plasma constantly changes and shifts the frequency too. These shifts of the frequency are supported by the ALL.
If a plasma was active previously in an enclosed vessel, the conditions for the ignition change. This state is called hot-restrike. Based on the ideal gas law the pressure is proportional to the gas temperature and therefore a higher electric field strength is required to re-ignite the plasma. A higher temperature also reduces the amount of energy necessary to generate free charge carriers. Combining these two contrasting effects, it depends on the application itself on how difficult a hot-restrike can be. More details on the breakdown and ignition of a plasma using RF sources can be found in [86], [87] and [88].

3.1.4 Generation of Free Charge Carrier to Ignite a Microwave Plasma

In the first part of the bi-static network development process, the ignition is investigated. The objective of the ignition is the generation of free charge carriers by a sufficient electric field strength to create the first electron avalanche. For the approximation of the required field strength, Paschen's law is used, as described in Chapter 2.1.2. Since the breakdown voltage of gases varies at higher frequencies, the approximations from [86] are introduced.

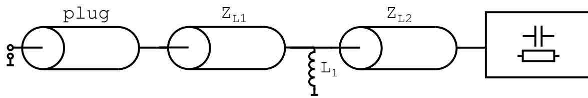

Figure 3.1: Schematic view of a circuit simulation for the ignition state.

The sketch of an exemplary ignition simulation network is shown in Fig. 3.1. Connected to the plug is the coaxial line Z_{L1} , which is for structure supporting purposes only. The main network consists of the inductor L_1, which shortens the network, because of its low resistance. This short is transformed by the coaxial line Z_2. It has a length of $\lambda/4$ transforming the short of L_1 to an open. The network is terminated by a high-value resistor or a capacitance depending on the DUT. Voltage is calculated by a harmonic balance simulation ([89]). The FEM simulation uses vacuum as the material to represent the physical conditions of the DUT. More details on ignition can be found in [55] and [90].

3.1.4.1 Ignition Simulation for Power Levels up to 20 Watt

In the course of this thesis, the required ignition field strength has been investigated. Based on Paschen's law for the breakdown of gases, a certain electric field strength is required for the ignition of a plasma. This field strength depends on the network and the output power of the amplifier. Compared to an incandescent light bulb, newer generations of domestic lighting solutions, such as LED, reduce the required power. Therefore a limitation of the amplifier's output power is necessary.

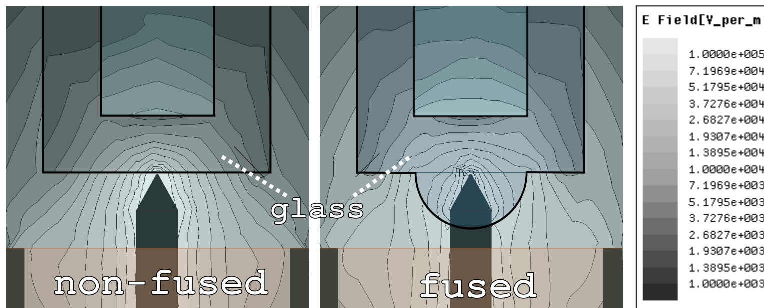

Figure 3.2: Simulated ignition field strength for the unbalanced electrode configuration using a non-fused and a fused set-up at 2.45 GHz and 15 W. Local electric field of the fused electrode is higher in the burner. The outlines are highlighted in black.

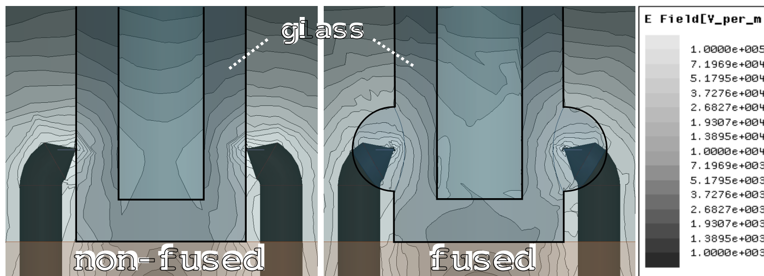

Figure 3.3: Balanced topology to simulate the ignition field strength at 2.45 GHz and 15 W. Fusing the electrode into the glass increases the maximum field strength by a factor of 1.5. Outlines are highlighted in black,

In order to optimize the electric field strength inside the bulb of the lamp at the same power level, different network structures are simulated in Ansoft HFSS. A differential (balanced) and a coaxial (unbalanced) structure are built and parametrized. Tips of the electrodes are sharpened to increase the local field strength. For both structures, the impact of melting the electrode into the glass is analyzed. Fig. 3.2 and Fig. 3.3 display the chosen electrode configurations for the unbalanced and balanced modes and the effect of fusing the electrodes into the glass. An input of 15 W for the unbalanced topology is set and 2x 7.5 W for the balanced topology, respectively. The geometrical properties in this section are chosen to emphasize

the differences in the field distribution and strength by using different network topologies and fused or non-fused electrodes.

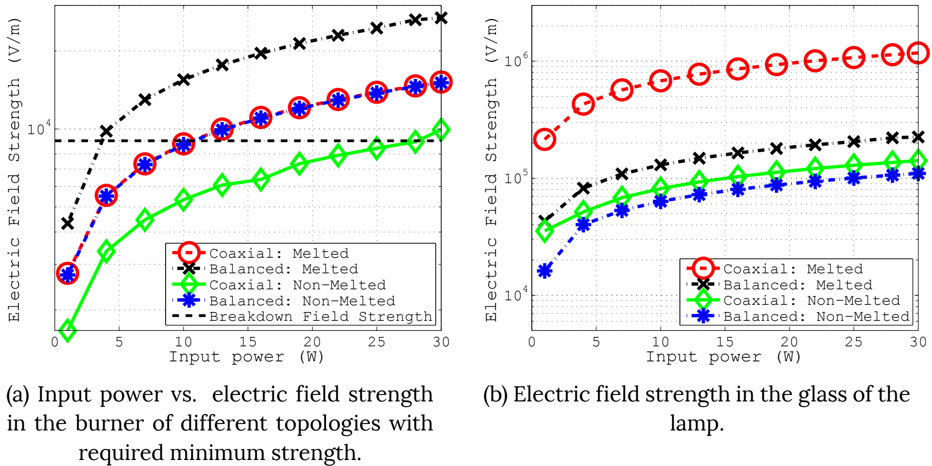

(a) Input power vs. electric field strength in the burner of different topologies with required minimum strength.

(b) Electric field strength in the glass of the lamp.

Figure 3.4: Simulated electric field strength inside the burner and glass body for the high-pressure lamp with a pressure of 20 mbar using argon.

The comparison of the maximum electric field strength in the glass and the burner is plotted in Fig. 3.4a and 3.4b. Maximum values are calculated inside the volumes of the burner and the glass body for the different input power levels. For the balanced topology, the combined input power is plotted. In Fig. 3.4a the field strength within the burner is plotted for the different simulated topologies. As mentioned above, the ignition field strength is investigated for the high-pressure lamp with a gas pressure of 20 mbar. A black dotted line indicates the required ignition field strength. Fusing the electrode into the glass increases the field strength by a factor of 2. In turn, this leads to a reduction of the necessary power by the same factor to ignite a plasma. A fused unbalanced structure exhibits the same field strength as a balanced topology. By fusing the balanced topology into the glass, the field strength is almost doubled again. Using the melted unbalanced topology an input power of about 12 W is required to surpass the ignition field strength of argon.
Additional simulation runs determine the maximum field strength of the glass to see if the material could be damaged. With $1 \times 10^6\,\mathrm{V\,m^{-1}}$ the maximum field

strength is achieved with an unbalanced electrode melted into the glass. Comparing this value to the dielectric strength of glass (about $4 \times 10^7\,\mathrm{V\,m^{-1}}$) shows that the field strength is not sufficient to damage the glass ([91]).

3.1.5 Operation of a Microwave Plasma by Electric Fields

The second part of the bi-static network development is the impedance matching during the operation of the plasma. After the corresponding plasma base point impedance determination using a purpose-built probe network, the values are entered in the circuit and FEM simulator.

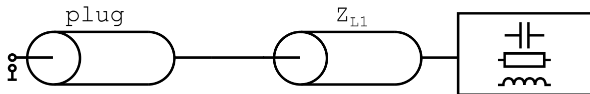

Figure 3.5: Schematic view of the operation network for probing the plasma.

Representation of the network in the circuit simulator is illustrated in Fig. 3.5. It consists of a single coaxial line Z_{L1}, whose radius and length is fitted to match the base point impedance of the plasma. Lumped elements such as capacitors, resistors, and inductors substitute the electric properties of the plasma. The material of the FEM simulation is switched to a lossy dielectric as described in Chapter 2.3.5. More information on these plasma representations can be found in [9].

3.1.5.1 Probe Networks for the Measurement of the Base Point Impedance

(a) $50\,\Omega$ probe for the determination of plasma impedances using the large signal S-parameter technique.

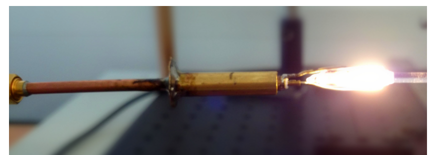

(b) Differential probe with variable balanced output impedance matching network.

Figure 3.6: Unbalanced and balanced probe approaches to transfer power from the amplifier to the plasma.

The determination of the plasma base point impedance is the first step to develop an RF-network for the desired application. As described in Chapter 2, the base point impedance has to be extracted from a measurement at the desired input power. A first approach is to build a 50 Ω probe, transferring the power from the amplifier to the lamp, since the plasma parameters are unknown in advance. An example probe can be found in Fig. 3.6a. Since the operating range of most applications is known, the power level coupled into the plasma is corrected by the measured reflection coefficient. In addition, a tuning-line[5] can match the amplifier to the plasma impedance.

3.1.5.2 Marchand Balun Network

In some cases, the power level coupled into the plasma using a 50 Ω probe is too low and therefore differential probes with a variation of the output impedance are designed and built during the works on this thesis. A probe is shown in Fig. 3.6b. A disadvantage is a more complex simulation set-up of this probe to determine the base point impedance. A Marchand sleeve balun is used in combination with

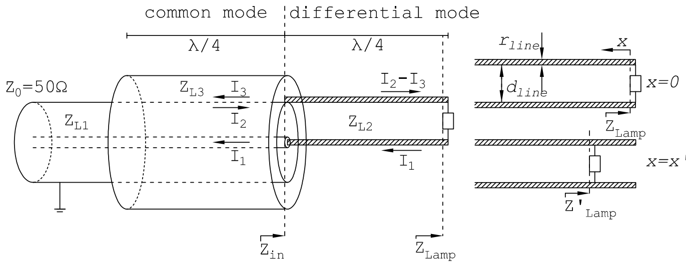

Figure 3.7: Schematic view of the Marchand balun and parallel transmission line. It has a length of $\lambda/4$ to enable variable wave impedance on the indicated X-axis. Sheath waves are suppressed by the extra outer conductor, which also converts the common to the differential mode.

a $\lambda/4$ parallel line ([92], [93]). This network transforms the unbalanced signal to a balanced signal. Marchand sleeve baluns[6] reduce sheath waves on the outer conductor and thus improve the efficiency. This network is used only to extract the electrical parameter of the high-pressure plasma inside the lamp. A schematic of

[5]Coaxial conductor with variable shunt inductors
[6]Balanced-Unbalanced Mode Converter

the used network is displayed in Fig. 3.7 in addition with the principle and a detailed view of the parallel transmission line.
For the circuit an equivalent voltage generator is created by the wave impedance $Z_{\mathrm{L1}} = Z_0 = 50\,\Omega$ and the current I_2. Z_{L1} acts as the internal resistance of the generator. After flowing through the parallel lines the current I_2 and sheath current I_3 are formed. Due to the $\lambda/4$-transformation the current I_3 sees an open-circuit with an infinite impedance, which is connected to the outer conductor of the 50 Ω line. Sheath waves are suppressed effectively. It results in a current of equal magnitude on the outer conductor and the sleeve, and shows a balanced operation by a phase shift of 180°.
Connected to the inner and outer conductor of the Marchand sleeve balun is a parallel line with a length of $\lambda/4$. The input impedance Z_{in} of a $\lambda/4$-transformer line is calculated by

$$Z_{\mathrm{in}} = \frac{Z_{\mathrm{L2}}^2}{Z_{\mathrm{Lamp}}} \tag{3.1}$$

using the wave impedance Z_{L2} and output impedance Z_{Lamp}. The impedance of parallel line wires with a radius of r_{line} at a distance of d_{line} is determined by

$$Z_{\mathrm{L2}} = \frac{120\,\Omega}{\sqrt{\varepsilon_{\mathrm{r}}}} \ln \frac{2\,r_{\mathrm{line}}}{d_{\mathrm{line}}}. \tag{3.2}$$

Both variables are indicated in Fig. 3.7. By moving the impedance Z_{Lamp} along the vector x, the electrical length of the parallel line as well as the lamp impedance is changed to Z'_{Lamp}. Using a distance $d_{\mathrm{line}} = 5\,\mathrm{mm}$ and a radius $r_{\mathrm{line}} = 1\,\mathrm{mm}$, the magnitude of the impedance is tunable over x between $50\,\mathrm{V\,A^{-1}}$ at the beginning and $1200\,\mathrm{V\,A^{-1}}$ at the end of the parallel line. This wide tuning range is independent from the impedance Z_{Lamp}.

3.1.6 Hardware Description of the Bi-Static Network for Ignition and Operation

Based on the simulation results of the base point impedance, the combined network for ignition and operation is designed. For this, the simulation is split into two parts: one for the ignition and one for the operation part of the bi-static network. All changes are applied to both parts to observe the particular impact.

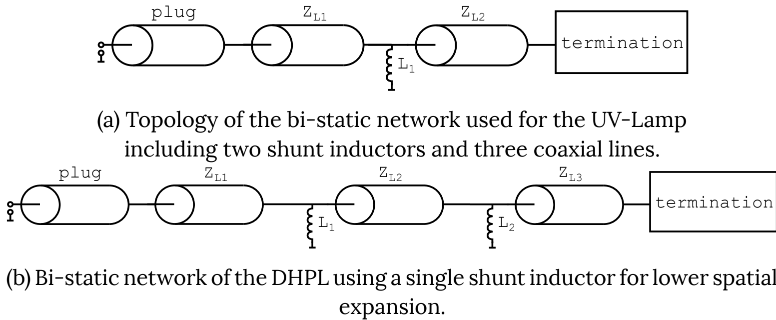

(a) Topology of the bi-static network used for the UV-Lamp including two shunt inductors and three coaxial lines.

(b) Bi-static network of the DHPL using a single shunt inductor for lower spatial expansion.

Figure 3.8: Different construction forms for the bi-static network.

For the bi-static network, two different network topologies are available. Fig. 3.8 shows a set-up with a single shunt inductor L_1. It provides the necessary transformation for the generation of the high field strength and the matching. After the ignition of the plasma, the electric properties of the network are changed in a way that most of the energy is coupled into the plasma. This set-up is better suited for smaller applications since its construction size is smaller than the dual shunt inductor set-up. The topology in Fig. 3.8 is preferred for higher power levels due to its rugged design. It features two inductors to enable the bi-static functionality. In the course of this chapter, both topologies are depicted for two different lamps at different power levels.
Another option is to include a series capacitance in the single shunt inductor topology. This set-up turned out to be too fragile due to its low reproducibility.
In this thesis, a modular construction kit was developed allowing an easy set-up of a new prototype. It utilizes the single shunt inductor topology. Shunt elements of different values in conjunction with inner coaxial conductors of different sizes cover the major areas of plasma applications. Examples of this construction kit are presented for the second generation UV-Lamp in this chapter and for the transmission network in Chapter 4.

3.2 Determination of the Base Point Impedance by Plasma Fitting

Electrical properties of microwave plasmas in operation states are influenced by many factors (power, pressure, gas flow etc.). As explained in Sec. 3.1.5 different networks are built to generate the necessary application requirements and probe the plasma. These measurements are de-embedded to extract the base-point impedance. This parameter sets the requirements for the impedance matching during operation of the bi-static network.
This section describes the determination of the base point impedance in a circuit and FEM simulator on the example of an electrode-less UV-Lamp. The network for the lamp has been developed during the works on this thesis. Further details on the UV-Lamp are presented in Sec. 3.3.1 along with the development of the bi-static network.
The next part of the base point impedance determination is split into the circuit and FEM simulation part. This splitting is necessary to reduce the development time. All major calculation steps are performed in the circuit simulation. After the fitting process in the circuit simulator, the starting values of the material properties are set accordingly in the FEM simulator.
Two steps are necessary to obtain the plasma parameters from the measured data:

- rebuilding of the probe in the simulators,
- de-embedding of the probe.

3.2.1 Lumped Element Model for Microwave Plasma Fitting in a Circuit Simulation

A simulation model using transmission lines is needed to de-embed the probe. In

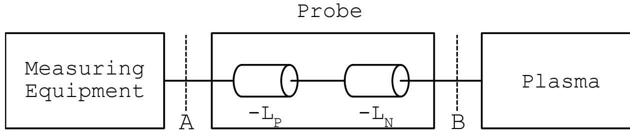

Figure 3.9: Schematic of the de-embedding process inside the circuit simulator to retrieve the base point impedance of the plasma. Reference planes A and B are indicated

Fig. 3.9 the circuit simulation of the probe is presented. A 50 Ω terminal feeds the signal into the model and is followed by the standard N-plug of length L_{P}, which consists partly of a dielectric to hold the inner conductor in place. This dielectric part is represented by a changing relative permittivity ε_{r}. For the inner and outer conductor, all geometrical values are entered therein. All coaxial lines are set to a negative length L_{N} to move the reference plane A of the plasma measurement from the output port to the end of the probe at position B.
If the plasma is enclosed[7], the base point impedance is a combination of the surrounding material and the plasma impedance. The probe consists of several coaxial line elements with different diameters, which are rebuilt in the circuit simulation. Another advantage of this method is the ability to use the de-embedding information for the ignition simulation of the device since the location for the ignition impedance is the same as for the plasma base point impedance.
The accuracy of the model is dependent mostly on the measurements of the physical dimension of the probe and the reproducibility of the large S-parameter measurement. Typical differences of 0.1 dB for the amplitude and a phase distinction of less than 1° are desirable, but not always possible to achieve. A higher precision causes increase in the development time. Therefore a trade-off decision has to be made, at which point the precision is met.

[7]By Quartz-glass or special ceramics

3.2.1.1 Exemplary Circuit Simulation for the Lumped Elements Model

On the example of the UV-Lamp, the circuit and the resulting matching is presented for the circuit simulation.

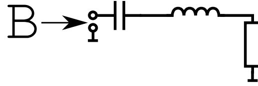

Figure 3.10: Lumped element simulation of the UV-Lamp's base point impedance including a capacitor for the quartz-glass representation.

Fig. 3.10 displays the substituting circuit of the UV-Lamp's de-embedded base point impedance at reference plane B. A capacitor with a value of 1.6 pF and a Q-value of 40 represents the glass surrounding the electrode. The plasma itself is a combination of an inductor with an inductance of 0.1 nH and a Q-value of 34. The circuit is terminated by a resistor having a value of 57 Ω.

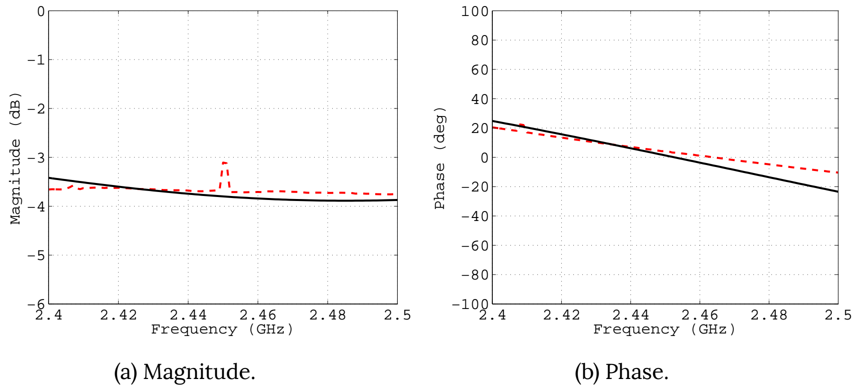

(a) Magnitude. (b) Phase.

Figure 3.11: Comparison of the de-embedded magnitude and phase of the measurement (dashed line) and the circuit simulation (solid line) made in ADS.

In Fig. 3.11 the comparison of the de-embedded measurement and circuit simulation is plotted. Fig. 3.11a displays the magnitude with an almost constant value of −3.5 dB from 2.4 GHz to 2.5 GHz. The phase is shown in Fig. 3.11b with a slow

decline. Both magnitude and phase exhibit an error margin of less than 3%. A resulting base point impedance of $(32.2 + 152.4i)\,\Omega$ is simulated for an input power of 200 W at 2.45 GHz.
In the next step, the de-embedding process is continued in the FEM simulator.

3.2.1.2 3D-Model in an FEM Simulation for the Fitting of the Plasma Base Point Impedance

After having obtained the base point impedance from the circuit simulation, a 3D model of the probe and the DUT is built. Primitives fitted to the measurements are used. Material properties are assigned to the corresponding bodies and missing materials such as non-standard ceramics or adhesives are entered into the database. The so-called fitting[8] the plasma in the FEM simulator consists of two steps:

- fitting of the physical properties,
- electrical property replication.

The probe itself is modeled by its physical properties. Main conductor losses are caused by surface roughness and inhomogeneous cover of the material effectively reducing the conductivity. To compensate for these higher losses, the conductivity of the conductor is reduced to match the measurements. In some cases, it is not possible to simulate all effects, causing the need to compromise on the precision. If this happens the closest match for the magnitude and the phase are set to fit the measurement.
If the DUT is shielded during its probing using a metallic knitted fabric, it is substituted by a surface that surrounds the device with a specific conductivity to simulate the losses and the meshes. This model is also used for the ignition part to simulate the electric field strength within the burner. The lossy dielectric technique models the electrical properties of the plasma. This technique describes the usage of material properties to match the electrical properties of the DUT, e.g. by setting a permittivity, which is smaller than 1. The theoretical background on these artificial dielectrics is explained in Ch. 2.3.5. Material constants such as permittivity and bulk conductivity are changed using a parameters sweep to match the measured data.

[8] Modeling the electrical properties of the plasma in the simulator

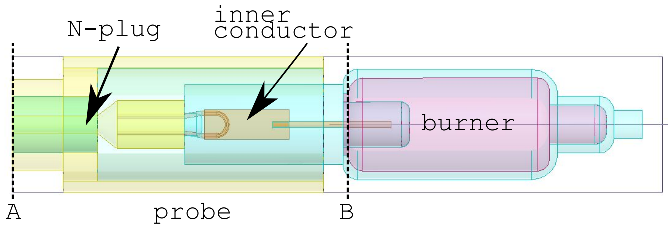

Figure 3.12: FEM simulation of the UV-Lamp's de-embedding process.

The simulation model of the UV-Lamp can be seen in Fig. 3.12. It includes a 3D-model of the lamp and the probe. A surface with proper boundary conditions represents the metallic knitted fabric surrounding the glass. Both reference planes are indicated using dashed lines and their corresponding label.

3.2.1.3 3D-Model Plasma Fitting Results for UV-Lamp

The FEM simulator requires a meta-material with artificial properties to calculate the electrical properties of the plasma. In this thesis the parameters conductivity and relative permittivity are fitted to the measurement.

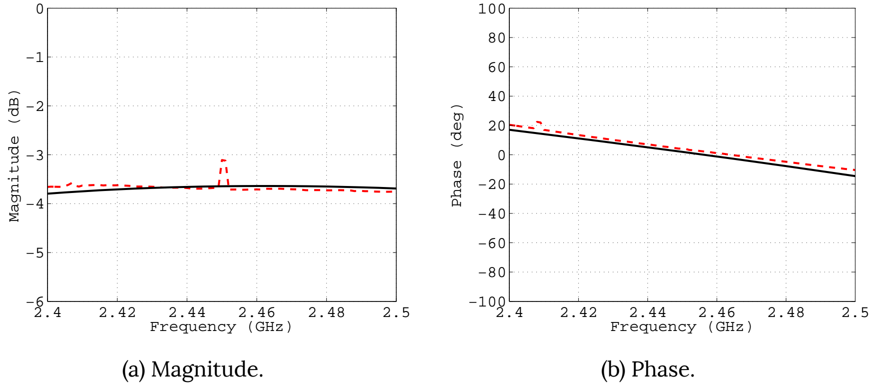

(a) Magnitude. (b) Phase.

Figure 3.13: Comparison of the de-embedded magnitude and phase of the 3D FEM simulation (dashed line) and the measurement (solid line).

The comparison of the magnitude (Fig. 3.13a) and the phase (Fig. 3.13b) shows a close match with an error of less than 1%. An FEM simulator is able to simulate the radiation effects in contrast to the circuit simulation. In the circuit simulator, it is only possible to calculate the values for the lumped elements, while the FEM simulator allows the calculation of additional effects such as surface roughness or radiation.

The data of the FEM simulation represented by the solid line display the de-embedded measurement data, while the FEM simulation (dashed line) shows the plasma fitting using a lossy dielectric material. For the plasma, material a conductivity of $37\,\mathrm{S\,m^{-1}}$ and a relative permittivty of 0.5 are calculated.

Based on these simulation results the development of the bi-static network is continued. In the next section, the development is presented based on the UV-Lamp introduced in this section and an additional electrode-less high-pressure lamp at 40 W.

3.3 Bi-Static Network Development of RF-Driven High-Pressure Plasma Lamps

The development of a bi-static network for two different lamp prototypes is explained in this section. These two prototypes with various requirements in size and power are introduced to highlight the application areas of microwave plasma lighting applications. The first lamp is built for an input power level of 200 W to decontaminate water. For the second model, a small spherical lamp at 40 W for high-pressure domestic lighting purposes is used. Additional information on electrode-less high-pressure lamps can be found in [94], [95] and [96]. More details on the usage of electrode-less UV-Lamps can be found in [97] and [98]. Both prototypes have been developed during this thesis.

3.3.1 Bi-Static Network Development of a High-Pressure UV-Lamp

For the decontamination of water in industrial environments, the presented UV-Lamps are built with an input power starting at 200 W.

(a) Prototype lamps with glass thicknesses of 3 and 8 mm around coaxial line.

(b) Annotated schematic of the first generation UV-Lamp.

Figure 3.14: First generation UV-Lamp and annotated schematic.

The new RF-driven UV-Lamp is a purpose-built prototype to compare the performance and influence of the electrode-less high-frequency operation to the DC excitation. In this configuration there were two iterations for the construction of the lamp:

- tungsten electrode melted into glass protruding into the burner (Fig. 3.14a)
- hollow cylinder topology with copper electrode. (Fig. 3.14b)

The lamp is filled with 20 mbar argon and 10 mg mercury, which is a standard filling for commercially available lamps. Both prototypes in Fig. 3.14a have their electrodes melted into and an additional layer of glass to avoid chemical interaction of the electrodes and the plasma. This electrode-less configuration requires the power to be coupled capacitively into the plasma. Total length is 30 mm, outer diameter 20 mm, inner diameter 4 mm, glass thickness 1.5 mm.

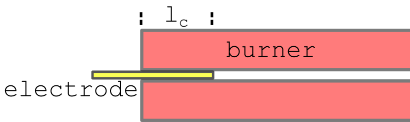

(a) Cross-section of the topology of the second lamp generation with de-coupled electrode.

(b) Second lamp generation prototype with inner electrode and plasma jet housing for cooling. Metallic knitted fabric is fixed by hose clip.

Figure 3.15: Cross-section and prototype of the second generation UV-Lamp.

In [99] a $\lambda/2$-dipole antenna has been selected to couple the power into an electrode-less UV-Lamp. The topology of the lamp is shown in 3.15a. This lamp exhibits a hollow cylinder structure with a length of 30 mm and an outer diameter of 20 mm. The inner tube has an inner diameter of 4 mm to allow the usage of a copper electrode within the lamp. The energy flows into the lamp via the coaxial line, which is surrounded by the burner at the length l_c, which is about $\lambda/6$ of 2.45 GHz.
During this thesis, the RF-network of the hollow-cylinder topology has been optimized. [99] required an input power level of 500 W and an air flow of 50 L min^{-1} to cool the electrode. The optimized network including a plasma jet housing with gas inlets is shown in Fig. 3.15b. A metallic knitted fabric prevents radiation of the RF-power. This prototype required an air flow of only 2 L min^{-1}.

3.3.1.1 Bi-Static Network Description for UV-Lamp

Based on the impedance transformer network shown in Fig. 3.8a, a bi-static network for the UV-Lamp is designed and realized

Figure 3.16: Bi-Static network prototype of the first generation UV-Lamp. Metallic knitted fabric provides shielding and prevents radiation.

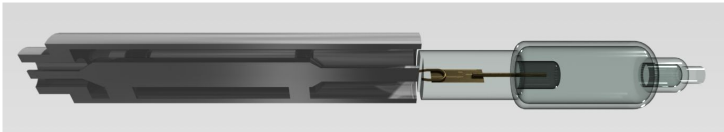

Figure 3.17: Cross-cut through the 3D-model of the bi-static network prototype of the first generation UV-Lamp.

In Fig. 3.16 the final bi-static network prototype of the first generation UV-Lamp is shown along with a cross-cut, which is generated from the FEM model in Fig. 3.17. It consists of a dual shunt inductor topology, which is surrounded by a brass tube. Two inner conductors of different lengths and diameters provide the impedance transformation for the different states.
Results for the ignition and operation state of the bi-static network are presented in the next two sections.

3.3.1.2 Ignition of the UV-Lamp by an Electric Field

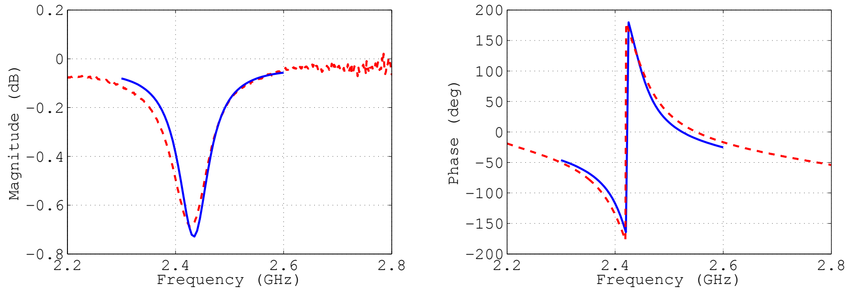

Figure 3.18: Fitting (solid line) and measured (dashed line) S-parameters for the UV-Lamp.

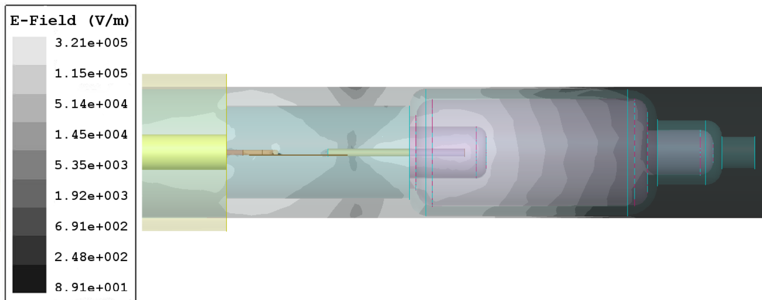

Figure 3.19: Simulated electric field distribution of the UV-Lamp's ignition state. A maximum amplitude of $3.2 \times 10^5\,\mathrm{V\,m^{-1}}$ at 40 W is calculated.

The resulting S-parameters both measured and simulated are plotted in Fig. 3.18. For the determination of the power level, the prototype is built and several repeatable ignitions are measured. This input power is set in the FEM simulator to calculate the resulting electric field strength.

In Fig. 3.19 the electrical field distribution using an input power of 40 W is shown, generating a maximum field strength of $3.2 \times 10^5\,\mathrm{V\,m^{-1}}$ inside the UV-Lamp's burner.

3.3.1.3 Mono-Static Operation Plasma State of the UV-Lamp

As described in Chapter 2.4.3 the maximum output power of the large signal measuring environment is limited. Therefore the plasma of the UV-Lamp could only be operated at 2.39 GHz using 200 W of input power.

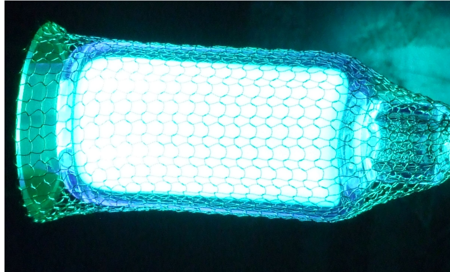

Figure 3.20: First generation UV-Lamp plasma with a low pressure at 200 W and 2.39 GHz. The electrode is located on the left side.

The resulting plasma of the lamp is shown in Fig. 3.20. Plasma exists in the entire burner and the brightest area is located in the area around the electrode. A metallic knitted fabric shields the lamp to avoid radiation.

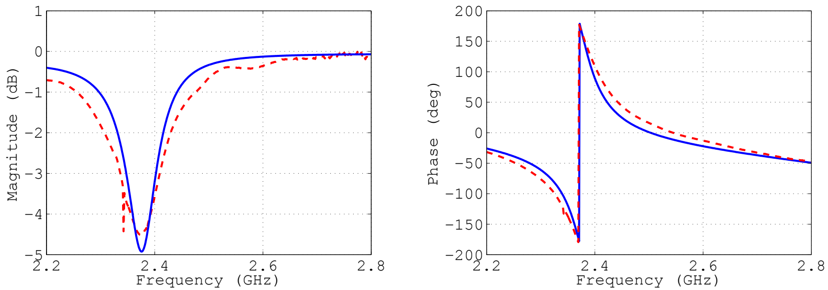

Figure 3.21: S_{11}-parameter fitting (solid line) and measurement (dashed line) of the UV-Lamp for an input power of 200 W.

No high-pressure is formed inside the burner. It is caused by the matching of 5 dB at 2.39 GHz, where only about 65% (~130 W) of the input power is coupled into the

plasma. The remaining power is reflected back into the amplifier and is absorbed by the circulator.
Both simulation and measured S-parameters are illustrated in Fig. 3.21. The ripple shown by the measurement data is caused by an inhomogeneous distribution of the plasma. Peak at around 2.38 GHz results from a cross talk of the large signal operating the plasma on the small signal of the network analyzer measuring the impedance. The comparison shows a maximum relative error of 5%.

3.3.2 Bi-Static Network Development for the Domestic High-Pressure Lamp (DHPL)

The second bi-static network designed in during this thesis is an electrode-less capacitively coupled high-pressure lamp. This lamp is a concept for the competition to existing lighting solutions and is developed in cooperation with the Lichttechnische Institut at the Karlsruhe Institute of Technology. These products are available for floodlight or industrial hall applications and make use of a resonant cavity. At the resonant frequency of the cavity, power is coupled to the lamp by a wave-guide mode. The resonator is part of a big heatsink shading the upper half space of the lamp. More details on this can be found in [37]. In this thesis, the lamp topology is

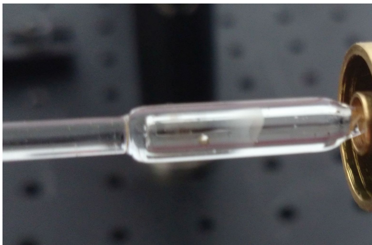

(a) Cylindrical prototype of the high-pressure lamp.

(b) Spherical prototype with a wall thickness of 1.5 mm.

(c) Configuration sweep of the spherical prototype with an increased wall thickness of 2 mm.

(d) Prototype with a diameter of 5 mm and whetted surface to improve energy flow.

Figure 3.22: Different geometries of the high-pressure lamp.

driven by a coaxial network. Only the aperture of the outer conductor shades the

emitted light. The lamp can also be reduced in size by using this type of construction. The lamp form is changed from a cylindrical to a spherical one to minimize heat losses as this geometric body has a lower surface-area-volume ratio. This research has also been published in [100].
In Fig. 3.22 the evolution of the lamp geometry starting is shown with a cylindrical form (3.22a), leading to spherical forms of different sizes and configurations (Fig. 3.22b and 3.22c). To optimize the energy flow from the electrode to the plasma, the glass is whetted, presented in Fig. 3.22d.
All lamps are filled with argon as start gas to ignite the plasma and a mixture of mercury to create the high-pressure for the efficient operation. Spectral gaps are filled with metal halides. A minimal temperature of 900 K is required for high-pressure operations.

3.3.3 Hardware Description of the DHPL Bi-Static Network

For the DHPL a bi-static prototype is built using the single shunt structure as shown in Fig. 3.8. This topology is chosen due to its smaller form-factor, compared to the dual shunt structure.

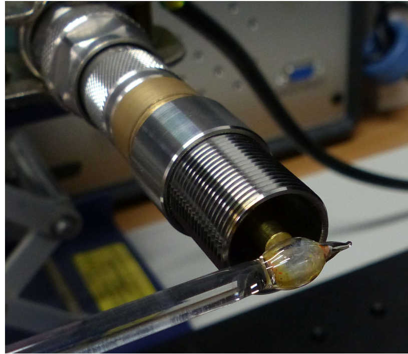

Figure 3.23: Bi-Static network prototype of the DHPL without radiation shielding.

In Fig. 3.23 the prototype of the bi-static network for the DHPL is shown along with a lamp. Metallic knitted fabric has been removed to improve the visibility of the picture. The prototype is built by use of the construction kit, which has also been developed in the course of this thesis. Inner conductor is made of brass, while the outer conductor consists of stainless steel. The shunt inductivity is realized by a copper disc, which is screwed between the back and front electrodes.

3.3.3.1 Mono-Static Ignition Plasma State of the DHPL

A matching of 10 dB at 2.43 GHz results in a maximum field strength of $1.5 \times 10^6\,\mathrm{V\,m^{-1}}$.

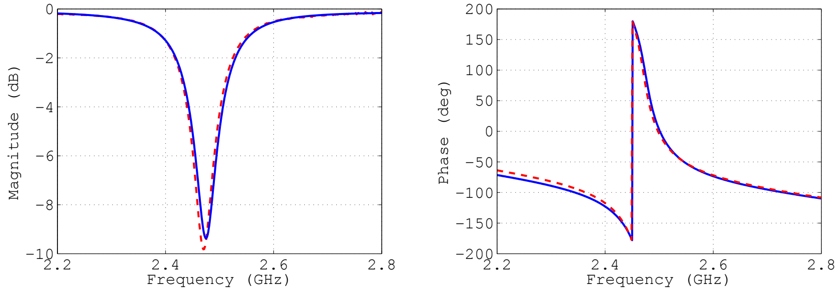

Figure 3.24: Measurement (dashed line) and the simulation (solid line) of the DHPL lamp ignition.

The resulting S-parameter plot is shown in Fig. 3.24 including the magnitude and the phase of the simulation (solid line) and the measurement (dashed line). Both lines show a maximum relative error of 2%.

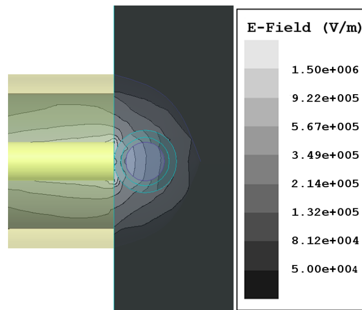

Figure 3.25: Electric field distribution of the DHPL at 20 W and 2.43 GHz. Maximum field strength of $1.5 \times 10^6\,\mathrm{V\,m^{-1}}$ is achieved, allowing re-ignition for a measured surface temperature of 750 K.

The resulting electric field distribution is plotted in Fig. 3.25 with a maximum value of $1.5 \times 10^6\,\mathrm{V\,m^{-1}}$ at 15 W input power.

Compared to the UV-Lamp the higher field strength is achieved due to the closer distance of the electrode to the burner. Also, the glass around the electrode inside the UV-Lamp is surrounded by 8 mm of quartz glass whereas the DHPL lamp is surrounded only by about 1 mm of material.

3.3.3.2 Mono-Static Operation Plasma State of the DHPL

The DHPL is shielded using a metallic knitted fabric reducing the emitted light by about 15%.

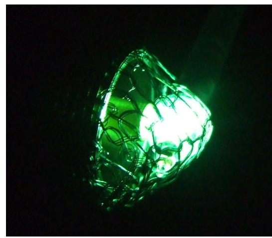

Figure 3.26: DHPL during operation at 40 W and 2.43 GHz. High-pressure is achieved. The greenish look of lamp indicates that not all of the salts have entered the gas stage. Based on HFSS, about 35 W are coupled into the plasma.

A wide band field strength indicator by Nardalert shows that no electric field strength higher than 4 mW mm^{-2} is emitted within a perimeter of 0.01 m around the lamp.
Goals for the first prototype of the DHPL are set to achieve high-pressure inside the lamp at an input power of 15 W. The lamp entered the high-pressure area at an input power of 30 W. Operation measurement results are recorded at 40 W of input power coupled into the network. Fig. 3.26 shows the resulting plasma.
In Fig. 3.27 the simulated and measured magnitude and phase of the simulation and the measurement are shown. A maximum matching of more than 40 dB occurs, which is more than 99.5% of the power transmitted into the network.
Not all of the power is coupled into the plasma. The measured losses are higher than the simulated ones caused by inhomogeneities of the material, surface roughness, and positioning of the lamp. Using the field calculator in HFSS determines an estimate effective power of 35 W coupled into the plasma. The remaining 5 W

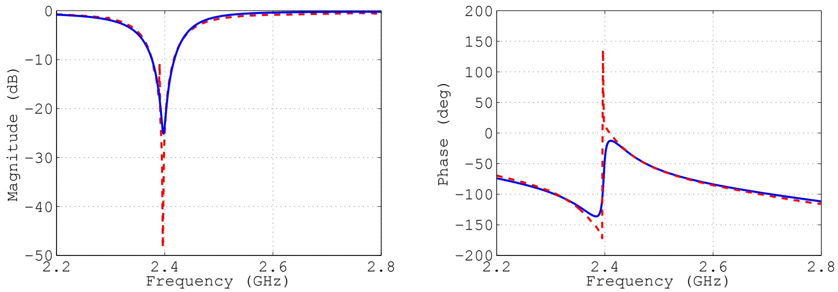

Figure 3.27: S_{11} magnitude and phase comparison of simulation (solid line) and measurement (dashed line) for operation.

have heated the network, glass and the metallic knitted fabric. The additional heating caused by the RF-power prevents cooling of the plasma by the network, which would lead to a decrease in the efficacy. The lamp's efficacy is mainly dependent on the temperature of the plasma.

No radiation is detected in a perimeter of 0.01 m around the lamp and is therefore negligible.

The calculation of the efficacy requires the amount of power coupled into plasma. This amount cannot be detected and therefore the gross power is used.

3.4 Optical and Thermal Measurement Results of the UV-Lamp and DHPL

In this section, the optimization of the optical output as well as the optical and thermal measurement results for both lamp topologies are presented. The development of a second large signal measuring environment is described. A new RFCore amplifier allowed powers of up to 400 W. In addition, the measurement results of the second generation hollow-cylinder topology UV-Lamp prototype as shown in Fig. 3.15b is presented.

3.4.1 Efficacy Optimization of the Microwave Plasma by Signal Modulation of the Electric Field

In contrast to DC and low-frequency excitations, RF-signals enable the modulation of several signal parameters.

3.4.1.1 Efficacy Optimization Methode Hardware Description

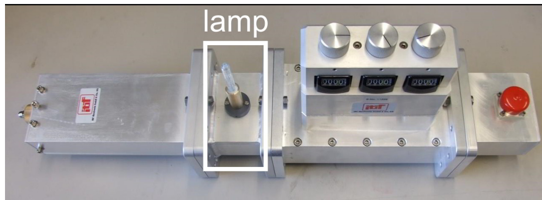

Figure 3.28: Low loss wave-guide tuning set-up containing shorting plunger, mounted shielded D8S lamp in fitting, 3-stub tuner and coax-wave-guide transition (left to right)

In [101] a method is described, which doubles the efficacy of commercially available automotive headlight lamps (approx. 190 $\mathrm{lm\,W^{-1}}$). It is stated, that superimposing an amplitude modulated signal leads to the increase in the lamp's efficacy. The torch was mounted onto a wave-guide, while power coupling was achieved with an optimized antenna-like structure.

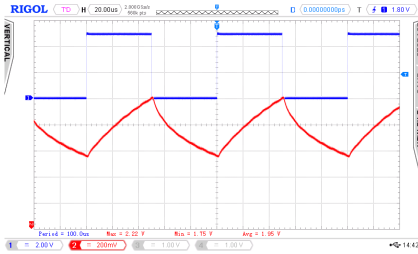

(a) Measured response of a signal: 2.45 GHz, squared modulation, modulation frequency: 10 kHz, 50% duty cycle.

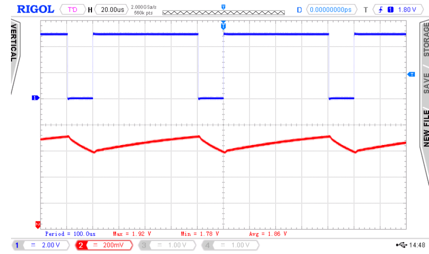

(b) Oscilloscope output: 2.45 GHz, modulation square, 10 kHz, 80% duty cycle.

Figure 3.29: Output response of the photo diode for different duty cycles.

In [36] the measurement set-up was rebuilt, which is illustrated in Fig. 3.28. Waveguides offer low transmission losses but due to their size, they are only used in applications, where available space is sufficient. Therefore a coaxial network is used to drive the same lamp to investigate the impact of the change in topology. Modifications on the coaxial network also allowed a direct comparison of the efficacy of the lamp driven by RF-signals and Switched-DC at 575 Hz.
A spectrometer measures the amounts of photons in a particular period, which is predefined by the luminance of the measured device and the distance to the spectrometer. Optimization goal of the chosen time interval is the improvement of the signal-to-noise-ratio. Upper and lower limit of the interval is the sensitivity and the noise floor of the spectrometer. A low-pass filter reduces the responsiveness of the device. Therefore changes above a certain frequency[1] can only be detected as the total amount of photons during that time.
An amplified photo diode (Thorlabs DA10A) with a bandwidth of 150 MHz is used to visualize the effects of the modulated signal on the illuminance. With this set-up changes of the radiant intensity up to a frequency of 75 MHz can be detected.
Fig. 3.29 displays the comparison of a square modulated signal at 2.45 GHz and different duty cycles. The illuminance changes with the generated signal, but with a longer rise and fall time of the slopes. It is caused by the inertia of the plasma.

[1] The used Ocean Optics JAZ is limited to 1 kHz.

3.4.1.2 Efficacy Optimization Measurement Results

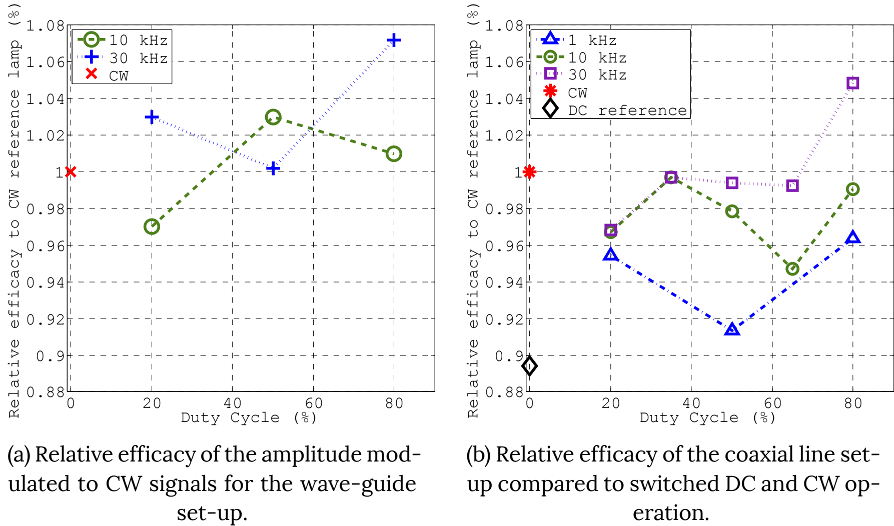

(a) Relative efficacy of the amplitude modulated to CW signals for the wave-guide set-up.

(b) Relative efficacy of the coaxial line set-up compared to switched DC and CW operation.

Figure 3.30: Efficacy changes of the wave-guide and the coaxial line set-up.

Relative efficacy of the wave-guide and coaxial network lamps are plotted in Fig. 3.30a and 3.30b. On the x-axis of both figures, the duty cycle is shown. It is plotted against the relative efficacy to the reference measurements on the y-axis. For both set-ups the continuous wave (CW) signal is referenced. Scale and range of the y-axis have been chosen to allow a side-by-side comparison of both measurements. For the wave-guide set-upm a maximum increase of 7% is calculated at 30 kHz at 80% duty cycle compared to the CW signal at the same input power. By superimposing the modulated signal a mean increase of 3% is measured.
The coaxial set-up shows a relative increase of 11% when driving the coaxial network with an RF-CW signal instead DC. Again the maximum increase of 5% is measured at 30 kHz at 80% duty cycle, but the modulation causes a decrease in the efficacy by a mean value of 3%.
As explained above, the spectrometer counts the amount of photons in a specified time interval. By superimposing a modulation on the RF-CW signal, the energy inside the plasma changes, while maintaining the same mean power level. As shown

in Fig. 3.30, the amount of photons is increased slightly due to the inertia of plasma, which results in a higher efficacy at the same mean power level.
Comparing the losses of both topologies, a relative mean decrease of about 5% is visible when switching from the wave-guide to the coaxial network set-up. These additional losses are caused by the metallic surface roughness and the mounting of the lamp inside the coaxial network. By optimizing the prototype, these losses can be reduced. This optimization shows the practical relevance of the coaxial network compared to the low losses of the wave-guide.
Superimposing a modulation on a CW-signal is also used in [102]. In the work the density of active plasma particles is increased compared to the CW as well as a lower gas temperature is shown. This observed phenomenon may explain the efficacy optimziation methode presented in this section.

3.4.2 Measurement Results of the High-Pressure UV-Lamp

This subsection presents the measurement results for the first and second generation UV-Lamp.

3.4.2.1 First Generation UV-Lamp with Melted-In Electrode

At the time of measurement of the first generation UV-Lamp the maximum available output was limited to 200 W. The lamp is built for an input power of about 400 W. Therefore no high-pressure is achieved at the lower power level.

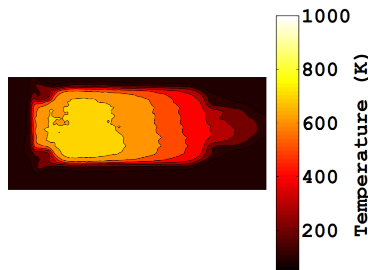

Figure 3.31: Temperature of the UV-Lamp for an input power of 200 at 2.45 GHz. A maximum temperature of 740 K is reached on the glass surface.

In Fig. 3.31 the glass surface temperature of the first prototype UV-Lamp at 200 W is presented. A maximum temperature of 740 K is measured. As shown in Fig. 3.20 the brightest area is located around the electrode, which is resembled by the area of the highest temperature.
Temperature decreases with the distance from the electrode. Temperatures of the lamp at 350 W using the new amplifier could not be recorded due to a technical problem of the infrared camera.

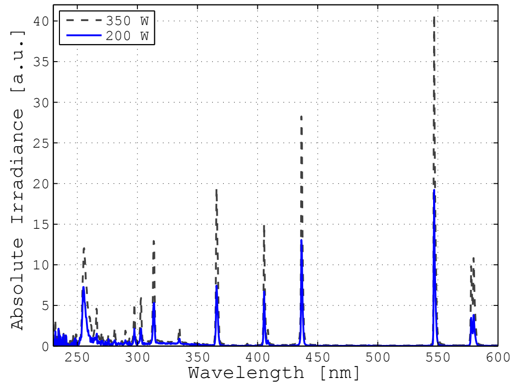

Figure 3.32: First generation UV-Lamp Spectrum at 200 W and 350 W. Single spectral lines only differ in their intensity. Line broadening at 250 nm is visible and is more pronounced at 350 W. Spectrum indicates not high-pressure.

Spectra of the first generation UV-Lamp at different power levels are plotted in Fig. 3.32, to illustrate the connection of the temperature/pressure and the optical properties. The sensor of the spectrometer is positioned in a distance of 0.5 m. To improve the optical output of the UV-Lamp a pressure of around 6 bar of the mercury inside the burner is desired.
Single spectral lines containing a high UV-part below 380 nm are visible. No continuum is present in the spectrum ([103]). At 200 W about 50% of the nominal operation power are coupled into the lamp. Therefore the energy level inside the burner is not sufficient for a high-pressure. The line broadening at 350 W is more pronounced but no high-pressure is indicated by the spectrum.
If high pressure inside the burner exists, the spectrum would show not only single spectral lines but a continuum ([104]). It is, for this reason, a redesign of the prototype is necessary.

3.4.2.2 Second Generation of the High-Pressure UV-Lamp with Jet Casing

In [99] an electrode-less UV-Lamp with a hollow cylinder topology is operated by a dipole antenna structure. It is described that the antenna impedance is not matched to the plasma impedance. Only the near field of the antenna powers the plasma.
The described prototype had to be cooled using an air flow of 50 L min^{-1} due to accumulated heat, hence reducing the temperature of the plasma. A redesign of

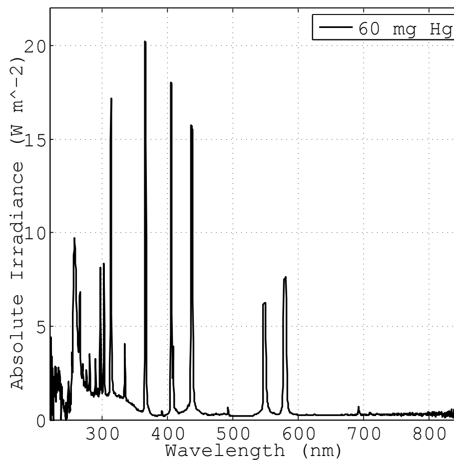

Figure 3.33: Spectrum of coaxial prototype using 350 W input power at 2.43 GHz.

the network was made to improve the antenna structure and reduce the cooling requirements. The new design is shown in Fig. 3.15. It utilizes the housing of a plasma jet in combination with a single shunt inductor for the bi-static network. A copper electrode matches the plasma base point impedance during operation. Cooling is provided by the gas inlets of the jet housing.
In Fig. 3.33 the spectrum of the coaxial prototype at 350 W (2.43 GHz) input power is shown. The measurement indicates a medium pressure spectrum with line broadening. A continuum in combination with a self-absorbing spectral line at 250 nm is pronounced. Another indicator is the molecule radiation of mercury from 230 to 250 nm.
An air flow of 5 L min^{-1} is applied to maintain a constant temperature of the electrode. This flow can be generated by any commercially available compressor.

About 50% of the emitted light is generated below 370 nm with about 30% for each UV proportion[9].
By comparing the results to the work presented in [99], a higher pressure inside the lamp is formed at a lower input power (500 W vs. 350 W). Operation using the dipole antenna shows only single spectral lines at 500 W. The cooling requirements are reduced by a factor of 10.

[9] UV-A, UV-B ,and UV-C

3.4.3 Measurement Results Presentation for the High-Pressured DHPL

In contrast to the second generation UV-Lamp, the DHPL has a hollow spherical configuration and the electrode is not enclosed by the burner.

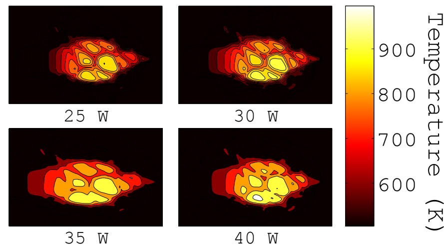

Figure 3.34: Measured thermal distribution of the DHPL at input powers from 25 to 40 W. Maximum glass surface temperature is 995 K. Wires of the metallic knitted fabric are visible by the drops in temperature.

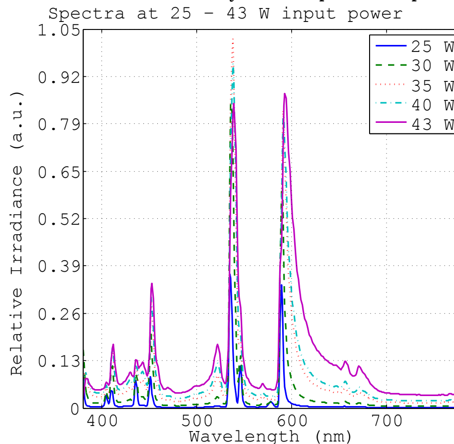

Figure 3.35: DHP lamp spectra at input power levels from 25 to 43 W. High pressure operation of the lamp at higher power levels is visible through an increased value and line broadening.

Mercury inside the burner creates pressures above 1 bar. A minimum temperature of 633 K has to be generated ([105]). The quartz glass of the lamp has a transformation point of 1403 K. If this temperature limit is surpassed the state of the glass

would change from rigid to vivid ([106]). To reduce the thermal stress on the glass, a back-off temperature of 200 K is suggested. Therefore the optimal temperature region for the operation of the lamp is between 633 K to 1203 K.
The surface temperature of the lamp is monitored at different power levels. The cold spot describes the point on the lamp surface with the lowest temperature. Since the plasma temperature is monitored indirectly by measuring the glass surface temperature, the temperature inside the burner is higher. If the cold spot temperature surpasses 630 K the vapor pressure of the mercury is higher than 1 bar.
In Fig. 3.34 the thermal properties of the lamp are illustrated for RF input powers from 25 W to 43 W. At 25 W the cold spot temperature of 581 K is measured, while at 35 W the cold spot temperature is 633 K. At 43 W a cold spot temperature of 681 K and a maximum temperature of 950 K is detected, which result in a vapor pressure range from 5 bar to 40 bar. For the UV-Lamp, these temperatures are reached at input power levels of more than 200 W.

Table 3.1: Measured and calculated properties of the DHPL at 2.39 GHz

Power W	**Appr. Luminous Flux** lm	**Efficacy** lm W^{-1}	**Cold Spot Temp.** K
25	752	30.1	581
30	3015	100.5	608
35	4252	121.5	633
40	5004	125.1	664
43	5551	129.1	681

The spectrometer is positioned at a distance of 0.2 m. Spectral values like luminous flux and efficacy are summarized in Tab. 5.2. Input power is calculated from the measured power corrected by the matching. Spectral data of the lamp is plotted in Fig. 3.35 from 25 to 43 W. Increasing the RF input power results in broadening of the existing spectral lines.
The efficacy optimization method described in Chapter 3.4.1 is applied to the lamp. A maximum increase of 5 % of the efficacy is measured at a modulation frequency of 1 kHz (duty cycle: 80 %, modulation depth[10] 80 %) resulting in a luminous efficacy calculations of 135 lm W^{-1} for the lamp.

[10] Amount on how much strong the modulation affects the signal

3.5 Discussion of the Results

In this chapter, the basics for the development of microwave plasma application around 2.45 GHz have been explained. Operation and ignition have been introduced as the main plasma states. An analysis of the required ignition field strength is presented, as well as custom-built prototypes for the probing of the plasma during operation. All these tasks were performed during this thesis.
An introduction to the workflow of a bi-static network development is shown in the example of an electrode-less UV-Lamp prototype, which is the first of its kind set-up. For the UV-Lamp, a second generation prototype is built, which produces a high-pressure spectrum using a coaxial RF-network. This second generation UV-Lamp is a good alternative to existing UV-Lamps since the life-time is prolonged due to its electrode-less configuration. This also enables the usage of new gas mixture that would otherwise react with the metal of the electrode. A disadvantage is the requirement of the metal knitted fabric that reduces the efficacy of the lamp by about 15%. Efficacy of this lamp can be further improved if the size of the lamp would be adjusted to the frequency.
An electrode-less high-pressure lamp (DHPL) at 40 W is also developed during the course of this work. A maximum efficacy of $135\,\mathrm{lm\,W^{-1}}$ is achieved using an input power of 43 W, which is above the efficacy of currently available LEDs. One advantage of this lamp is the possibility to use new gas mixture. In contrast to the LED, the spectrum exhibits a continuum and is, therefore, closer to the daylight spectrum. A disadvantage of this lamp is the high input power, which is higher than that of LEDs. Improvements are possible by reducing the size of the coaxial network and obtaining the metallic knitted fabric by a coating. This research has been published in [100].
Since the simulations of the ignition and operation for both lamps are very close to the corresponding measurements, the robust structure of the development workflow is shown in this section. To further demonstrate the importance of the plasma matching, the optical and thermal results of the lamps are presented along with an efficacy optimization technique using signal modulation.
This chapter has shown the implementation of microwave plasmas inside the ISM-band around 2.45 GHz for different power levels and prototype sizes.
In the next two chapters the influence of the frequency on the microwave plasma properties is analyzed. Possible optimizations for different applications are presented. The applicability of the presented workflow to develop custom-built

RF-network is presented in the next chapter for frequency ranges at 1.3 GHz and 3.5 GHz. After this, the comparison of thermal, optical and geometric for different microwave plasma applications will be presented in Chapter 5. The connections between the frequency and several plasma parameters is analyzed.

Chapter 4

Frequency Dependence of Microwave Plasma Electrical Properties

This chapter presents the extension of the existing equipment to frequency bands around 1.3 and 3.5 GHz with output powers up to 35 W. The extension is described in detail along with the hardware requirements for the balanced amplifier operation. It is assessed, if the principles and workflow presented in Chapter 3 can be applied to other frequencies. Similarities and differences are explained and analyzed. It is shown, that most of the presented microwave plasmas have a capacitive dominated base point impedance. Therefore the specific capacity of a plasma can be determined.

Based on the extensions three different application areas are covered: a plasma jet, an electrode-less phosphor-coated lamp (PC-Lamp) and a hollow glass cylinder filled with xenon (XHC). Measurement and simulation results of the frequency dependence are plotted for each application. Different plasma models and their fitting for each application are presented with a focus on the reproduction of the physical dimensions of the plasma body. It is analyzed whether the existing RF

plasma model can be refined to better represent the electric field distribution inside the plasma. The results show, that simple lumped element and 3D-models are capable of fitting the plasma in the simulator.
For the first time, an analysis of the transmission values of a microwave plasma is presented. Two new models are created to fit the plasma in the simulator: A lumped element model using a single frequency-dependent capacitor calculates the plasma transmission properties. In the FEM simulator, a 3D core/cone model fits the plasma close to the measurements.

4.1 Lumped Element and 3D-Model for the Fitting of Reflection and Transmission Properties of a Microwave Plasma

In this section, the reflection and transmission of different microwave plasma applications are measured and analyzed.
Base point impedance of the PC-lamp and the XHC-device exhibit a capacitive impedance (negative imaginary part). Both are substituted by a series resonant circuit of inductance and capacitance. Below its resonant frequency, a series resonant circuit acts as a frequency-dependent capacitive component ([68]). The inductivity is only needed to shift the resonance frequency and simulate the frequency dependence.
The capacitive behavior is also measured for the transmission network. In the circuit simulator, a series capacitor with a variable quality factor (q-factor, q-value[1]) is sufficient to substitute the plasma. The q-value of each component is dependent on the frequency, too. It is set to the following frequencies for each of the bands: 1.3 GHz, 2.4 GHz and 3.5 GHz.
In Fig. 4.1 the equivalent circuit diagram of the plasma is plotted. It is based on the model of [74], which treats the plasma as a rodded material. In this chapter, the plasma consists of a parallel circuit of a capacitor and a resistor at all frequencies. It is shown in the upper part between the two lines. The inductor is required to substitute the frequency-dependent part of the capacity. In the lower left corner, an axial section of the plasma shows an exemplary distribution of the capacitor and the resistor.

[1] Ratio of inductive or capacitive reactance and resistance

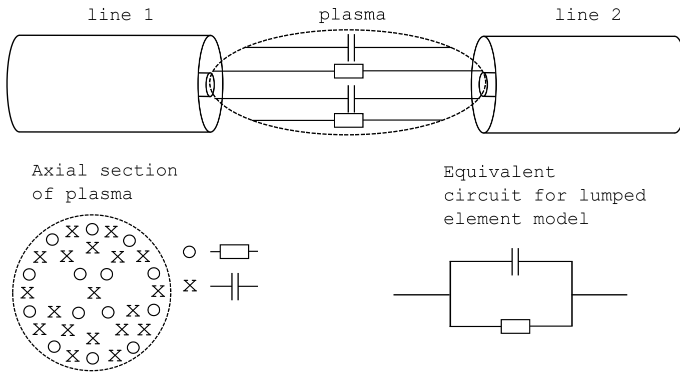

Figure 4.1: Transmission line set-up with plasma impedance representation for the reflection and transmission value.

All mentioned plasmas in this section exhibit a specific capacity C_{Spec}, which is defined as the capacity per volume. It can be compared to the specific conductivity ([107]). In this chapter it is shown that all investigated microwave plasmas have a specific capacity that is dependent on the frequency and the input power. Therefore it is directly influenced by the amount of free charge carriers and their collision frequency. The integral of all specific capacities is calculated in the circuit simulator as the resulting capacitive impedance of the plasma.

4.2 Extension of the Large Signal S-Parameter Measuring Environment

As described in Sec. 2.4.3 the large signal S-parameter measuring set-up monitors the electrical properties of the active plasma. Frequencies from 2.3 GHz to 2.6 GHz were possible prior to the extensions described in this section. The Rohde & Schwarz ZVM network analyzer supports the measurement of frequencies up to 20 GHz. Two additional frequency bands around 1.3 and 3.5 GHz are chosen due to cover an area of more than 2 GHz, including an equidistant spacing of 1.1 GHz for the center frequencies. Thus an additional degree of freedom for the design of applications is offered.

4.2.1 Common Hardware Components and Measuring Equipment of the Extension

New couplers and amplifiers prototypes are built during this thesis to generate the required signals and to extend the frequency range to the 1.3 GHz and 3.5 GHz bands. Balanced amplifier set-ups are implemented to increase the available linear output power. In this set-up, the differential signal of two amplifiers is combined using a hybrid coupler for a gain of 3 dB.

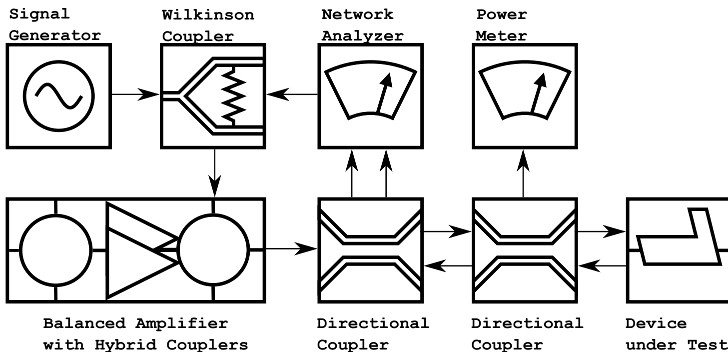

Figure 4.2: Block diagram of the large signal S-parameter environment extension for the additional bands.

In Fig. 4.2 the block diagram of the modifications is shown. The signal of the network analyzer and the signal generator are combined using the Wilkinson coupler. The balanced amplifier stage creates the necessary output power and is described in the next section. The details of the assemblies are described in the following list:

Wilkinson Coupler A combiner is required to superimpose the signal of the network analyzer and the large signal to drive the DUT. More information on the Wilkinson coupler can be found in [108].

Bi-Directional Coupler A bi-directional coupler enables the measurements of the inserted and reflected waves. It generates both wave quantities, which are directed to the network analyzer. The coupler used has a frequency range from 1 GHz to 4 GHz and limits the frequency of the large signal measuring environment.

Power Meter The power meter is calibrated and its correction factor is set to the specific frequencies and signal types. For this calibration of the power meter, the output power of a known source is measured. The offset of the meter is changed to the required amount. To ensure a constant input power inside the plasma, the input signal is corrected by the measured matching.

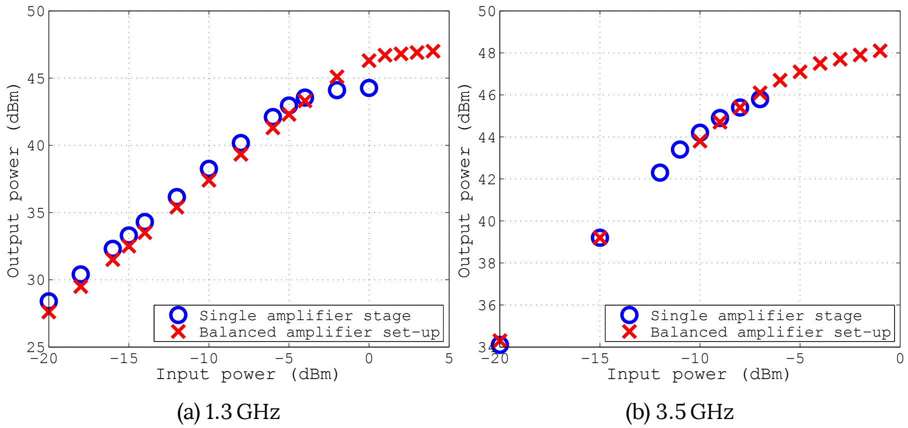

(a) 1.3 GHz

(b) 3.5 GHz

Figure 4.3: Input power vs output power of the amplifier stages for the extension of the large signal measuring environment at the indicated frequencies.

4.2.2 Balanced Amplifier Stages of the Large Signal Measuring Test-Set-Up

A balanced amplifier stage is chosen for the frequency bands around 1.3 GHz and 3.5 GHz, since this configuration performs with a good matching and a good stability. This is required since large signal S-parameter measurements rely on a stable and linear signal. The output signal of an amplifier gets distorted and non-linear signals if the maximum input power is surpassed. Therefore a linear back-off of −3 dB is often used to satisfy the linearity requirements. To compensate for these losses a balanced amplifier stage extends the ideal linear range by 3 dB. It splits the unbalanced mixed input signal and puts out two signals at ±90°. After the amplifier stage, the balanced signal is combined with an unbalanced signal by using the reversed connections. The fourth port is terminated with a 50 Ω attenuator for a cleaner signal. Additional information can be found in [109].
Maximum output power is determined for the new amplifier stages, like the current amplifier around 2.45 GHz. As described earlier, the amplifier is built in a balanced set-up to linearize the power output. A pair of cables with a phase difference of less than 2° connect the amplifier stages. More details on linearization techniques can be found in [110].

4.2.2.1 Balanced Amplifier Hardware for the 1.3 GHz Band

The amplifier stage at the lowest frequencies consists of two Mitsubishi RA18H1213G with a maximum output power of 35 W (45.4 dBm). Maximum input power is 23 dBm. A custom PCB and a heat sink are designed and built for the experiments.
The maximum linear output power of the signal is limited to 12 dBm. Therefore a pre-amplifier is required to raise up the signal amplitude to 23 dBm. A TriQuint TQP8M9013 pre-amplifier is placed before the first hybrid coupler. A demo board is modified for the desired frequency range from 1.25 GHz to 1.3 GHz. It delivers the necessary maximum output power of 30 dBm to compensate for the −6 dB input loss of the passive RF networks.
Both Mitsubishi amplifiers are driven with a gate voltage of 13.8 V. A 5 V voltage regulator in combination with a 500 kΩ potentiometer changes the operating point of the amplifier. Getting the most linear operating point is achieved by setting the bias voltage to 5 V, which places the amplifier into class A operation mode. At this point, a single amplifier draws a quiescent current of 8 A.
Fig. 4.3a shows the gain for a single amplifier and the amplifier stage at 1.28 GHz including the pre-amplifier for input powers from −20 dBm to 5 dBm. A maximum power of 48.5 dBm (70 W) is measured for the complete set-up including both hybrid couplers and the Wilkinson coupler. The current increases to 17 A for both amplifiers. Linear gain is possible up to 40 W. Additional losses of cables and connectors can be neglected. The value of the linear gain is 28 dB. The maximum linear output power fluctuates between 0.5 dB from 1.2 to 1.3 GHz. At 43.5 dBm and 46.5 dBm the 1 dB compression point is located for the 1.3 GHz amplifier stage.

4.2.2.2 Balanced Amplifier Hardware for the 3.5 GHz Band

Two balanced WiMax base station amplifiers in class A operation mode deliver the linear power for the band from 3.4 to 3.75 GHz. A linear gain of up to 47 dBm (50 W) is measured using a quiescent current of 6 A for a single amplifier.
To get the maximum output power, an input power of 10 dBm is needed for the balanced set-up. Therefore no pre-amplification stage is required. An increase of 3 dB is measured by moving from the single to the balanced set-up.

In Fig. 4.3b the gain of a single amplifier is plotted along with the gain of the balanced set-up. A maximum combined output power of 48.1 dBm (64 W) is measured. The maximum linear output power fluctuates between 0.3 dB from 3.4 to 3.75 GHz. The measurement of the combined arrangement shows a power of 47 dBm (50 W). By backing off the power, the linear area of the amplifiers is determined at a maximum of 45.5 dBm (35 W).

4.2.3 Summary of Extensions of the Large Signal Measuring Environment

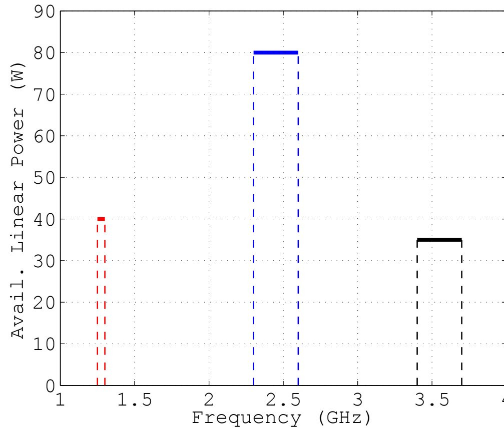

Figure 4.4: Graphical overview of the maximum linear output power available from 1.3 GHz to 3.5 GHz.

For an overview of the maximum linear output power available over all frequencies, it is plotted in Fig. 4.4. To compare the frequency-dependent effects, a constant electric field strength is required. Therefore the maximum power level for all frequency bands is limited by the 3.5 GHz amplifiers to 35 W.
Power levels are set from 5 W to 25 W due to limitations of the hardware used and the plasma properties.

4.2.4 Large Signal S-Parameter Measuring Environment Extension for Plasma Transmission Properties

Microwave transmission measurements require an extension of the large signal S-parameter measuring environment, too. Before this, only the determination of the reflection base point impedance[2] was required. An additional port on the network analyzer enables the measurement of the transmission. Reduction of the large signal power to a non-destructive level is provided by an additional attenuator inserted into the signal chain after the transmission prototype.

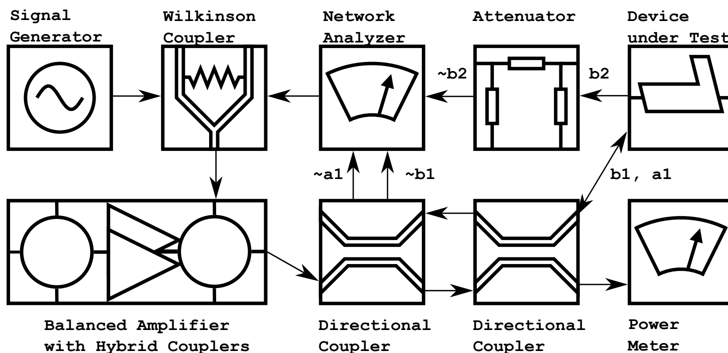

Figure 4.5: Block-diagram for the transmission measurement test-set based on the large signal S-parameter environment at different frequencies.

The block diagram of the transmission extension is plotted in Fig. 4.5 including the signal flow. On the right side, the additional signal from the DUT over the attenuator to the network analyzer marks the extension for the measurements. All other components are the same as for all other measurements in this chapter.

4.2.5 Frequency Dependency Measuring Error

The estimation of the impedance measuring accuracy depends mainly on the calibration of the network analyzer. The OSM [3] calibration method eliminates all influences of the amplifier chain on the measurement and sets the reference plane to

[2] calculated from S_{11}
[3] Open, Short, and Match (Load)

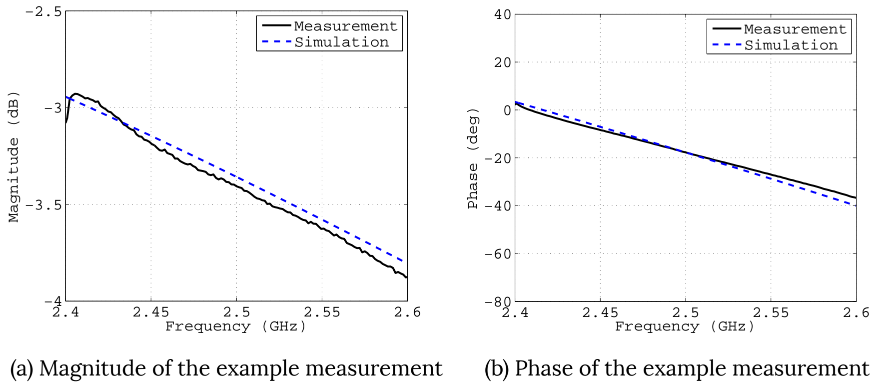

(a) Magnitude of the example measurement (b) Phase of the example measurement

Figure 4.6: Large signal S_{11} measurement and simulation comparison for the PC-lamp (2.5 GHz and 5 W with a resulting relative error of 3.7%).

the desired position at the N-plug of the DUT. More details on calibration standards can be found in [68].
A ripple test is made with a test cable[4], which was shorted at its end to verify the calibration. A peak to peak ripple of 0.5 dB is measured resulting in a source match of −28 dB. It corresponds to a phase measuring error of 2.28° and a magnitude error of 0.34 dB for high reflecting DUTs. These values are the relative measuring errors for all the measurements presented in this chapter. More information on the classical ripple test can be found in [111] and [112].
All measurements of the jet, the PC-Lamp, and XHC are based on the modifications of the measuring environment described in the previous section. Additional transmission measurements are presented using a modified version of the jet.
Measurements of the PC-lamp and the XHC are simulated to investigate possible connections between the frequency and the lumped element properties. Only the mean relative error between simulation and the measurement is given. In Fig. 4.6 an example plot for the PC-lamp at 2.5 GHz and 5 W is plotted with a relative error of 3.7%. This plot has been chosen, since it is located in the mean region of all simulated errors.
For the measurements of the transmission, the extended measuring environment is calibrated by the two-port one-path forward method. It requires the full open,

[4]Precision PC7 air line

short and load calibration for the first port. The transmission is calibrated by connecting a calibration standard between the two ports. A full transmission measurement was not possible due to the lack of a second coupler for the determination of S_{22}. The ripple test shows a source match of 32 dB. It corresponds to an error of 0.22 dB and 1.43°. More information on the calibration method can be found in [113]. After the calibration, the reference planes are located on the N-plugs of the prototype.

4.3 Frequency Dependence of an Atmospheric Pressure Microwave Plasma Argon Jet

Atmospheric pressure plasma jets have been in use for several application areas such as material manipulation, medical and chemical purposes ([19], [22], [17]). For plasma generation signals range from pulsed DC up to several GHz at input powers from mW to MW ([8], [9]). For more details and application areas using this specific jet design see [114] and [115]. This section will determine the frequency-dependent effects on the electric properties of a microwave plasma at atmospheric pressure levels up to 1 bar. Argon dieacts as the process gas at a constant gas flow of 1.6 L min^{-1}.

4.3.1 Plasma Modeling for the Jet using Lumped Elements and Lossy Dielectrics

In its most primitive form, a plasma jet consists of a coaxial topology, which is flooded with the process gas. The gas exits the jet through an opening at one of the ends. On the other side, the plug for inserting the microwave power is located. Power is applied to an electrode which ignites and operates the plasma. Therefore

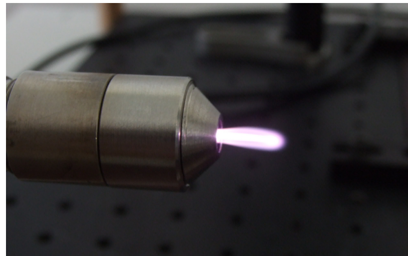

Figure 4.7: Plasma jet with an argon plasma driven with 20 W at 2.43 GHz and a matching of −5 dB

the plasma is visible outside the housing and can be used for the application. If desired different size of the plasma can only be achieved by adjusting the gas flow or the applied power. The surface activation is an application that requires a larger size to optimize the throughput, while medical applications may need a smaller size

for a higher precision. Due to the generated heat or medical reasons often compromises are required for the gas flow or power to not surpass specific limits. An investigation on the changes in size caused by different frequencies is presented in Chapter 5.2.1. In Fig. 4.7 a jet, which is operated with argon at an input power level of 20 W. The results of this section have also been published in [116].

4.3.1.1 Modeling in Circuit and FEM Simulation of the Jet

A model for the representation of the jet inside the circuit and FEM simulators is built in this thesis.

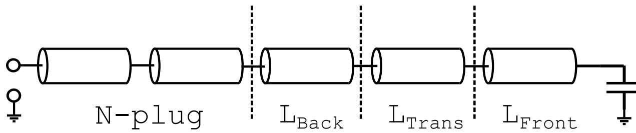

Figure 4.8: Circuit simulation model of the jet represented by coaxial lines. Corresponding positions in the FEM simulation model are annotated.

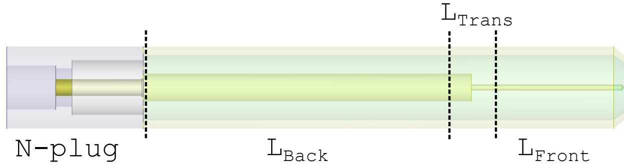

Figure 4.9: Annotated FEM simulation model of the jet. The indicated positions are for visualization purposes of the circuit simulation model.

Broadband measurements of the jet in a cold state[5] from 0.5 GHz to 4 GHz are conducted and fitted. In addition, the jet is shorted with a metal plate for easier deembedding.

In Fig. 4.8 and 4.9 the simulation models from the circuit and FEM simulation of the jet are displayed. The circuit model consists of a series connection of five coaxial lines, which correspond to the different areas of the jet. These areas are also indicated in the FEM simulation model.

A capacitor fits the termination of the jet in the cold state to enable the simulation of the resulting ignition voltage at the tip of the electrode. The voltage in the FEM simulator is calculated by integrating the electric field strength along a line from

[5]No plasma is present

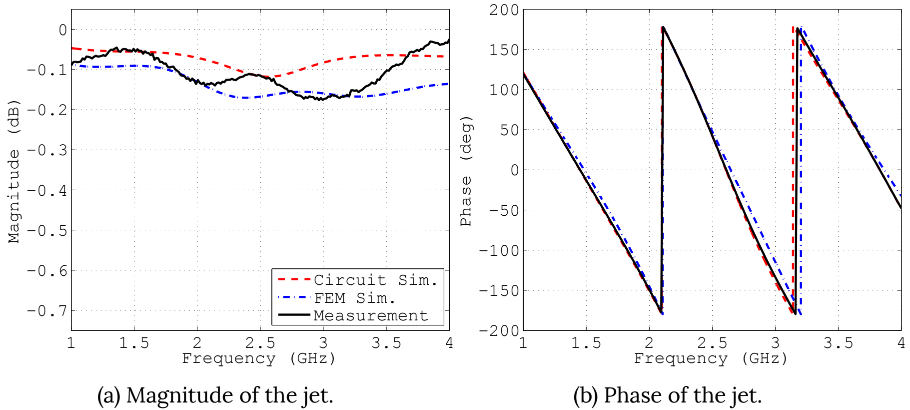

(a) Magnitude of the jet.

(b) Phase of the jet.

Figure 4.10: Comparison of the S_{11}-parameter of the measurement, circuit simulation and FEM simulation model.

the tip of the electrode to the nearest position of the jet casing[6]. Fig. 4.10a and 4.10b illustrate the broadband magnitude and phase matching of the circuit simulation and FEM simulation to the measured values for the cold state from 1 GHz to 4 GHz. As mentioned above, not all frequency-dependent losses can be simulated, and therefore the slope of the magnitude is matched as closely as possible to the measurement.

Radiation effects can only be reproduced inside the FEM simulator. The phase exhibits a relative error of less than 2% over the whole frequency band from 1 to 4 GHz. This error is below the measuring error of the ripple test. The circuit simulation model calculates the base point impedance of the plasma.

[6]A field calculator provides the necessary equations.

4.3.1.2 Jet Plasma Body Representation in FEM Simulation

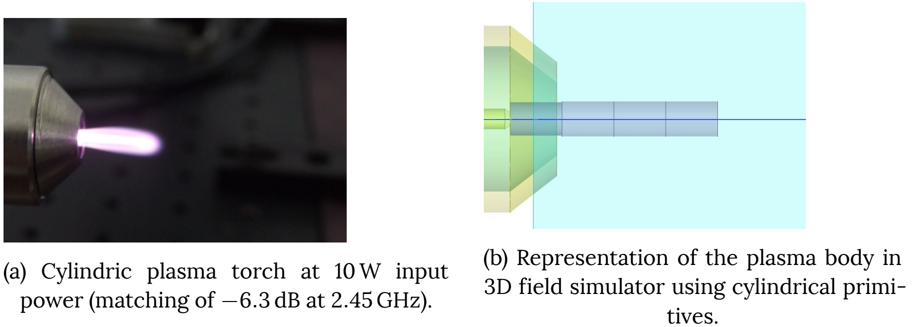

(a) Cylindric plasma torch at 10 W input power (matching of −6.3 dB at 2.45 GHz).

(b) Representation of the plasma body in 3D field simulator using cylindrical primitives.

Figure 4.11: Comparison of the plasma and its representation in an FEM simulator

For the operation of a jet, a gas flow needs to be applied to generate the plasma torch in front of the casing. Otherwise, a spherical plasma ball is formed on the tip of the electrode. This spherical plasma finds its usage in the microwave plasma spark plug ([83]). A cylindrical body is formed by applying the gas flow. It is presented in Fig. 4.11a for an input power of 20 W at 2.45 GHz. A higher flow of the gas leads to an extension of the cylinder at the same power level. The correspondent FEM representation is illustrated in Fig. 4.11b. Since the losses show a maximum of −0.15 dB, they do not have a significant effect on the conductivity estimation of the plasma. For the height and length of the cylindrical bodies the determined plasma body sizes presented in Chapter 5.2.1 are used.
The simulation modeling of the plasma follows two different paths. As described in Chapter 2.3.5 lumped elements (resistors, capacitors, and inductors) substitute

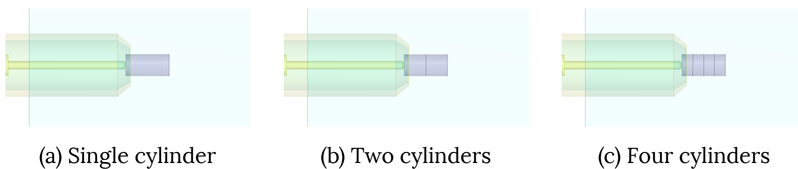

(a) Single cylinder (b) Two cylinders (c) Four cylinders

Figure 4.12: Different models of the jet for the simulation of the plasma at 1.3 GHz and 5 W input power as an example for the FEM simulation.

electrical plasma properties in the circuit simulator. In the FEM simulator, the conductivity and the permittivity of a meta-material substitute the plasma as an electrical conductor. By moving further away from the electrode tip, the energy of the electric field inside the plasma is reduced. It results in a smaller generation of free charge carriers and a reduced conductivity. Different cylindrical bodies with a fixed or decreasing conductivity imitate this behavior in the FEM simulator. A model case is presented for a fitting of a plasma at 1.3 GHz.
Fig. 4.12 illustrates the cylinder topologies for one, two and four cylinders. All models with two or more plasma bodies are tapered[7]. The measurement of a 1.3 GHz plasma at 10 W is set as reference. Results of the matched magnitude and phase are

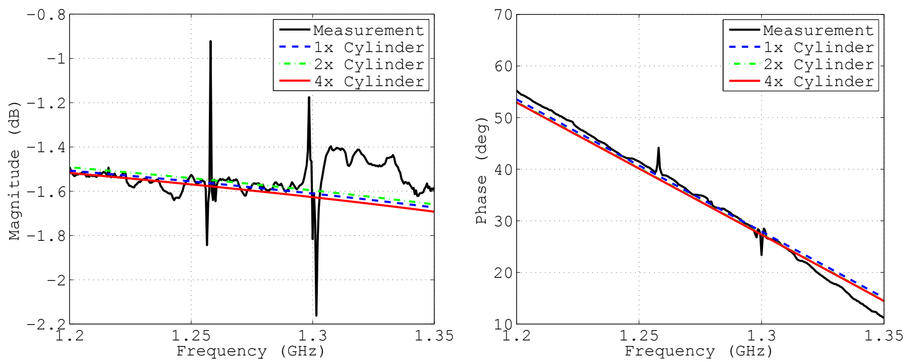

(a) Magnitude of a jet driven by 10 W power at 1.3 GHz and three different cylinder topologies.

(b) Fitted phase of the measurement and the three different FEM models.

Figure 4.13: Magnitude and phase of the measurement with additional data.

plotted in Fig. 4.13. All three models show a good agreement for the phase within the measuring error margin. For the magnitude, all models are off by 0.2 dB above 1.3 GHz.
All three models exhibit the same slope progression. Even by changing the values of the secondary and higher cylinder materials only the axial distance is increased but not the slope. The single cylinder models exhibit the same behavior as the two other models. It will be used for further simulations. Simulation runs are reduced by a factor of up to four by reducing the number of cylinders from four to one.

[7]Values of the conductivity decreases with distance to the electrode

The FEM model is an approximation for the conductivity to fit the simulation to the measurement, as only reflection measurements are analyzed. For the example in Fig. 4.13a a single cylinder with a conductivity of $12\,\mathrm{S\,m^{-1}}$ is calculated. Other electrical properties such as permittivity, permeability, and loss tangent would require a fixed wave impedance and a transmission measurement. A fixed wave impedance can only be set if the plasma is shielded to avoid radiation.
The impact of the relative permittivity has been investigated, too. Changes to this properties result in minor effects on the phase of the simulation. For example, a doubling of the permittivity from 0.5 to 1.0 alter the phase by 0.5°. Therefore the conductivity[8] is simulated.
As mentioned above, the plasma is not shielded and radiates parts of the microwave energy. These effects need to be considered in the simulation. De-embedded measurement results are calculated in the circuit simulator. The radiation effects can only be fitted by the FEM simulation. The results presented are taken from the FEM simulation runs.

[8] For all measured power levels and frequencies

4.3.1.3 Measurement Results of the Jet over Frequency

All frequencies and power levels of the jet are measured from 5 W to 15 W. The complex base point impedance[9] of the argon plasma is determined in the circuit simulator using the broadband model of the jet presented in the previous section.

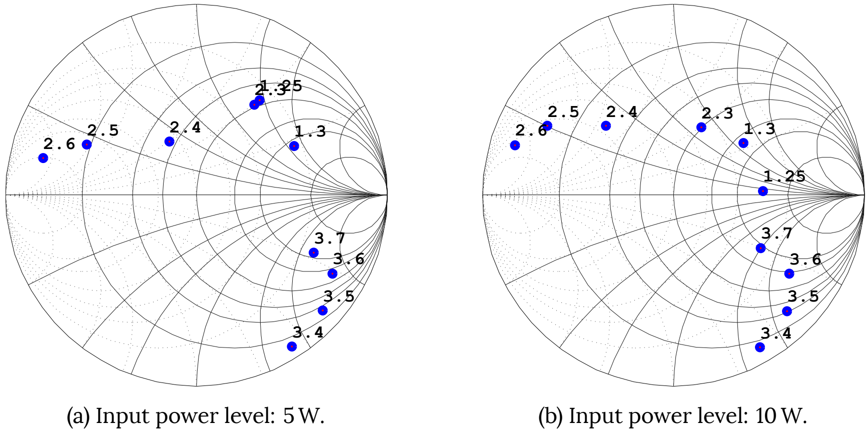

(a) Input power level: 5 W.

(b) Input power level: 10 W.

Figure 4.14: Complex reflection values of a de-embedded jet for different frequency ranges.

In Fig. 4.14a the results for a constant input power of 5 W are plotted, whereas Fig. 4.14b shows the complex reflection values for 10 W. Plots for 15 W are omitted since the changes compared to the lower power levels are not changing significantly.
A strong dependence of the magnitude on the frequency is striking from 1.25 GHz to 1.3 GHz. For the ranges around 2.4 and 3.5 GHz the change of magnitude and phase is smaller. Only minor changes occur within the same frequency band by increasing the power levels. This behavior is measured for all energy levels, too. By using a power- and a frequency-dependent equivalent circuit diagram, the behavior of the plasma could be determined based on the measurement results. A non-monotonic connection across all frequencies is apparent.

[9]Results are presented in Smith Chart as S_{11} reflection values. See Eq. (2.46)

Table 4.1: Fitted RF conductivities using the plasma body model at power levels from 5 W to 15 W and frequencies from 1.3 GHz to 3.5 GHz.

Frequency GHz	**Input Power** W	**RF Conductivity** $S\,m^{-1}$
1.3	5	0.45
	10	0.6
	15	0.7
2.4	5	11
	10	12
	15	13
3.5	5	9.5
	10	10
	15	11.5

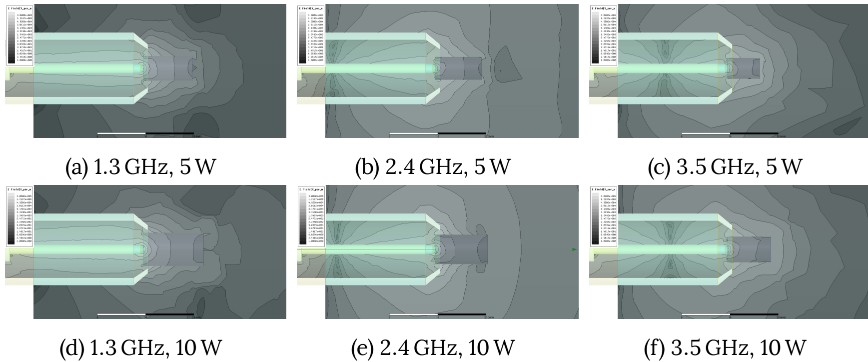

(a) 1.3 GHz, 5 W (b) 2.4 GHz, 5 W (c) 3.5 GHz, 5 W

(d) 1.3 GHz, 10 W (e) 2.4 GHz, 10 W (f) 3.5 GHz, 10 W

Figure 4.15: FEM simulation of the electric field distribution of the plasma jet using a single plasma body and the conductivities presented in Tab. 4.1.

All fitted results of the frequencies and power levels show an error margin of 5% relative to the corresponding measurement. For further investigations measurements with frequency points space more closely would be required to obtain possible connections of the base point impedance and the frequency.
These results confirm that the workflow for the development of a special built RF network can be applied to the other frequencies. All measured impedances can be

substituted by lumped elements and only the changed wavelength has to be taken into account.
In Tab. 4.1 the plasma conductivities fitted in the FEM simulator for 1.3, 2.4 and 3.5 GHz are presented. At 1.3 GHz the lowest fitted conductivities range from $0.45\,\mathrm{S\,m^{-1}}$ to $0.7\,\mathrm{S\,m^{-1}}$, while the frequency bands around 2.4 and 3.5 GHz are within the same region.
Inside the frequency bands[10] all measured values exhibit a 10% margin. For the same frequency, the conductivity increases with the input power and therefore the energy level within the plasma. At higher energy levels more free charge carrier are generated causing a raise of the conductivity.
The distribution of the electric field inside the plasma is shown in Fig. 4.15 for an input power of 5 and 10 W at frequencies from 1.3, 2.4 and 3.5 GHz. Phase of the electrical field is set to 0°, while only the source power is changed.
The plasma in this simulation is represented by a single cylinder of constant conductivity. Dimensions of the cylinder are scaled to measured geometries, presented in Chapter 5.2. Lighter areas in the plots represent higher values of the electric field strength.
As expected the distribution of the electric field is caused by changes in the wavelength. This has been explained in more detailed in Chapter 2.4. As it focuses on the impedance fitting only, the electric field distribution inside the plasma shows the limitation of this model. It has been analyzed that the model is able to fit the plasma conductivity over the whole investigated frequency range from 1.3 GHz to 3.5 GHz.
The fitting results show that the development workflow can be applied in the FEM simulator using a single cylinder of a fixed conductivity.

[10] 1.25 GHz to 1.3 GHz, 2.3 GHz to 2.6 GHz and 3.4 GHz to 3.7 GHz

4.4 Frequency Dependence of Low-Pressure Microwave Plasma Sources

For the comparison of low-pressure microwave plasmas and lighting applications, a standard low-pressure but electrode-less phosphor-coated lamp (PC-lamp) and a hollow cylinder filled with xenon (Xenon Hollow Cylinder, XHC) are measured. These DUTs are chosen to investigate the influence of the frequency of different gas fillings. Both share the same operation network, whose de-embedding results are explained in this section followed by the plasma fitting of the PC-lamp.

4.4.1 Shared Network in Circuit and FEM Simulation for DUTs

The measurements of the PC-lamp and the xenon filled hollow cylinder configuration are made using an existing 50 Ω network.

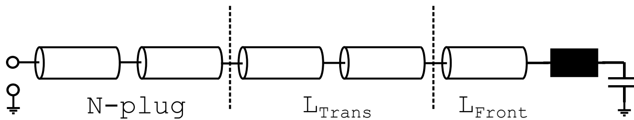

Figure 4.16: Representation of the measuring adapter inside the circuit simulator consisting of five different coaxial lines. At the end, an inductor and capacitor to ground are located which substitute the plasma of the PC-lamp and the XHC.

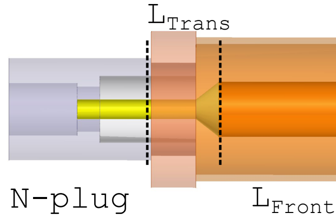

Figure 4.17: FEM simulation model of the shared network for the PC-Lamp and the XHC. Areas are indicated to identify the corresponding areas in the circuit simulation model.

It is shown in Fig. 4.17 and consists of a standard N-plug including an attached coaxial network, whose size is extended to the diameter of the devices under test. The network is able to sustain input power levels of up to 100 W. For the xenon

cylinder, a shorter version of this network is used. The fitting process of the shorter version is omitted since the mismatching is only in the phase.
In [12] this topology is used for an electrode-less energy saving lamp. These energy saving lamps included a dielectric conductor within the lamp to increase the propagation of the RF-signal into the plasma. Before introducing this conductor, the plasma was only existing in the first third of the burner and thus not being efficient. After integrating another glass tube with a specified diameter to match the impedance of the plasma, the plasma filled the whole burner. Even by increasing the power the light intensity was increased. The dielectric conductor is left out of the DUTs to elaborate the effects of the different frequencies.
The set-up inside the circuit simulator is shown in Fig. 4.16, represented by five different coaxial lines. From the terminal, the signal flows through the N-plug and the widening of the network. At the end, of the network, the inner conductor is slightly longer than the outer conductor. It is symbolized by the inductor. The pen end of the network is substituted with a capacitor. It is removed by the plasma de-embedding. The FEM simulation model is shown in Fig. 4.17. Areas corresponding to the each other are indicated in both plots. Both FEM simulation set-ups can be found in Fig. 4.20 and Fig. 4.27.

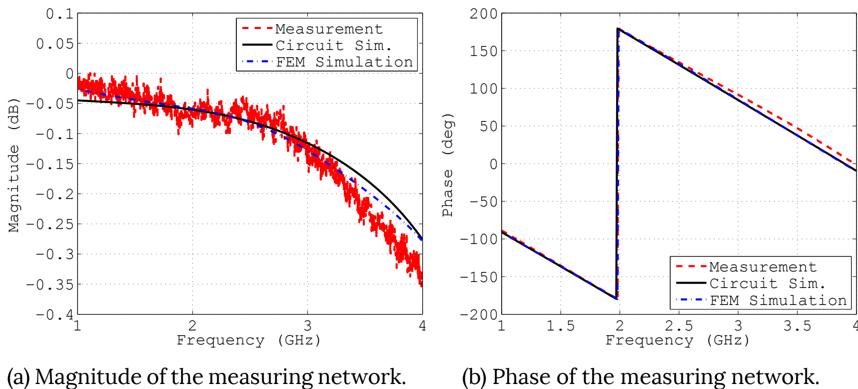

(a) Magnitude of the measuring network.

(b) Phase of the measuring network.

Figure 4.18: S_{11} values of the fitting of the measuring network used for the PC-lamp and the XHC.

Fig. 4.18 displays the magnitude and phase of the reflection measurement, circuit and FEM simulation. The model exhibits a relative error of less than 2% for the

magnitude and the phase. Fitting of the network from 1 GHz to 4 GHz is done in two stages using the circuit and FEM simulation. The fitting of the phase shows a good agreement of the measurement and both models.

4.4.2 PC-Lamp Plasma Representation

The frequency dependence on an enclosed low-pressure argon-mercury plasma is determined by the PC-Lamp. It is filled with low pressured argon as start gas. After its ignition the temperature increases and the mercury is ionized. The emitted UV-light is converted to the visible light spectrum by the phosphor coating. A metallic knitted fabric around the lamp prevents radiation of the RF power.

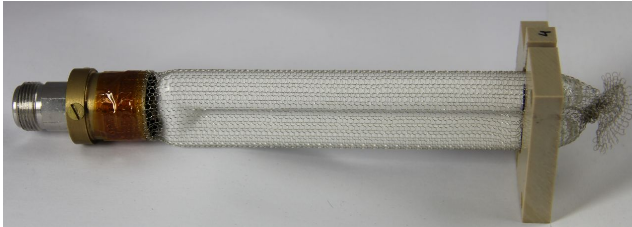

Figure 4.19: Prototype of the PC-lamp including the measuring network, metallic knitted fabric for shielding and a polyoxymethylene (POM) frame for fixation.

Fig. 4.19 shows the manufactured prototype including the network described in the previous section. Radiation of the electro-magnetic field is constrained by a metallic knitted fabric. A polyoxymethylene frame provides the fixation of the lamp.

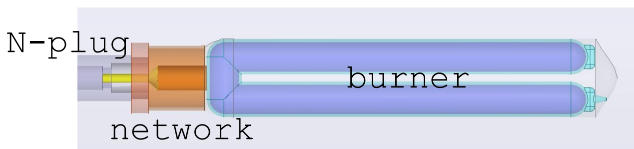

Figure 4.20: Cross-section of the FEM simulation model of the PC-lamp, including the N-plug and the measuring network.

The FEM representation of the lamp is shown in Fig. 4.20.
In this thesis, the PC-lamp is operated with power levels from 2 W to 10 W at all frequencies. At 1.3 GHz the linear output power of the amplifiers cannot compensate

the low matching of the lamp. Therefore a maximum input power of 5 W can only be measured for this band.

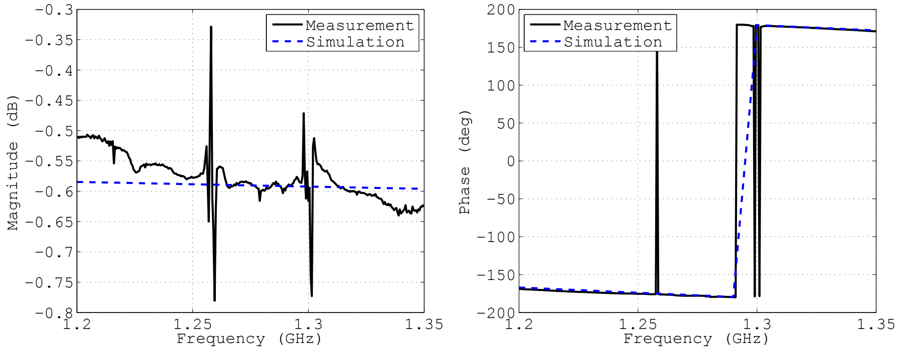

(a) Measurement and simulation of the plasma using a single conductivity.

(b) Phase of measurement and simulation.

Figure 4.21: S_{11} results of the plasma simulation for the PC-lamp using a single conductivity body inside the burner for a frequency of 1.3 GHz and an input power of 5 W.

Fig. 4.21 shows the exemplary plot of the measurement at 1.3 GHz and the fitted FEM model with a single plasma body of a constant conductivity of $0.5\,\mathrm{S\,m^{-1}}$. As explained in Sec. 4.3.1.2 the usage of several decreasing conductivities might improve the fitting. Further simulations with several plasma bodies did not yield an improvement of the fitting. The loss tangent is set to 0, the relative permittivity and the permeability are set to 1.

4.4.3 Measurement and Simulation Results of the PC-Lamp Base Point Impedance

Coaxial transmission lines substitute the measuring network in the circuit simulator for de-embedding as shown in Fig. 4.16. The base point impedance of the PC-Lamp is determined. All results do not exceed an error margin of 10%.

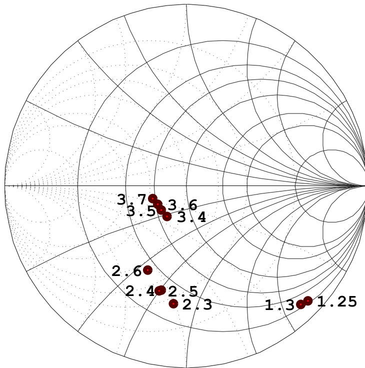

(a) Input power of 2 W.

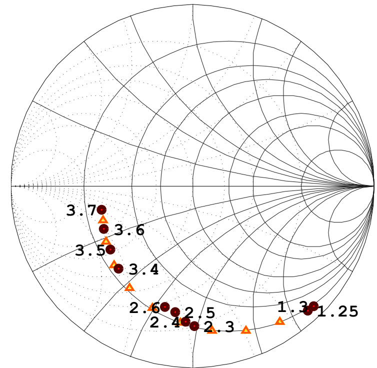

(b) Input power of 5 W with constant conductivity results from FEM simulation.

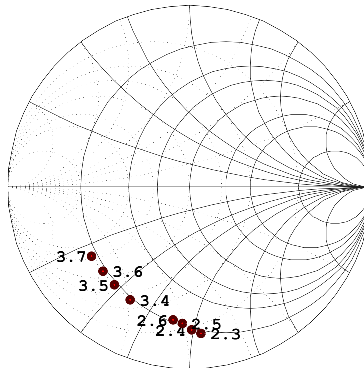

(c) Input power of 10 W. No measurements at 1.3 GHz were possible.

Figure 4.22: De-embedded measured complex reflection values of the PC-lamp at 2 W, 5 W and 10 W.

4.4.3.1 Base Point Impedance Determination of the PC-Lamp

First the measurements are de-embedded and the corresponding base point impedance is determined. Second, the plasma is fitted using a matching network. The de-embedded S_{11} results for two different power levels at 2 and 5 W are illustrated in Fig. 4.22a and 4.22b with indicated frequencies. At 10 W the 1.3 GHz band could not be measured. Therefore the Smith Chart in Fig. 4.22c contains the result of the other frequency ranges only.
At an input power of 2 W the highest base point impedance of $(38.5 - 13.3\text{i})\,\Omega$ is at 3.5 GHz, while the lowest value is $(15.2 - 123.9\text{i})\,\Omega$ at 1.25 GHz. The values of the reflection measurement do not follow a linear path.
A linear connection of the de-embedded reflection parameters and the resulting base point impedances is visible for power levels at 5 W an above. At 5 W an almost constant real part of the base point impedance of 10.8 Ω at 1.3 GHz, 13.2 Ω at 2.4 GHz and 15.6 Ω at 3.5 GHz are determined.
Only the phase of the de-embedded values changes significantly from −120.3° at 1.3 GHz, over −45.7° at 2.4 GHz to −10° at 3.5 GHz. This is also visible in the Smith Chart in Fig. 4.22b. In this plot the circle on which the values are located is of a constant real part. Only the phase decreases counter-clockwise.
A possible connection of the base point impedances across the frequencies is visible for input powers of 5 W and higher. In Fig. 4.22b the simulation of a constant conductivity of $0.5\,\text{S}\,\text{m}^{-1}$ and a constant relative permittivity of 0.5 is plotted.
For all frequencies from 1.3 GHz to 3.7 GHz this constant conductivity is able to fit the base point impedance within an error margin of 5%. With this constant value, it is possible to estimate the behavior of the base point impedance for the PC-Lamp in the white space between the investigated frequency bands.

4.4.3.2 Plasma Fitting with a Circuit Simulator of the PC-Lamp

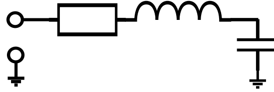

Figure 4.23: PC-Lamp plasma model for the representation in the circuit simulator. It consists of a series resonance circuit.

A series connection of an inductor and capacitor with tunable q-factor fits the plasma of the PC-Lamp in the circuit simulator. It is shown in Fig. 4.23. It is the same network used for the jet and the XHC.
Results of the fitting process in the circuit simulator are presented in Fig. 4.24 at all measured frequencies and power levels of the PC-Lamp. The simulation results are based on a series resonance circuit of an inductor and a capacitor. Below its resonant frequency, a series resonance circuit exhibits a capacitive impedance. Therefore the inductor is only used as the frequency-dependent element in the circuit simulator.
Values of the inductance L do not follow a monotonic connection over the frequency and power. Its highest values are simulated for the 2.4 GHz band. The inductor's q-value increases with the frequency within the measuring accuracy. The capacity is assumed to be constant over frequency and power. Q-value of the capacitor is constant and has been omitted due to visibility reasons. The maximum relative fitting error of the circuit simulation representation and the PC-Lamp plasma is about 6%.

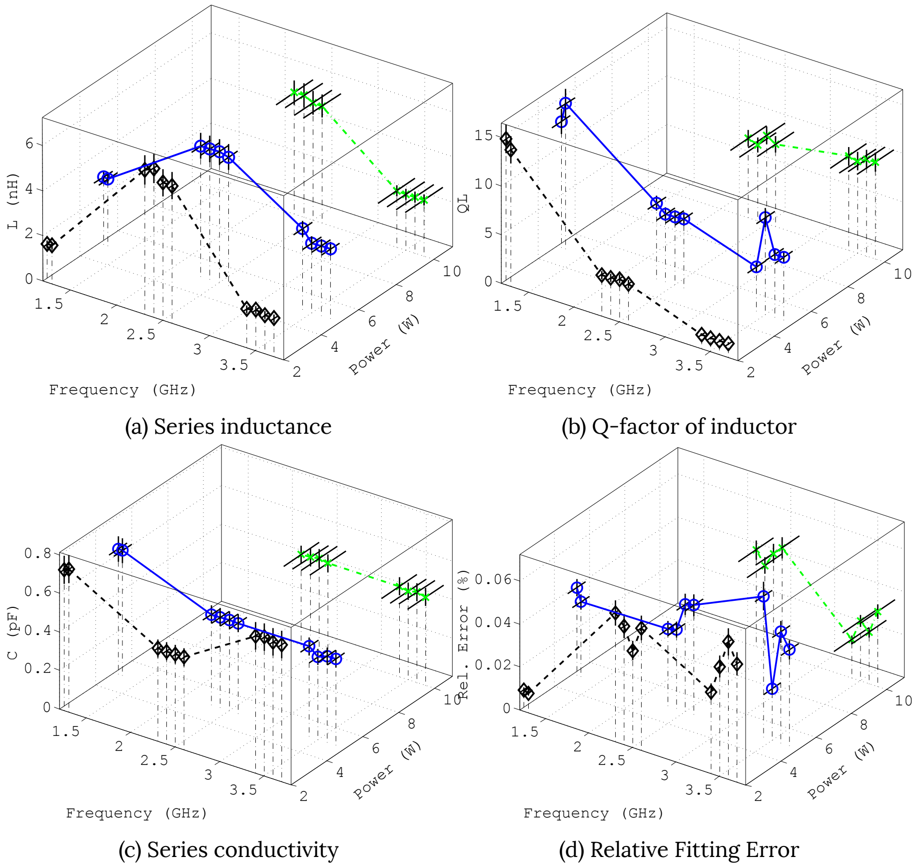

(a) Series inductance

(b) Q-factor of inductor

(c) Series conductivity

(d) Relative Fitting Error

Figure 4.24: Fitted values of the PC-Lamp plasma representation network in the circuit simulator. The network consists of a series resonance circuit of a capacitor and an inductor with a tunable Q-value.

4.4.3.3 Fitting of the PC-Lamp Measurements in an FEM simulator

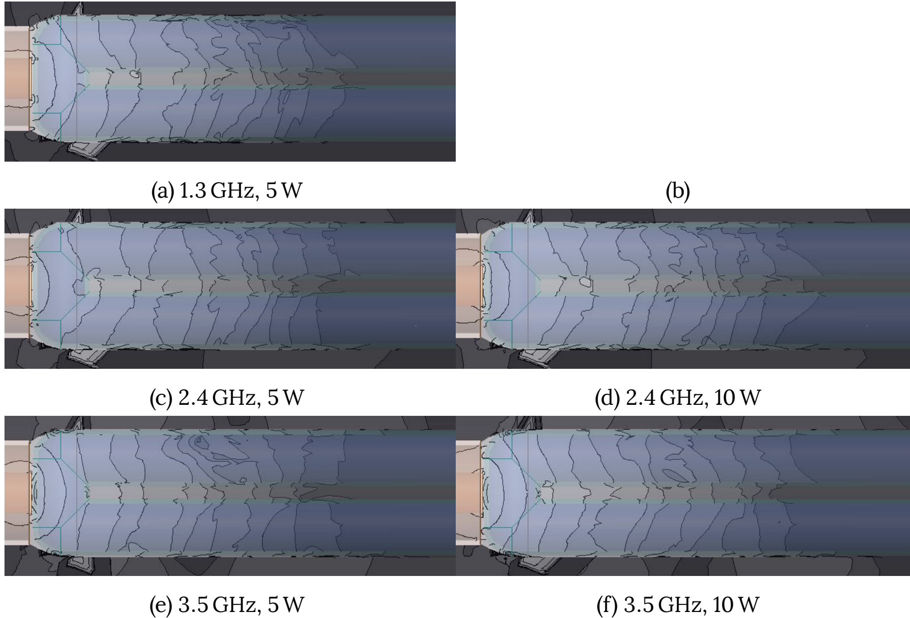

(a) 1.3 GHz, 5 W

(b)

(c) 2.4 GHz, 5 W

(d) 2.4 GHz, 10 W

(e) 3.5 GHz, 5 W

(f) 3.5 GHz, 10 W

Figure 4.25: Electric field distribution of the shielded PC-lamp at different frequencies and power levels.

In order to compare the electric field distribution inside the lamp burner, the results of the FEM simulations are plotted in Fig. 4.25 for the power levels of 5 and 10 W. The conductivity of each frequency and power is set to the determined value described in Tab. 4.2, along with the input power.
By comparing the influence of the frequency on the spatial extensions of the plasma in Sec. 5.2.2, no relation to the simulation can be found for input power levels below 5 W. As plotted in Fig. 4.22b, a constant conductivity of $0.5\,\mathrm{S\,m^{-1}}$ is able to fit the base point impedance at all frequencies. At 10 W the constant conductivity of about $0.45\,\mathrm{S\,m^{-1}}$ can be made for the frequencies around 2.4 GHz and 3.5 GHz since the measurements for the band around 1.3 GHz is missing.

Table 4.2: Fitted PC-Lamp Plasma RF conductivities obtained from the FEM simulator.

Frequency GHz	**Input Power** W	**RF Conductivity** $\mathrm{S\,m^{-1}}$
1.3	2	0.2
	5	0.5
	10	n/a
2.4	2	0.65
	5	0.55
	10	0.45
3.5	2	0.61
	5	0.53
	10	0.42

The resulting conductivities are given in Tab. 4.2. Within the bands, two different frequencies are simulated for verification. For each frequency band, a constant conductivity is fitted. While the frequency bands around 2.4 and 3.5 GHz exhibit the same conductivity, the values of the 1.3 GHz band change significantly at 2 W input power. Therefore the determined constant conductivity across all frequencies can only be verified for a limited window of power. Another interesting result is represented by the decrease in the conductivity and an increase in the input power. While at 2.4 GHz and 2 W the fitting resulted in a conductivity of $0.65\,\mathrm{S\,m^{-1}}$, it decreases to $0.45\,\mathrm{S\,m^{-1}}$ at the input power of 10 W.
In contrast to the plasma jet, the boundary conditions are more consistent since the plasma is enclosed and the radiation is constrained.
The geometrical dimensions of the PC-lamp allow the full extension of the plasma even at 10 W. The amount of energy reflected back into the plasma can be neglected. In case of the XHC reflected amount of the energy has to be considered, since an interference pattern is formed at 5 W of input power. The latter is explained in Chapter 5.2.3.
The investigated results may form the basis for a possible extension to an FEM model, which is defined by other plasma parameters. An almost constant conductivity is shown for an input power of 5 W. This would reduce the number of unknowns in Eq. (2.19). Only the number of electrons and the resulting collision

frequency would be unknown. Further investigations on this matter could involve the determination of plasma parameters by only measuring and fitting the RF conductivity for specific frequencies. Limitations of this model are the amount of mesh cells for the 3D bodies, defining the resolution of the local changes inside the plasma.
It is shown that the fitting of the plasma in the circuit and FEM simulation exhibit a close match to the de-embedded measurement of the base point impedance. A linear connection of the phase exists and has been verified by a complete solution.

4.5 Frequency-Dependent Electrical Properties of the Low-Pressured Xenon Hollow Cylinder (XHC)

The Xenon Hollow Cylinder (XHC) consists of a glass tube, filled with xenon at a pressure of 15 mbar. It has a length of 62 mm and a diameter of 16 mm. The glass tubes were manufactured by the LTI of the KIT[11] and have an inner volume of 0.043 m^3 and a glass thickness of 1 mm.

Figure 4.26: Photograph of the set-up XHC including the probe network and metallic knitted fabric.

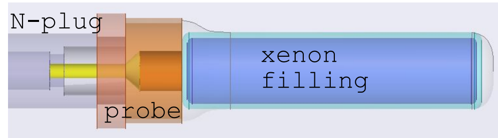

Figure 4.27: FEM model of the XHC to simulate the conductivity of the plasma.

A metallic knitted fabric provides the shielding similar to the PC-lamp. The XHC prototype including the shielding and the probe network is presented in Fig. 4.26. This device was chosen for the measurements to evaluate the differences in the electric properties of a typical lighting gas. Its simple geometric form simplifies the modeling process in the simulators. Xenon-filled burners can be found in e.g. automotive head lights. Therefore potential differences in the frequency dependence of argon and xenon can be assessed.
A shorter version of the 50 Ω network explained in Sec. 4.4.2 is used for the measurements. This network exhibits the same magnitude and shows just a minor difference in the slope of the phase. The FEM model of the lamp is plotted in Fig. 4.27. As in the case of the PC-lamp and the jet, only a single cylinder with a constant conductivity substitutes the plasma in the 3D-model.

[11] Lichttechnisches Institut of the Karlsruhe Institute for Technology

4.5.1 Measurement and Simulation Results of the XHC-device

The XHC device measurements are conducted following the same procedure as for the PC-lamp. A detailed description of the used network and the procedure itself can be found in Section 4.4.2.

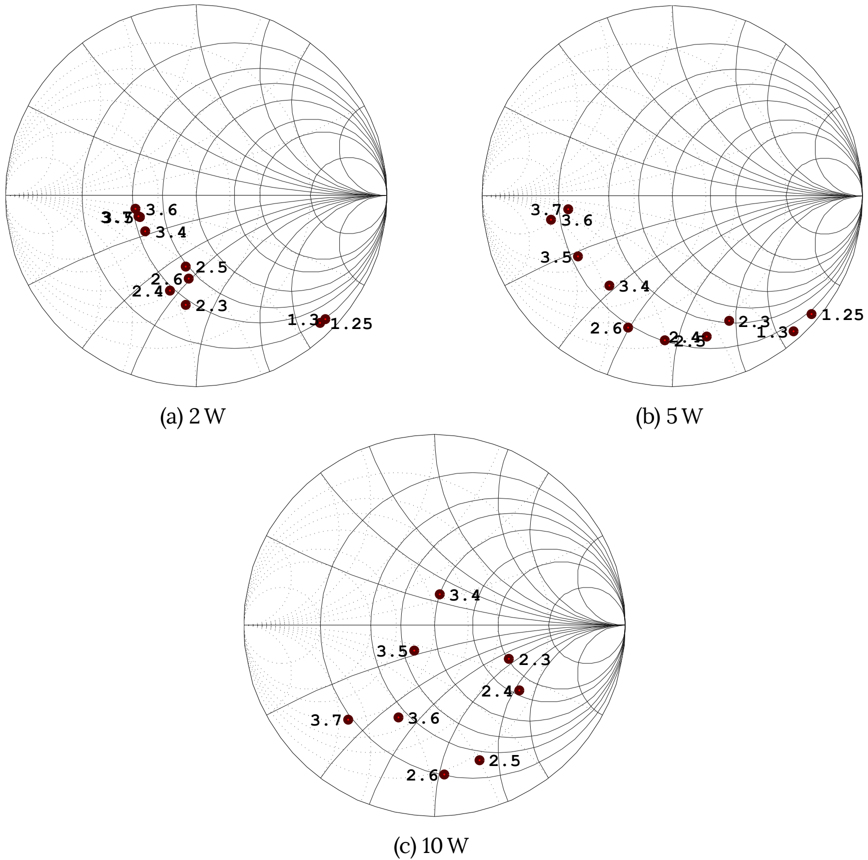

(a) 2 W

(b) 5 W

(c) 10 W

Figure 4.28: Frequency-dependent S_{11} reflection values of the XHC at different power levels from 2 W to 5 W and frequencies from 1.3 GHz to 3.5 GHz.

4.5.1.1 Base Point Impedance Determination of the XHC

The network shown in Fig. 4.16 is used for de-embedding the XHC in the circuit simulator. Reference plane of the base point impedance[12] is located at the tip of the inner conductor.
Fig. 4.28 displays the comparison of the de-embedded plasma S_{11} reflection values, which are calculated in the circuit simulation. Input power levels from 2 W to 10 W are compared. No data could be measured for frequencies around 1.3 GHz at 10 W. For an input power of 10 W a random pattern spread appears across the Smith chart. This behavior correlates with the observation that the amount of reflected power is sufficient to produce visible interference patterns inside the burner.
At 2 and 5 W a possible connection between the frequency and the conductivity is distinct. All frequencies are located on a single admittance circle in the Smith Chart, which is the equivalent of a constant real part of the complex reflection values. It only changes its imaginary part. Therefore, a parameter sweep using different conductivities is performed in the FEM simulator and then fitted to the measured data. No monotonic connection of the frequency and the conductivity is found as in the case of the PC-lamp.
At 10 W of input power the results are erratic and do not follow the possible connection observed at the lower power levels. This behavior correlates to the results measured in Chapter 5.2.3. The burner of the XHC is not completely filled at lower power levels, while at 10 W interference patterns of the standing wave inside the plasma are visible. Due to the interference of the reflected wave, the base point impedance is changed and cannot be replicated by a constant conductivity inside the simulator.

[12] Combination of glass and plasma electrical properties

4.5.1.2 Plasma Fitting of the XHC in the Circuit Simulator

The microwave plasma representation of the XHC in the circuit simulator is rebuilt by using the same network as for the PC-Lamp.

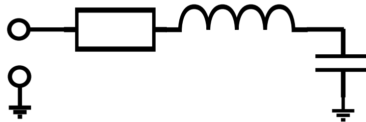

Figure 4.29: Series resonance circuit schematic for the plasma representation of the XHC in the circuit simulator. The resistor substitutes the losses of the circuit.

In Fig. 4.29 the series resonance circuit is shown, which simulates the frequency-dependent plasma electrical properties by lumped elements. The losses of the series resonance circuit's losses are substituted by the resistor. Frequency-dependent losses of the circuit are represented by the Q-values of the inductor and the capacitor.
As shown in Fig. 4.28 all determined base point impedance values are located in the capacitive area of the Smith Chart, which is the lower half circle of the diagram.
Below its resonance frequency, a series resonance circuit can be seen as a frequency-dependent capacitance. Therefore the inductor only substitutes the frequency-dependent part of the plasma. Main influence on the base point impedance is caused by the capacitor. A detailed explanation is given in Section 4.1.
As for the PC-Lamp, the chosen model consists of a series resonator circuit of an inductor and capacitor, which is shown in Fig. 4.29. Both are simulated with a tunable frequency-dependent q-factor, which is illustrated by the resistor in the schematic. By this fitting it is shown that the plasma fitting of two different gases (argon and xenon) and two different prototype configurations (PC-Lamp and XHC) are possible by the same underlying lumped element model.

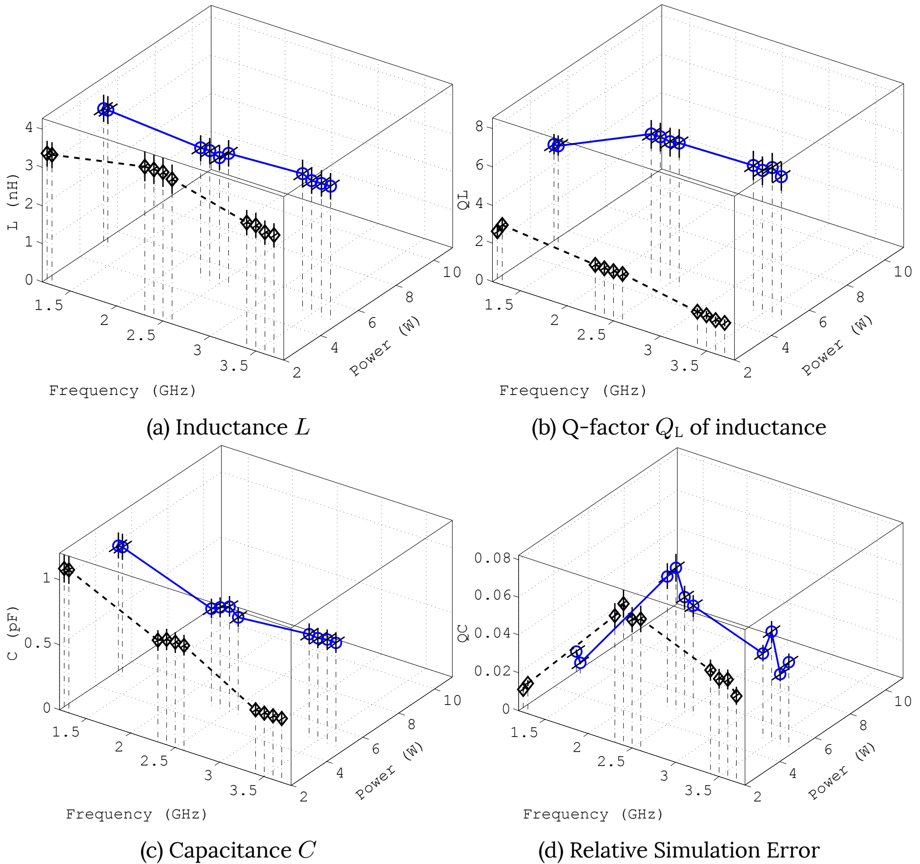

(a) Inductance L

(b) Q-factor Q_{L} of inductance

(c) Capacitance C

(d) Relative Simulation Error

Figure 4.30: Values of the XHC plasma representation by lumped elements in the circuit simulator at power levels from 2 W to 5 W from 1.3 GHz to 3.5 GHz.

The next step is to verify the possible connection between the frequency and the base point impedance in the circuit simulator. All measured frequencies and power levels for the simulated plasma representation of the XHC are visualized in Fig. 4.30. Simulations for 10 W input power could not be made since the chosen model did not fit with any parameter combination.
Values of the inductance and capacitance are inversely proportional to the input power. Q-Factors of the inductor increase with the power, while the q-factor of

the capacitor changes only slightly. Both the values of the inductance and the inductor's q-factors are inversely proportional to the frequency. The values of the capacitance are inversely proportional to the frequency, while the q-factor of the capacitor exhibits a constant value of 300 at all frequencies. Therefore the q-factor's plot has been omitted.

Comparing these values to the determined base point impedance in Fig. 4.28 shows that the main influence on the impedance is caused by the capacitance. This behavior supports the chosen lumped element model for the XHC plasma representation. The mean relative error of the fitting to the measurement is plotted in Fig. 4.30d with a maximum value of 7% at 2.4 GHz.

For the analysis, the XHC's spectral properties have to be taken into account. At 2 and 5 W the burner is not completely filled by the plasma. This allows a fitting by the series resonance circuit model. A higher input power leads to interference patterns within the XHC's burner. Fitting of this interference pattern is not possible by the presented lumped element model.

To further investigate the connection of the conductivity, the plasma is modeled in the FEM simulator.

4.5.1.3 3D-Modeling of the XHC plasma in an FEM simulator

In Fig. 4.27 the FEM simulation model of the XHC is illustrated. The shielding of the device under test is included in this simulation and is visible by the spline curves at the transition from the probe to the burner and the end of the glass cylinder. The curve was rotated around the axis to become a surface emulating the losses of the meshes. Spacing of the meshes is set by surface conditions. The sizes of the plasma are represented by a length of 60 mm and a radius of 7 mm.

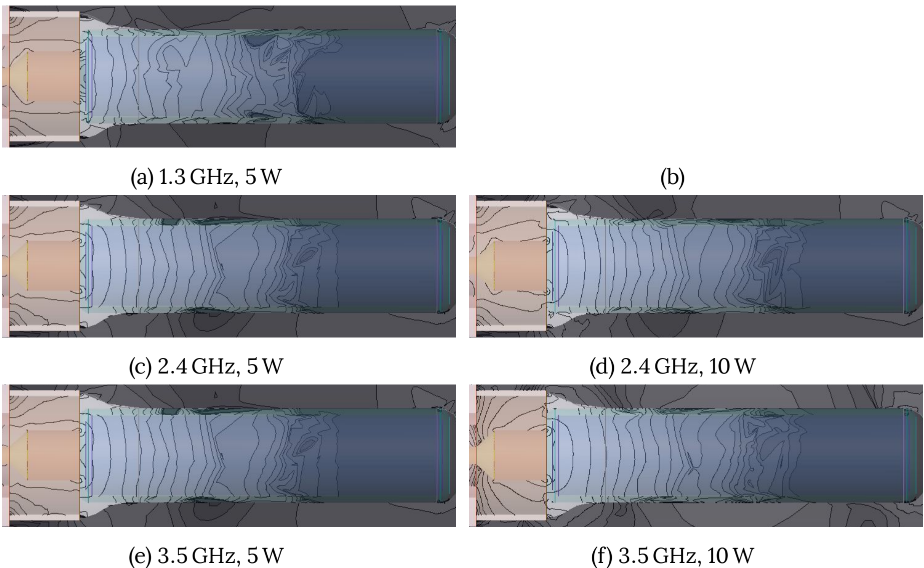

(a) 1.3 GHz, 5 W (b)

(c) 2.4 GHz, 5 W (d) 2.4 GHz, 10 W

(e) 3.5 GHz, 5 W (f) 3.5 GHz, 10 W

Figure 4.31: Electric field distribution of the shielded XHC at frequencies of 1.3 GHz, 2.4 GHz and 3.5 GHz and power levels from 5 W to 10 W.

To compare the electric field of the different measurements, it is plotted in Fig. 4.31. The phase is set by the maximum electric field strength inside the burner.
These plots point out the limitation of the plasma modeling using a lossy dielectric with a finite conductivity and permittivity. It is possible to model the electric parameters in terms of matching and electric field strength. As described in the

following chapter, the length of the XHC device helps to visualize the interference pattern of the standing electro-magnetic wave. The pattern is explained in Chapter 5.2.3. Using the finite conductivity and permittivity the field distribution of the standing wave cannot be reproduced. Another approach is possible by simulating the plasma meta-material through dielectric loss tangent and permittivity.

Table 4.3: Overview of the fitted values for the extracted RF conductivities at different power levels and frequencies for the XHC-device.

Frequency	**Input Power**	**RF Conductivity**
GHz	W	$\mathrm{S\,m^{-1}}$
1.3	2	0.05
	5	0.03
	10	0.02
2.4	2	0.15
	5	0.21
	10	0.26
3.5	2	0.28
	5	0.35
	10	0.45

FEM simulations of the XHC at each measured frequency and input power level are performed for the verification of the constant conductivity. In Tab. 4.3 the simulated results are given for each of the measured data points. The lowest values are calculated for the band around 1.3 GHz and increase with the frequency.

4.5.1.4 Summary of the XHC-Device Frequency-Dependent Electrical Properties Analysis

A frequency dependency analysis of the XHC's plasma electrical properties is presented.
Extraction of the measured base point impedance based on the measured S_{11} reflection values is given, resulting in a strong dependence on the frequency and the power.
Using a lumped element lossy series resonance circuit model, the plasma is fitted in the circuit simulator. It is verified, that the proposed model with a dominant

and frequency-dependent capacity fits the plasma within a low error margin of 6%. Hence it becomes obvious that this model is consistent for microwave plasmas of different gases, pressures, and topologies.
Fitting of the XHC's plasma conductivity at different frequencies using a 3D-model in an FEM simulator is presented. Conductivity of the plasma is proportional to an increase in the frequency and the power. It is shown that the electrical properties of the plasma are fitted only by a variation of the conductivity[13].
All presented analyses are made during the course of this thesis.

[13]Real part is changed, imaginary part is constant

4.6 Modeling of Argon Microwave Plasma By Electrical Transmission Properties

Electrical properties of microwave atmospheric plasmas in this chapter have been analyzed based on reflection measurements. The used approach satisfies the requirements for most applications, since just the impedance of the RF network has to be adapted to the specific plasma. Electro-magnetic energy entering the plasma is partly reflected at different positions inside the plasma and superimpose each other[14]. The sum of this reflected wave is measured as the reflection coefficient and lacks spatial resolution. This spatial resolution can be recorded by measuring the electro-magnetic energy transmitted through the plasma.
All measurements and fittings were made during the course of this thesis.

4.6.1 Description of the Transmission Measurement Adapter Prototypes

This section describes the development of the different prototypes for the frequency-dependence of the plasma transmission properties. Boundary conditions are determined by two prototypes followed by a third one to conduct the measurements.

4.6.1.1 Final Network Prototype for the Measurement of Microwave Plasma Transmission Properties

Two prototypes are built up to identify the boundary conditions of the measurements and analysis.

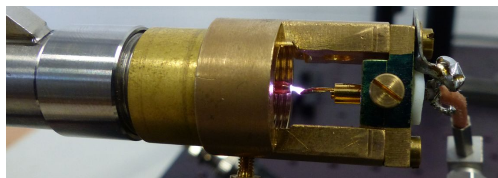

Figure 4.32: First prototype for the transmission measurements to explore and prepare the boundary conditions for the operation of a microwave plasma.

[14]Most of the other energy is absorbed by the plasma

A simple first set-up is created, which is shown in Fig. 4.32. It consists of the plasma jet presented in Sec. 4.7 onto which a special head is mounted. The second electrode is taken from a standard N-plug with an SMA[15]-cable is attached. The distance between the electrodes can be varied by screwing and unscrewing the head. This set-up was used to measure the influence of the distance between the electrodes and to determine the possible combinations of gas flow and input power level.
A disadvantage of this first measuring set-up is the radiation caused by the aperture of the device. The wave impedance of the system is unknown. Therefore no measurements are presented.

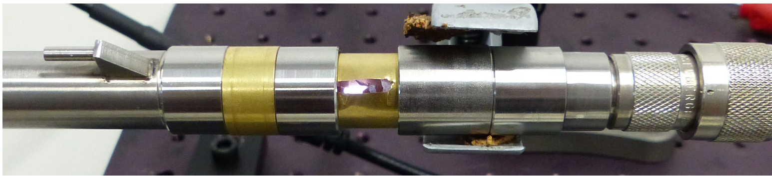

Figure 4.33: Second plasma transmission prototype using a coaxial topology to imprint a fixed and known wave impedance for the whole test fixture.

These problems are solved by a second prototype, shown in Fig. 4.33 with an ignited argon plasma between the inner conductors. It consists of the plasma jet used in Sec. 4.3 and a 50 Ω measuring probe of the DHPL presented in Chapter 3. The inner conductors are facing each other in a fixed distance of 2.5 mm. Brass foil held in place by a hollow glass cylinder forms the outer conductor of the coaxial system. A small gap in the glass and the foil is left open to ignite the plasma. The smaller aperture of this device prevents the RF power from radiating while providing a fixed wave impedance for the de-embedding process.

[15] SubMiniature Type A

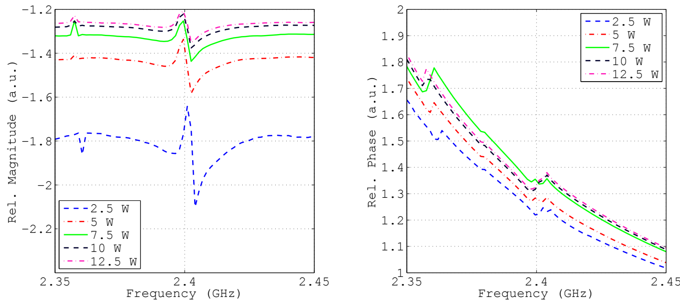

(a) Relative magnitude and phase changes in the transmission values of the second transmission prototype at different power levels and a fixed gas flow of 1 L min^{-1}.

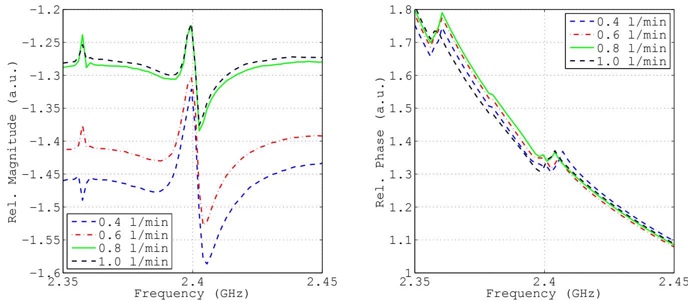

(b) Changes in the transmission magnitude and phase caused by variations of the gas flow from 0.4 L min^{-1} to 1.0 L min^{-1} and a fixed input power of 10 W.

Figure 4.34: Overview of the impact of power and gas flow changes on the magnitude and phase of S_{21}. Measurements are made using the second transmission prototype for visualization purposes and verify the influence of the investigated parameters.

In Fig. 4.34 the measured relative changes in the S_{21}[16] values are shown. For this, either the input power or the gas flow is fixed to a constant value, while the other parameter is swept. All measurements had to be made in a single measurement set-up and could not be reproduced.
Fig. 4.34a displays the swept frequency of the measurement from 2.3 GHz to 2.6 GHz using a fixed power level of 10 W and a constant argon flow of 1 L min^{-1}.

[16] Transmission values

Relative changes in the frequency are visible for the magnitude of the impedance within a window of about 10 % within the measuring accuracy.
In Fig. 4.34b the gas flow and the frequency are fixed to 1 L min^{-1} and 2.4 GHz respectively. The power is changed from 2.5 W to 12.5 W. For the magnitude, the highest change is measured at the lowest input power and decreases with an increase in the power. At higher power levels a saturation effect can be seen.
It is shown that the change of the gas flow and input power influence the magnitude and phase of the transmission properties of the plasma. Impact on the magnitude of the S_{21} values is higher as on the phase and thus an indication that the main influence of the conductivity is the amount of generated free charge carriers and their resulting collision frequency. Low impact on the phase indicates a small change of the relative permittivity within the plasma.
Measurements with this set-up were not reproducible since the interconnection boasted fragile behavior. In addition, the fixed gap width of the second prototype limits the possibilities for the measurements.

4.6.1.2 Final Network Prototype for the Measurement of Microwave Plasma Transmission Properties

The Final Transmission Network Prototype (FTNP) for the transmission measurements is built up based on the former designs.

Figure 4.35: Built-Up prototype for the final transmission measurements. It consists of the plasma jet and a network for the HFD-lamp, which are connected by a custom-built screwable interconnection.

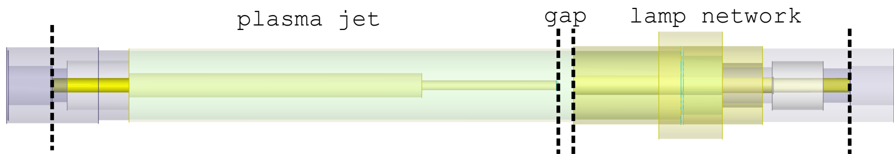

Figure 4.36: 3D-model of the final transmission prototype with annotated areas.

The glass tube and brass foil are exchanged by a screwable connection enabling reproducible measurements across all frequencies bands. It is illustrated in Fig. 4.35. The 3D-model for the calculation of the conductivity is presented in Fig. 4.36. The used parts of the prototype are annotated, too.
The length of the inner electrodes is chosen to short the connection between the two adapters. Shorting the adapter is required to perform the calibration[17]. After the calibration process, the references planes are located on the tip of both electrodes.
By unscrewing the adapter, the distance between the electrodes is adjustable. The distance is measured by the difference of the outer casing using a caliper and are based on the relative changes to the shortened position.
Different process gasses can be inserted via the front inlet. The gas exits the inner electrode (cannula) of the jet, where it feeds the plasma between the electrodes. Teflon discs are inserted into both adapters to prevent the process gas from leaking. All measurements are made using a fixed gas flow of $0.8\,\mathrm{L\,min^{-1}}$.

[17] Unknown thru response calibration[117].

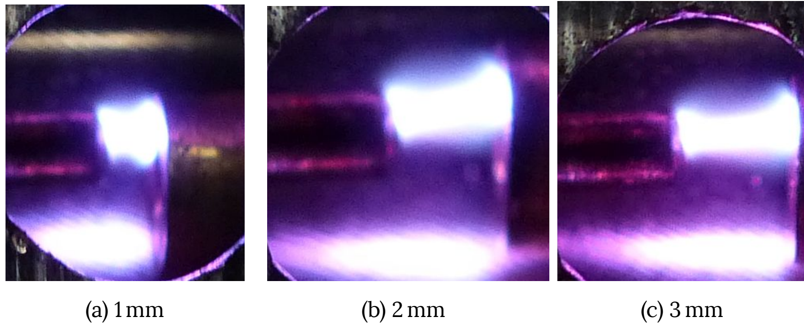

(a) 1 mm (b) 2 mm (c) 3 mm

Figure 4.37: Argon plasma at different gaps. Input power of 10 W is constant at an excitation frequency of 3.4 GHz and a gas flow of 0.8 L min^{-1}.

Argon plasmas at different gap sizes between the electrodes are shown in Fig. 4.37. Simulations show the vertical shift of the electrode does not have a significant effect on the conductivity of the plasma. On the left, a gap size of 1 mm at 3.5 GHz is set. The pictures in the middle and the right within the figure show a gap distance of 2 mm and 3 mm. Vertical size of the plasma decreases while increasing the distance between the electrodes. This effect has also been taken into account in the simulations.

4.6.2 Fitting of Microwave Plasma Transmission Parameters using Lumped Element- and 3D-Modeling

This section describes the fitting of the microwave plasma transmission parameters for frequencies around 1.3 GHz, 2.4 GHz and 3.5 GHz, power levels from 5 W to 15 W and gap width from 1 mm to 3 mm.
A lumped element model is presented for the representation of the parameters in the circuit simulator. The resulting transmission base point impedances are shown. A single capacitor with a frequency-dependent q-value fits the plasma for all conducted measurements.
For the calculation of the parameters in the FEM simulator, a 3D-model is shown. A new model using a core/cone representation is presented along with a comparison to a cylindric plasma body. Based on a detailed error analysis of the new model, the fitting of the plasma using only the conductivity is presented.

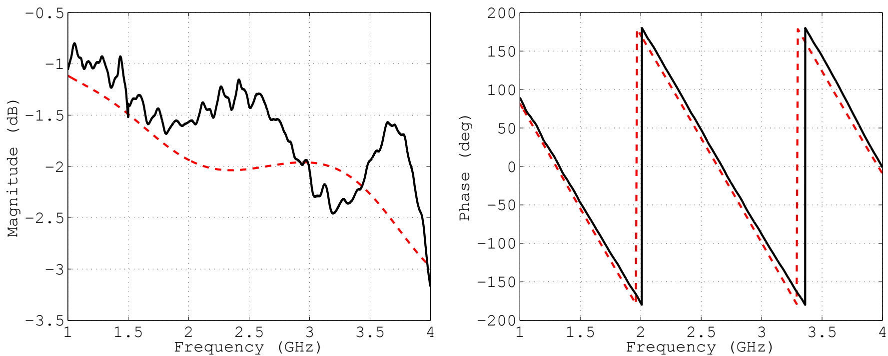

(a) S_{21} transmission value of the magnitude of the measurement and ADS fitting for prototype with shorted gap.

(b) Phase of the S_{21} transmission value.

Figure 4.38: Overview of the S_{21} transmission values for the FTNP with a closed gap. Both measurements and model in the circuit simulator are shown.

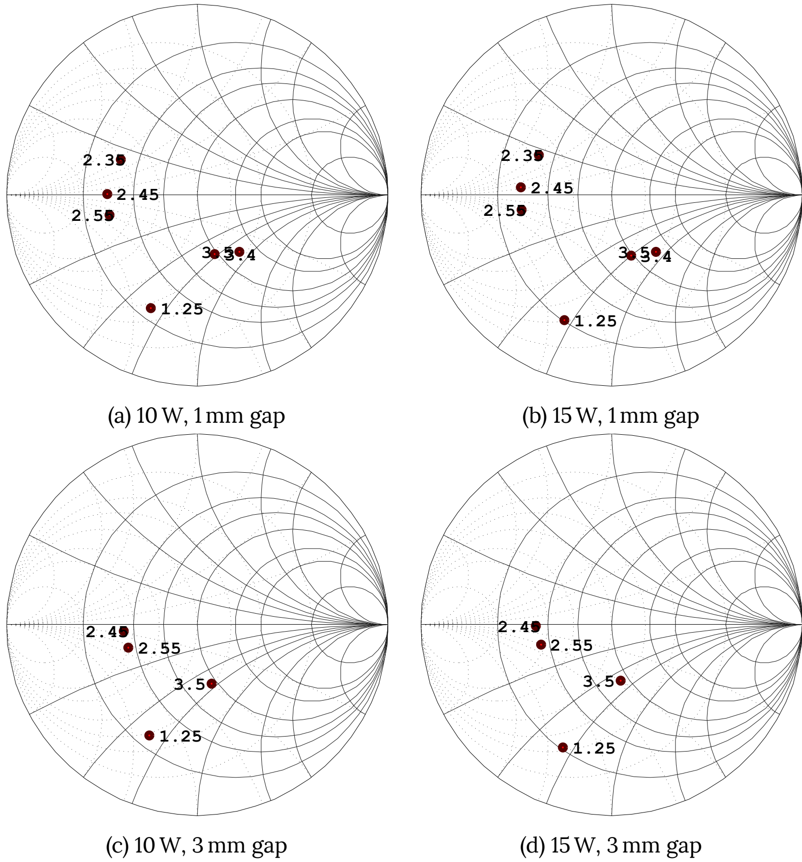

(a) 10 W, 1 mm gap

(b) 15 W, 1 mm gap

(c) 10 W, 3 mm gap

(d) 15 W, 3 mm gap

Figure 4.39: De-embedded transmission plasma base point impedance of the FTNP for 10 and 15 W input power at different distances of the electrodes.

4.6.2.1 Fitting of the Plasma Transmission Parameters using a Lumped Elements Model

For the generation of a lumped element model of the plasma transmission parameters, the measurements are loaded into the circuit simulator and a model is built up.
Based on the existing model of the plasma jet (Sec. 4.3.1.1) and the operation network of the HFD-Lamp (Sec. 3.3.3.2) the model of the FTNP is created. It consists of a series connection of ten coaxial lines.

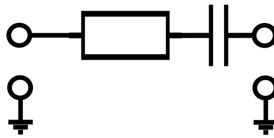

Figure 4.40: Lumped element model for the fitting fitting of the FTNP plasma. A series conductor with a tunable q-factor is utilized. The q-factor is represented by the series resistance.

In Fig. 4.38 the results of the fitting process from 1 GHz to 4 GHz for the FTNP with a closed gap[18] are shown. Four different reference measurements including gap distances from 0 mm (short) to 3 mm in 1 mm steps are fitted and used for the de-embedding process. The figure shows the shorted measurement and fitted model in the circuit simulator for the transmission. An error of 10% is achieved for the broadband fitting. This accuracy is the main influence on the variance of the final results of the lumped element model.
The black-box method[19] is utilized and the values of the base point impedance of S_{11} and S_{21} are determined.
Fig. 4.39 displays the de-embedded transmission impedance of the FTNP at different frequencies, input power levels and gap sizes. All measured data points are located close to each other. A non-monotonic connection between the frequency and the base point impedance of the plasma exists for the transmission based on the black box method. Plots for the 2 mm gap have been omitted since they do not show any significant change compared to the other gap sizes.

[18] Connection is shorted
[19] De-Embedding of the measurements without a fitting by a model.

Table 4.4: Circuit simulation results for the transmission network using a single capacitor and a tunable frequency-dependent q-factor.

Frequency	**Power**	**1mm**		**2mm**		**3mm**	
(GHz)	**(W)**	**C (pF)**	**QC**	**C (pF)**	**QC**	**C (pF)**	**QC**
1.3	5	0.7	1.8	0.7	1.8	0.6	1.8
1.3	10	1.1	1.8	1.05	1.8	0.95	1.8
1.3	15	1.3	3.5	1.3	3.1	1.3	1.9
2.4	5	0.35	1.3	0.25	1.3	0.15	0.6
2.4	10	0.7	0.8	0.17	0.6	0.25	0.9
2.4	15	0.35	3	0.23	0.8	0.15	0.4
3.5	5	0.6	0.5	0.35	0.5	0.15	0.5
3.5	10	0.7	0.8	0.4	0.4	0.13	0.25
3.5	15	0.75	0.45	0.45	0.35	0.15	0.15

Changes in the gap size or input power do not show a measurable effect on an electro-magnetic wave traveling through the plasma. Only the frequency has a significant impact on the base point impedance, which is again caused by the different wavelengths. These results also show that another frequency can be chosen to design an application based on its requirements. It underlines the importance, that the frequency introduces a degree of freedom. A simple extraction of an equation based model is not possible.
Inside the circuit simulator, a capacitor with a tunable q-value substitutes the plasma between the electrodes. It is shown in Fig. 4.40 and consists of a series capacity with a tunable frequency-dependent q-factor. In the model, it is represented by a series resistor.
In Tab. 4.4 the overview of the fitted model values of the plasma at all gap sizes, power levels and frequencies for the FTNP is presented. Since the bands exhibit a margin of 5%, the center frequencies are shown.
At 1.3 GHz the capacitance increases with the power as does the q-factor for all three gap sizes. By increasing the frequency to 2.4 GHz the course of the capacitance and the q-factor does not follow a linear path and shows a rather random behavior. The same situation can be seen for the highest frequency around 3.5 GHz where the capacitance increases for gap sizes of 1 and 2 mm but is distributed randomly at 3 mm. It appears also for the q-factor.
A simple frequency-dependent trend is visible for some of the fitted parameters:

Values of the capacity are inversely proportional to the frequency of a fixed gap size and power. The capacity is reduced at higher frequencies.
For a fixed frequency and power level the capacity is inversely proportional to the gap size. It follows the same principle as a plate capacitor, which exhibits a reduction of its capacitance at higher electrode distances.
Values of the q-factor are reduced with an increase of the frequency and a fixed gap size and input power. It is caused by the change of the energy density, which is proportional to the frequency.

4.6.2.2 Fitting of the Transmission Plasma Parameters using a 3D-Model in an FEM Simulation

A 3D-model of the FTNP is rebuilt in the FEM simulator to determine the conductivity of the plasma transmission conductivity. This is done to achieve a good 3D-

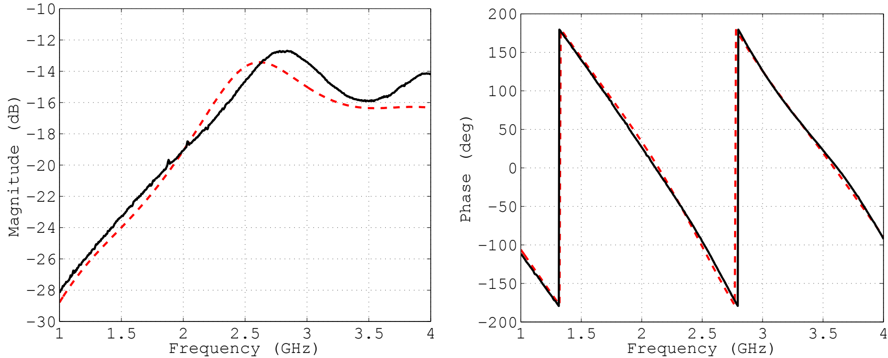

(a) Magnitude of the S_{21} transmission values for the measurement and the fitting using the 3D-model of the FTNP.

(b) S_{21} transmission phase values of the fitting and the measurements.

Figure 4.41: Overview of the broadband S_{21} transmission values of the magnitude and phase for the FTNP from 1 GHz to 4 GHz. Measurement (dashed line) and fitting (solid line) are presented.

model of the properties of a microwave plasma.
In Fig. 4.41 the overview of the S_{21} transmission values of the fitted 3D-model and the measurement for the FTNP for the frequency range from 1 GHz to 4 GHz is shown. An error margin of 8% is calculated for the broadband fitting.
For the representation of the plasma in the 3D-model the cylindrical plasma body of the jet[20] The conductivity of the material is set to a constant value.

[20] Sec. 4.3.1.2 is utilized for the first approach.

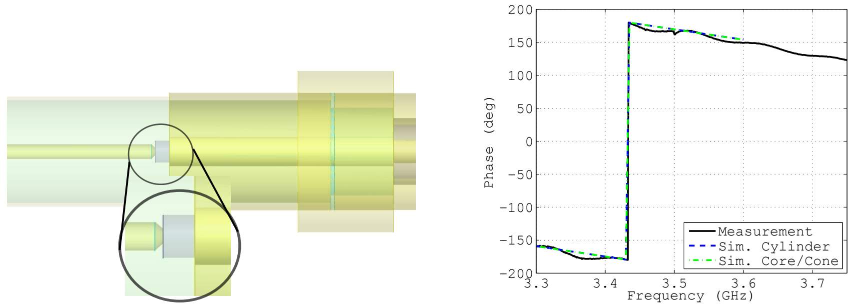

(a) Single cylinder model of the plasma fitting for the transmission of the FTNP.

(b) S_{21} transmission value of the phase of measurement, single cylinder model and the new core/cone model.

Figure 4.42: Overview of the measurement and the different plasma fitting models. The single cylinder model is simulated with a diameter of 1 mm.

Fig. 4.42 shows the final size of the plasma cylinder for 1.3 GHz. The physical dimensions of the cylindric model do not fit the plasma since the diameter is more than doubled. An exemplary overview of the S_{21} transmission value phase is presented in Fig. 4.42b. The phase of both the measurement and the fitting are close to each other. One aim of the FEM simulations is the reproduction of the correct physical

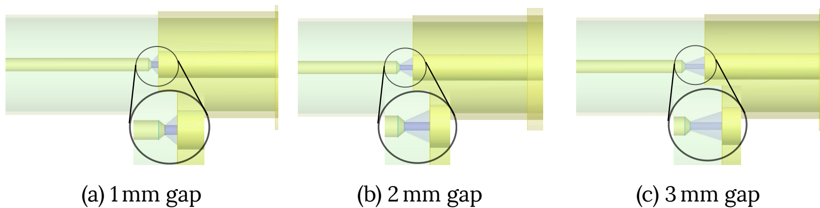

(a) 1 mm gap

(b) 2 mm gap

(c) 3 mm gap

Figure 4.43: HFSS plasma models for the different gaps between the electrodes from 1 mm to 3 mm. The power is coupled in from the left side.

attributes. The diameter of the cylinder does not match the spatial extensions of the plasma. Therefore an updated model consisting of a core cylinder and a surrounding cone is introduced (further: core/cone): This model is extracted from different photographs, where a more light intensive part is located in the middle of the plasma. Less illuminated parts are represented by the cone.

The conductivity of the inner core is tapered[21]. This means that is always higher than that of the outer cone.

All gaps from 1 mm to 3 mm of the core/cone model are plotted in Fig. 4.43. Maximum diameter of the inner core is set to the size of the inner conductors opening, which is 0.6 mm. Size of the core's diameter is varied to satisfy the spatial extensions of the different frequencies. At 1.3 GHz the maximum size is set, while at 3.5 GHz a reduction down to 0.3 mm is necessary. The size of the cone is fitted with a parameter sweep. In Fig. 4.42b the fitting results of the core/cone model are plotted. This emphasizes the correct fitting while maintaining the spatial extensions of the plasma.

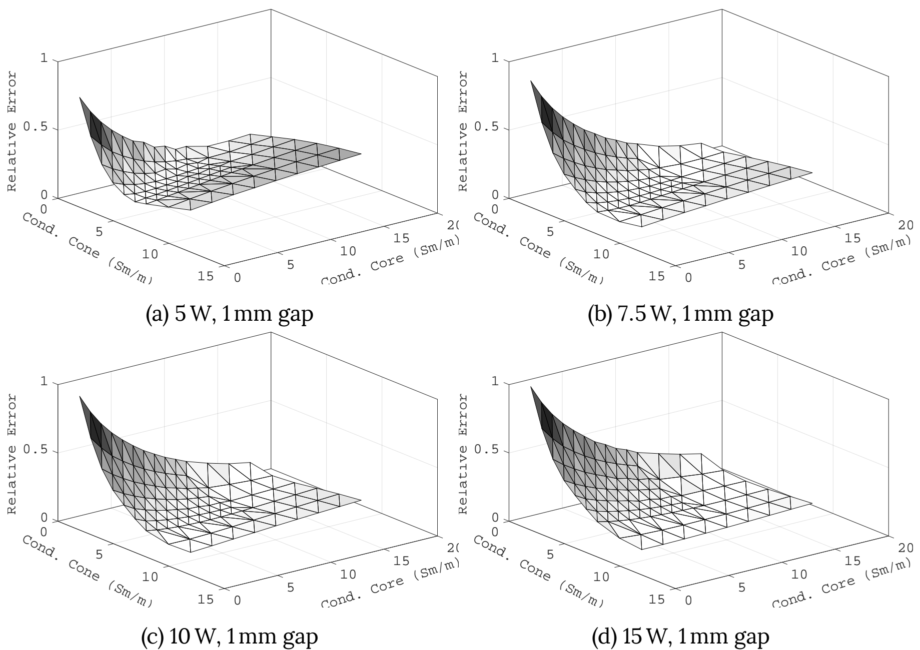

(a) 5 W, 1 mm gap

(b) 7.5 W, 1 mm gap

(c) 10 W, 1 mm gap

(d) 15 W, 1 mm gap

Figure 4.44: Relative errors for the different power levels of the transmission fitting in the FEM simulator. Fitting is made for a gap of 1 mm at 2.4 GHz.

[21]Same approach is used for the jet plasma fitting.

Simulations are run with a parameter sweep for the following variables:

- inner core: diameter, conductivity and relative permittivity[22],
- cone: diameter of the larger side, conductivity, and relative permittivity.

A change of the relative permittivity does not yield any significant changes. Therefore the conductivities represent the electrical properties of the plasma for the FTNP. The amount of parameter sweeps is reduced by setting the relative permittivities to a constant value of 1. The results are exported to Matlab, where a custom-written routine analyzes and visualizes the fitting error. Lowest error is calculated for S_{11} and S_{21}. A 3D surface is generated by the routine to show the influence of the different conductivities. The outputs of the scripts for a frequency of 2.4 GHz at power levels from 5 W to 15 W are presented in Fig. 4.44.
Both conductivities are plotted on the x- and y-axis, while the absolute error of the fitted model is located on the z-axis. A lower value on the z-axis corresponds to a lower absolute error. The sum of the measuring error (Sec. 4.2.5) and the accuracy of the de-embedded model are required for the margin of the error. With a minimum source matching of -32 dB for a minimal measured matching of -5 dB, the relative error of the measurement is about 1%. The simulation error of the broadband fitting is about 10%. Therefore the summed relative error is about 11% for the transmission measurements. The relative error is not plotted in Fig. 4.44 due to visibility reasons.
The iterative process of the parameter sweep is started with a rough spacing of the conductivities to identify the areas of the lowest error. After this, the granularity of the spacing is refined which is also visible in the plots where the mesh points are denser distributed. A shading effect is overlayed for a better visibility.
The combination of three frequencies (1.3, 2.4 and 3.5 GHz), four power levels (5, 7.5, 10 and 15 W) and three gap sizes (1, 2 and 3 mm) is fitted, resulting in a total of 36 data points.

[22] Exact fitting possible only for transmission measurements

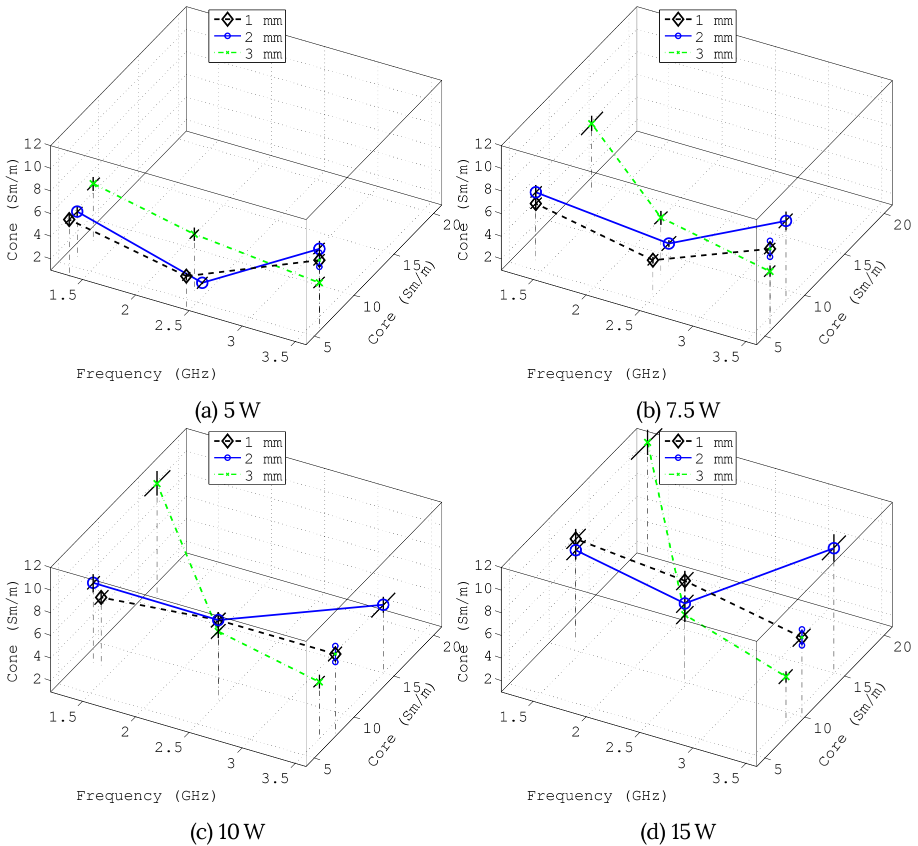

(a) 5 W

(b) 7.5 W

(c) 10 W

(d) 15 W

Figure 4.45: Fitted S_{21} transmission values for the FTNP conductivity of the plasma body at power levels from 5 W to 15 W and electrode distance from 1 mm to 3 mm.

The results of the frequency-dependent fitted conductivity are presented in Fig. 4.45 at the power levels from 5 W to 15 W. The frequency from 1.3 GHz to 2.4 GHz is located on the x-axis, while the y- and z-axis show the conductivities of the core/cone model. For a better visibility, a single frequency of the three bands is shown. All other frequencies vary within a 5% margin. For the comparison of the power levels this value is fixed and the frequency dependency is plotted for all gap sizes.

The error bar for each of the conductivities is plotted on each data point. As described above the accumulated relative error is about 11%. It would result in a circle on the yz-plane with a diameter of the measuring error. Due to visibility reasons, this circle is only indicated with the bars.
Both conductivities increase the power independently from the gap between the electrodes.
At 1.3 GHz the highest value is simulated for the 3 mm gap at each power level. Conductivities at 1 and 2 mm exhibit almost the amount. The maximum value of $21\,\mathrm{S\,m^{-1}}$ for the core and $11\,\mathrm{S\,m^{-1}}$ for the cone is simulated for a gap of 3 mm at 15 W. All other measurements results are located within a close range.
For the frequencies around 2.4 GHz all values are within a 20% margin, but this band also shows the lowest fitted conductivities. The value of the core plasma cylinder is almost constant for this band. Maximum values of 11 for the core and $7\,\mathrm{S\,m^{-1}}$ for the cone are calculated.
At 3.5 GHz the highest spread between the single power levels is simulated. Starting from a constant value for the core conductivity at 5 W the distance between the different fitted points emerges. Highest value is simulated for a gap size of 2 mm at 15 W with $15\,\mathrm{S\,m^{-1}}$ for the core and $12\,\mathrm{S\,m^{-1}}$ for the cone.
The frequency dependency and gap size show a non-monotonic connection, like the jet. Only the power exhibits an increase in the mean conductivity. The overall energy level inside the plasma is increased by a higher input power generating more free charge carriers. This leads to a higher conductivity, which is mostly developed in the core part, which is the shortest connection between the two electrodes and therefore the area of the highest possible conductivity.

4.6.2.3 Summary of the Modeling of Frequency-Dependent Transmission Measurements for Microwave Argon Plasmas

In this section, the modeling of the microwave plasma transmission parameters is presented. This analysis has been made for the first time.
Two prototypes are built to determine the boundary conditions of the measurements, while the third prototype (FTNP) is built using the casing of the jet and the HFD-lamp operation network connected by a screwable interconnection. De-embedding of the FTNP using a lumped element and 3D-model is presented.

A simple lumped element model is created to fit the plasma transmission properties in the circuit simulator. A simple capacitor with a frequency-dependent q-value is sufficient for this purpose.
Creation of a new 3D core/cone model for the fitting of the plasma in the FEM simulator is shown. This model matches the physical dimensions of the plasma and only requires fitting of the conductivity's real part, while the relative permittivity is set to a constant value. This underlines the simple, but exact approach.

4.7 Discussion of the Results

In this chapter the frequency dependence from 1.3 GHz to 3.5 GHz of electrical properties of microwave plasmas has been investigated and analyzed. All works have been made during this thesis.
All investigated plasmas, except the jet, exhibit a capacitive dominated impedance. In the circuit simulation, a series resonance circuit substitutes the frequency-dependent capacity of the plasma. The simulated capacity is equal to the integral of the specific capacity of the plasma.
Three different devices have been measured and analyzed based on their S_{11}: plasma jet, PC-lamp and XHC.
The argon plasma jet at atmospheric pressure shows a strong dependence of the base point impedance on the frequency. It is shown that a single cylinder is capable of fitting the plasma's conductivity in the 3D-model.
Two enclosed microwave plasmas consisting of argon and xenon at low pressures have been operated with the same RF-network. The fitting of the plasma of both prototypes is made by a series resonance circuit. Below its resonance frequency this type of circuit has a capacitive dominated impedance. The inductivity is used only for the frequency-dependent behavior of the circuit. Both devices show a connection of the conductivity and frequency. In case of the phosphor-coated lamp a constant of $0.5\,\mathrm{S\,m^{-1}}$ fits the plasma using the 3D-model.
Analyses on the influence of the plasma on an electro-magnetic wave passing through are made with a purpose-built transmission network, which is the first of its kind. A new lumped element model is created to fit the plasma properties in the circuit simulator. It is shown that a single capacitor with a frequency-dependent q-value is sufficient to fit the plasma. The creation of a new 3D-model for the fitting of the plasma properties in an FEM simulator is presented. This new

tapered core/cone model consists of an inner core and an outer cone, which are matched to the physical dimensions of the plasma.
The electrical properties of a microwave plasma depend strongly on the frequency and it is possible to adapt the workflow for the development of a bi-static network to other microwave frequencies, while adding a new degree of freedom to applications.
Microwave plasmas have a capacitive dominated impedance for both reflection and transmission values. New simple lumped elements and 3D-models are created to fit the plasma in the simulator and exhibit are very good agreement with the measurements.

Chapter 5

Multi-Physical Analysis of the Microwave Plasma's Frequency Dependence

Microwave plasmas exhibit changes in electric properties with a change of the frequencies. This chapter contains the investigation and analysis of the multi-physical changes and properties of a microwave plasma. Relative to its change the frequency has a more significant impact than the input power on all of the measured parameters.
Geometrical dimensions of the plasma are extracted from pictures taken with a CMOS camera by a custom written image registration routine. It is shown, that the size is inversely proportional to the frequency and proportional to the input power.
Spectral properties of the plasma are measured and the participating ion species are analyzed. It is shown that light output is higher at lower frequencies and is caused by the proportionality of the size to the frequency. By normalizing the light output to the size, a constant ratio is discovered. Spectral properties of the jet plasma are analyzed in detail using optical emission spectroscopy (OES).

The frequency-dependence of the thermal properties is investigated. A strong dependence on the frequency is measured for the two enclosed plasma sources. Determination of the jet plasma's rotational temperature by OES is presented and values of up to 1350 K are measured.

5.1 Numeric Method for the Plasma Size Determination

This section covers the basics of two Matlab routines analyzing the different measurement data. An image registration and edge detection routine provides information on the two-dimensional analysis of the plasma body's size. A second routine determines the ion species of a spectral measurement with the help of the NIST atomic lines database. All routine are developed during the course of this thesis.

5.1.1 Image Registration Routine

The first routine detects the edges of the plasma and extracts information of the plasma size changes by image registration. Image registration is based on the Fourier transformation. The picture is transformed by a two-dimensional fast-fourier transform. Based on this transformation, filters can be applied to detect changes in brightness and edges. More details on this technique are described in [118]. The theory is explained in [119]. This routine requires the pictures to be taken

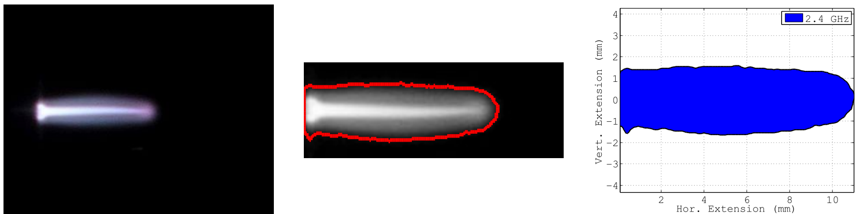

Figure 5.1: Different stages of the Matlab image registration routine.

at the same exposure time and f-stop. Otherwise, changes in brightness could not be detected correctly.

As described in Chapter 3, a simple CMOS camera is mounted on a tripod at a fixed distance and set to manual exposure. The pictures are loaded into by the routine performing the following actions.
First, the picture is cropped to remove unnecessary parts to avoid the increase of the computation time. An example can be found in the left image of Fig. 5.1. Maximum crop size is set by the plasma to the greatest extent. All other images are cut to these dimensions while the electrode is used as the reference point for the alignment. The gray-scale image is calculated and then loaded into a matrix with a value range of 0 for black and 1 for white. It prepares the matrix for the usage of the Lanczos algorithm, which is a fast linear algorithm to calculate the Eigenvector and Eigenwerte of a matrix for the edge detection. A custom fixed threshold for all images is set manually to gain a closed path around the plasma. This track is equal to the size of the plasma. In the middle image of Fig. 5.1 the detected path around the plasma is highlighted, which is equal to the detected size.

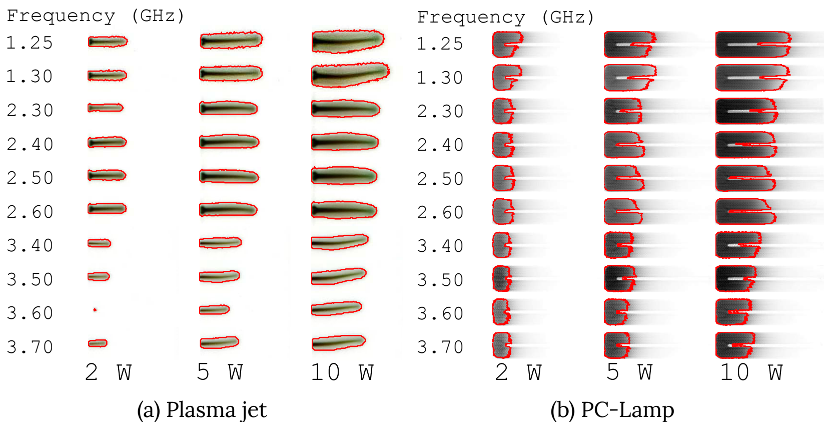

(a) Plasma jet (b) PC-Lamp

Figure 5.2: Plasma size at different frequencies and input power levels for the plasma jet and the PC-lamp.

Fig. 5.2 displays the results of the manual threshold fitting by comparing the generated surfaces for each power level and frequency. Threshold is chosen in a way that the maximum and minimum extent of the plasma are covered by the conversion. The column on the left shows the images for 2 W, in the middle for 5 W and the column on the right for 10 W. Each row represents a different frequency.

A scaling factor is calculated by taking a picture of a caliper and measuring the pixels forming a millimeter to convert the pixels to metric units. After scaling the size, a plot of the scaled plasma is plotted. An example of this plot is displayed in Fig. 5.1 for an example.
The conversion factor is the main influence on the error margin of this method. Relative error is calculated by summing up the amount of pixels forming a length of 10 mm. The variance is determined by the pixel width of the distance indicators on the caliper. At the beginning of each section, a comparison of the conversion factor and the corresponding variance is presented.

5.1.2 Ion Species Analysis Recognition

A plasma radiates electro-magnetic energy. It is caused by the change of energy levels of electrons and the generation of photons. This interaction of matter and the electro-magnetic waves allows the determination of the plasma composition. By varying the frequency in the mentioned ranges, the changes of the spectral emissions are measured and investigated. Spectral lines of the plasma are recorded. For the analysis of the spectral lines, the atomic lines database of the NIST is used to assess the transition probability and the ion species of the gas forming the plasma. The spectral line with the highest transition probability will be utilized for the determination of the ion species since the spectrometer exhibits a measuring accuracy of 1.5 nm. For a more detailed analysis of the plasma properties[1] a spectrometer of a higher resolution is required. Optical emission spectroscopy is described in [120], [121] and [122].
Argon and xenon are the process gases of the analyzed prototypes. These two process gases are analyzed with this method. Data is requested from the NIST using both elements in combination with the lower and upper wavelength.
Spectral lines are extracted by calculating the local extremes. These are compared to the obtained data within the measuring accuracy of the spectrometer, which is 1.5% at 850 nm. An overlay is plotted on the results to visualize the type of ion species for each spectral line.
The type of ion species is essential for the analysis of the thermal properties since the infrared camera detects the temperature between 6 µm to 13 µm. To ensure

[1] E.g. vibrational and rotational temperature, electron density

that the temperature measurements are not disturbed by emissions of the plasmas, the determination of the ion species is necessary. For example, in the case of argon, only ions with an ionization of four and higher are radiating energy in the wavelength area detected by the IR camera.

5.2 Frequency Dependence of the Geometrical Expansions

This section covers the influence of the frequency on the microwave plasma's geometrical expansions. A CMOS camera in combination with a routine analyzes the frequency dependence. More details on the routine can be found in Sec. 5.1.
The comparison of the plasma size is presented for each device under test (DUT): jet, phosphor-coated lamp (PC-Lamp) and xenon-hollow cylinder (XHC). Frequencies around 1.3 GHz, 2.4 GHz and 3.5 GHz at power levels from 2 W to 10 W were investigated in the frame of this thesis.

5.2.1 Frequency Dependence of the Plasma Jet's Geometric Expansion

The plasma jet is operated at atmospheric pressure conditions and argon is used as the process gas. Results of this section have been published in [116].

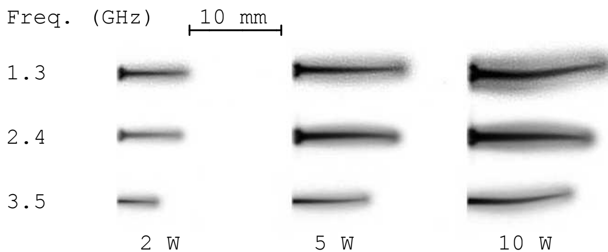

Figure 5.3: Gray scale images of different microwave plasmas generated by the jet at 1.3, 2.4 and 3.5 GHz at power levels from 2 W to 10 W.

An inverted gray-scale image of the plasma for the frequencies at 1.3, 2.4 and 3.5 GHz at power levels from 2 W to 5 W is plotted in Fig. 5.3. The size of the plasma increases by applying a higher power but decreases inversely proportional to the frequency. The changes in its extension occur in both, horizontal and vertical, directions. Areas of lower brightness around a bright inner part of the jet are visible. These brighter areas correspond to a higher energy density. Depending on the kind of application different spatial expansions are desired.

Table 5.1: Summary of the settings of the CMOS camera and the resulting calculated variances of the plasma jet size analysis measurements.

Frequency	Exposure Time	Pixels per 10 mm	Absolute Variance	Relative Error	Accumulated Relative Error
GHz	s^{-1}		px	%	%
1.3	80	128	3	2.7	5.7
2.4	80	130	3	2.3	5.3
3.5	80	106	2	1.8	4.8

Table 5.1 summarizes the properties of the photographs along with information on the resulting variance resulting from the conversion factor from pixels to mm. The last column displays the accumulated relative error describing the sum of the systematic error and the error resulting from the image analysis. A maximum relative error of 5.7% for the 1.3 GHz band is calculated, with a decreasing value at higher frequencies.

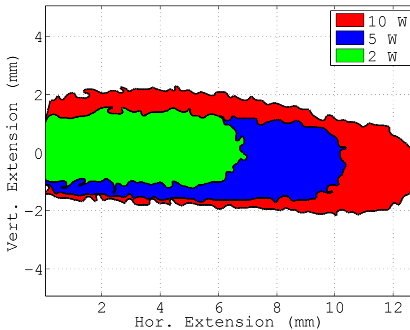

(a) Different plasma sizes for a constant frequency of 1.3 GHz at input power levels from 2 W to 10 W.

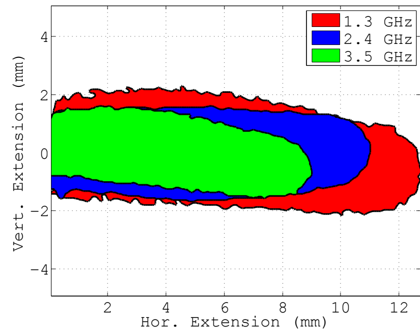

(b) Absolute cross-section size of a plasma across different frequencies for an input power of 10 W.

Figure 5.4: Comparison of the jet's plasma size at different frequencies and input power levels.

Results from the image registration routine in Matlab show the influence of the frequency and the input power level on the jet plasma size. These results are shown in Fig. 5.4. In this figure, the size is compared to a fixed power level of 10 W on the left side. The right side displays the size for a constant frequency of 1.3 GHz with a

varying power. With a maximum length of 12 mm the longest horizontal extension is located at 1.3 GHz, followed by 10.5 mm at 2.4 GHz and 9 mm at 3.5 GHz. Even by considering the accumulated relative error of the measurements the differences in size are still significant.
Within the bands, the size varies by the relative change of the frequency. At 1.3 GHz the horizontal extension ranges from 6.5 mm at 2 W, over 10.5 mm at 5 W to 12.5 mm at 10 W. The vertical extension increases from 2 to 4 mm. At 1.3 GHz an input power of 5 W results in the same spatial extension when using 10 W at 2.4 GHz.

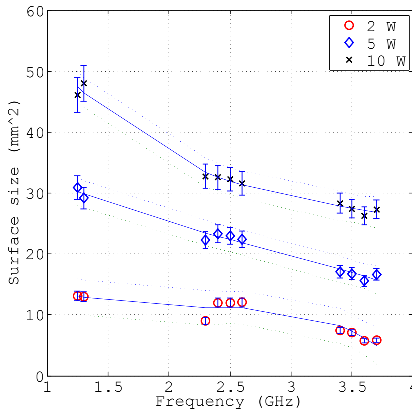

(a) Surface size of a cross-section through the jet plasma cylinder.

Frequency	**Input Power**	**Relative Wavelength**	**Relative Plasma Size**
GHz	W	%	%
1.3	2, 5, 10	100	100
	2		94.3
2.4	5	54.2	82.2
	10		49.2
	2		54.7
3.5	5	37.1	48.4
	10		41.2

(b) Numerical size values of the jet plasma compared to the size of 1.3 GHz.

Figure 5.5: Size of the jet plasma at all measured frequencies, power levels along with numerical values of the relative size changes compared to the results of the 1.3 GHz band.

The size of the jet plasma is approximated with a cylinder, whose height is determined by the horizontal, the diameter by the vertical extension. In Fig. 5.5 the calculated size comparison obtained from a cross-section of the plasma cylinder is shown. At 2 W input power, no trend can be determined. By increasing the input power to 5 and 10 W the previously described size changes of the plasma are apparent. This effect persists, when including the variance of the measurements. Table 5.5b shows the comparison of the measurement changes and the wavelength about 1.3 GHz. Significant changes can be observed for power levels of 5 W and

higher. At these power levels, relative changes converge to the wavelength ratio within the confidence interval of the measurements.

Changes in the jet plasma size caused by the frequency can only be explained by the difference in the wavelengths as explained in Chapter 2.4.1. In contrast to the frequency-dependent effect on a single electron, the size changes are not proportional to the wavelength. This is due to the more complex interaction of particles inside the plasma.

5.2.2 Frequency Dependence of the PC-Lamp Plasma

The plasma of the PC-Lamp is enclosed by quartz-glass, which is filled by a low-pressured argon-mercury mixture. It is coated with phosphor to transform the UV-light of the mercury into the visible spectrum. Therefore shorter exposure times of the CMOS camera are possible leading to a better signal-to-noise ratio for the analysis.

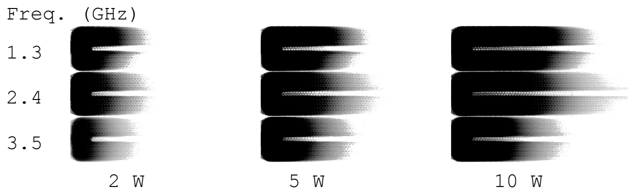

Figure 5.6: Inverted gray image comparison of the measured frequencies and power levels for the PC-Lamp plasma. Black represents the areas of highest brightness.

In Fig. 5.6 the gray images of the PC-Lamp plasma at different frequencies and input powers are shown. Size is proportional to the input power and inversely proportional to changes of the frequency. This behavior is the same as for the plasma jet at a different pressure. At 1.3 GHz and 10 W of input power, the highest expansion is measured.
The constant threshold is set to cover the highest brightness, which is represented by the black areas. Lighter areas could not be captured using a constant threshold to compare the size differences.

Table 5.2: Overview of the photograph properties and resulting systematic relative error for the PC-Lamp spatial results.

Frequency Band	**Exposure Time**	**Pixels per 10 mm**	**Absolute Variance**	**Relative Error**	**Accumulated Relative Error**
GHz	s^{-1}		px	%	%
1.3	2500	128	4	3.1	6.1
2.4	2500	126	4	3.1	6.1
3.5	2500	110	3	2.7	5.7

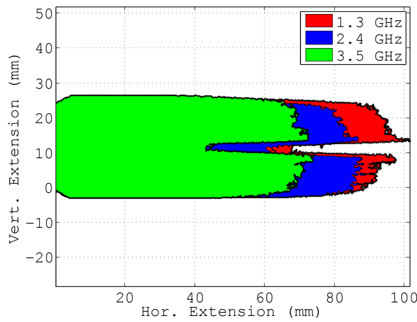

(a) Cross-section size across different frequencies for an input power of 10 W.

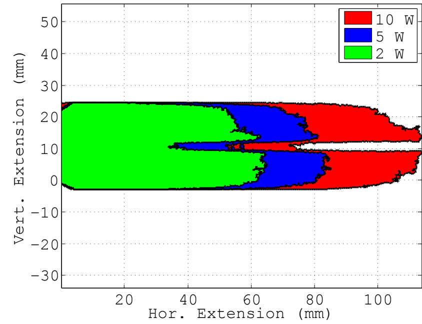

(b) Plasma sizes for a frequency of 1.3 GHz at input power levels from 2 W to 10 W.

Figure 5.7: Overview at different frequencies and input power levels for the PC-Lamp plasma.

To emphasize the influence of the frequency and the input power, a comparison with a fixed input power and excitation frequency is shown in Fig. 5.7. The gap in the middle of the lamp is not completely cropped due to the chosen threshold level. This threshold level is chosen with a focus on the horizontal expansion.
Table 5.2 displays the photograph properties and the resulting relative error. Compared to the plasma jet, the error is located within the same region with a maximum at 1.3 and 2.4 GHz. The position of the camera at 3.5 GHz is more distant from the object since the amount of pixels is decreased.
The converted absolute cross-section of the PC-Lamp for a fixed frequency with varying power is plotted in Fig. 5.7a. A fixed power level with varying frequency is shown in Fig. 5.7b. The maximum size of the PC-Lamp is 115 mm, whose size is sufficient to demonstrate the difference between the frequencies even at higher power levels.

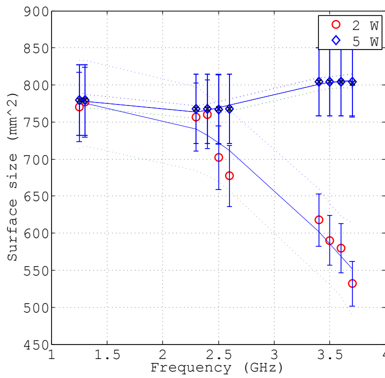

(a) Surface size of the plasma of the PC-Lamp.

Frequency	Input Power	Relative Wavelength	Relative Plasma Size
GHz	W	%	%
1.3	2, 5, 10	100	100
2.4	2	54.2	87.3
	5		88.7
	10		91.3
3.5	2	37.1	70.1
	5		67.8
	10		61.1

(b) Numerical values of the PC-Lamp relative to the size of 1.3 GHz.

Figure 5.8: Size of all measured frequencies, power levels, and relative size changes compared to the results of the 1.3 GHz band.

In Fig. 5.8 all measured data are plotted. At 2 W a decrease of the size is not distinctive. Increasing the power to 5 W shows a more pronounced fall of the size. Error bars indicate the relative systematic error. Due to a measurement error at 1.3 GHz, a wider confidence interval occurs at 10 W. This error results from a change of the exposure time to $1/3000\,\mathrm{s}^{-1}$.
Tab. 5.8b displays the relative changes of the size to 1.3 GHz. For this enclosed low-pressure plasma the sizes do not converge to the wavelengths even at higher power levels.
Changes of the size are comparable with the jet and are caused by the change of the wavelength. Boundary conditions like pressure and the glass surrounding the plasma do not affect the impact of the frequency dependence since the power is coupled in capacitively. It is important to notice, that the power at lower frequencies can be lowered to gain the same size of the plasma for the PC-Lamp. This is a possible increase in the plasma efficiency and leads to another degree of freedom for the design of enclosed plasma sources.

5.2.3 Geometrical Expansion of the Xenon Hollow Cylinder Plasma

The XHC is the second enclosed prototype and is filled with xenon. The frequency dependency of this gas is investigated in this subsection.

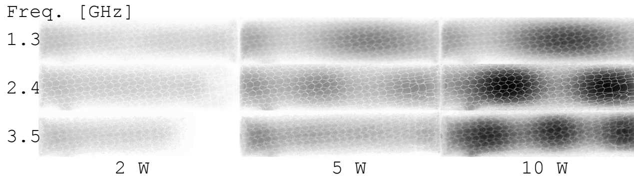

Figure 5.9: Inverted gray image comparison of the XHC plasma size at different frequencies and power levels.

As explained above, the Matlab routine calculates the inverted gray-scale comparison of the different power levels and frequencies. The results are plotted in Fig. 5.9. At 2 W the relative changes are visible by the surface size, while at 5 W all frequencies illuminate the whole probe volume. Parts of the volume are illuminated with a different intensity. By increasing the power up to 10 W these parts become more apparent and show the standing waves of the different frequencies. After entering the plasma and traveling all the way through the volume, the electro-magnetic waves are reflected at the end of the glass. The reflected parts are building an interference pattern inside the plasma. Simulation of the conductivity could be eased by this effect since the distribution of the electro-magnetic field is made visible by the plasma inside the XHC's burner.

Table 5.3: Comparison of the photograph properties and resulting systematic relative error for the XHC plasma size measurements.

Frequency Band GHz	**Exposure Time** s^{-1}	**Pixels per 10 mm**	**Absolute Variance** px	**Relative Error** %	**Accumulated Relative Error** %
1.3	200	127	4	3.1	6.1
2.4	200	132	4	3.0	6.0
3.5	200	110	3	2.7	5.7

Tab. 5.3 displays the different parameters for the conversion between the photographs and the spatial properties including the relative errors.

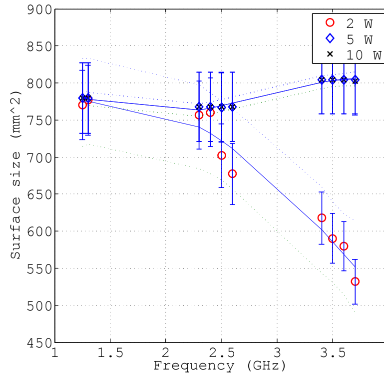

Figure 5.10: Absolute size of the plasma inside the XHC.

A comparison of the different surface sizes is plotted in Fig. 5.10 and the same behavior as in the visual comparison is visible. At the power levels from 5 W to 10 W the size stays constant. This is caused by the size of the plasma filling the whole volume at these power levels. Therefore the size is assumed to be constant. Since 90% of the captured images fill the inner cylinder of the XHC, no additional analysis and size comparison are plotted.
The plot of the absolute sizes is not presented since the cylinder is filled completely at 10 W for all frequencies. The changes of the illumination will be used to explain the differences. A difference can only be measured for an input power of 2 W, which is plotted in Fig. 5.10.
Comparing the spatial expansion of the PC-Lamp and the XHC, a difference in the spatial expansion is visible. At the same power level the spatial expansion of the PC-Lamp, which is filled with argon, is smaller. It is influenced by a different pressure of the plasma, which is higher inside the PC-Lamp and caused by the vapor pressure of the mercury. Another influence is the higher ionization energy (argon: 1520.8 kJ mol^{-1}, xenon: 1170.4 kJ mol^{-1}), which reduces the generation of free charge carriers.

5.2.4 Summary of the Geometrical Expansion Measurements

In this section, the frequency dependence of microwave plasmas was investigated. For these purposes an atmospheric plasma jet using argon, a phosphor-coated lamp filled with argon and mercury and a hollow cylinder cylinder topology filled with low-pressured xenon are analyzed.
All measured devices under test show the same behavior: the plasma size is proportional to the power and inversely proportional to the frequency. It is possible to achieve the same plasma size with a lower power at lower frequency. These observations add a new degree of freedom to the design of microwave plasma applications.
The measurements have been made during the course of this thesis and are the first of their kind at these frequencies and power levels.

5.3 Microwave Plasma Frequency Dependence Analysis by Optical Emission Spectroscopy

In this section, the spectral properties of the devices under test are analyzed.
As described in the previous section, the size of the plasma depends on the applied excitation frequency and the power. It is expected that an increase in size also increases the irradiance of the plasma. Therefore a normalization of the measuring results is required. For this, the total optical output is set in relation to the size of the plasma.
For the analysis of the spectral properties, the database of the NIST[2] is used. More details on the used routine can be found in Section 5.1.2.
A more detailed analysis of the jet based on measurement using a monochromator is presented in this section. Spectral lines are measured and the influence
For all measurements, the spectrometer is positioned in a fixed positioned of 0.30 m. As described earlier this adds 1% to the overall relative measuring error for a total of 5.4% of uncertainty.

5.3.1 Optical Properties and Optical Emission Spectroscopy of the Plasma Jet

Plasma jet applications like surface treatment and medical disinfection require different kinds of spectral parameters.
In the case of human tissue treatment, low UV-generation is desired to avoid harmful exposure. Industrial applications like surface manipulation may require different amounts of the different UV-spectra. For example, priming a surface for better adhesion requires a high UV-output at certain wavelength, which would react with the surface.
Infrared-emissions above 780 nm can only be used for thermal treatment and may have to be reduced depending on the application to reduce the thermal stress on the manipulated material.
More information on different areas of applications for the plasma jet can be found in [19], [22] and [17].

[2] National Institute of Standards and Technology

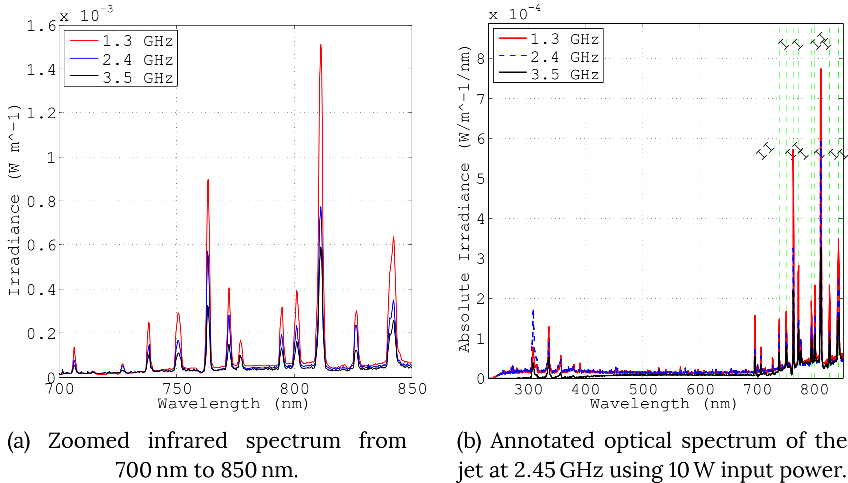

(a) Zoomed infrared spectrum from 700 nm to 850 nm.

(b) Annotated optical spectrum of the jet at 2.45 GHz using 10 W input power.

Figure 5.11: Spectrum and zoomed spectrum of the plasma jet at different frequencies for a constant input power of 10 W.

The optical spectrum presented in Fig. 5.11 shows the spectral lines of argon for the different RF frequencies from 1.3 GHz to 3.5 GHz at 10 W including a zoomed infrared spectrum.
Most spectral lines are developed below 380 nm and above 700 nm. At 1.3 GHz the highest irradiance is measured. A decrease in the optical output is shown for a constant power across the frequencies. For the same frequencies, a non-linear increase in the irradiance is visible. Within the bands, a 5% margin is measured. The difference in the irradiance is based on the spatial expansion, which is higher at lower frequencies and has been explained in Section 5.2.
For further analysis of the participating ion species of the plasma, the Matlab routine in combination with the NIST database is used. Since the only process gas is argon, only the ion species of this element is queried.
In Fig. 5.11b the optical spectrum of the jet for a frequency of 2.4 GHz at 10 W input power is plotted along with annotated vertical lines. These lines show the closest match of the NIST database. In addition, the ion species are plotted (Ar I = single ionization). Most of the lines show single ionization of the argon, but some lines in the infrared area show a second-degree ionization.

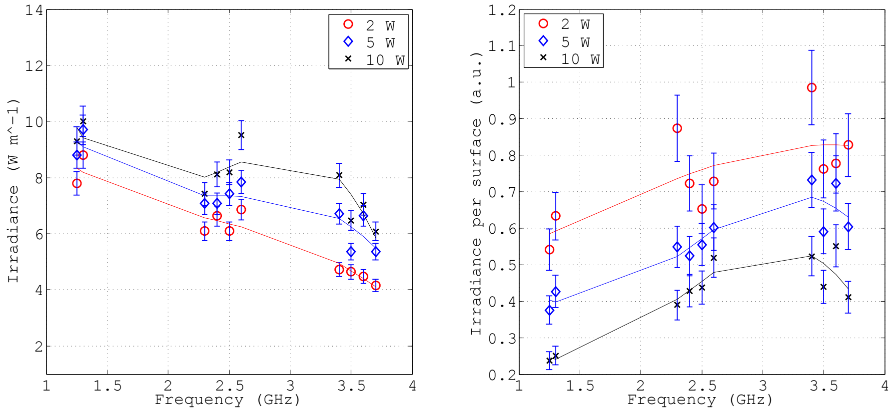

(a) Absolute measured irradiance at different frequencies and power levels.

(b) Irradiance to surface ratio of the plasma jet.

Figure 5.12: Measured irradiance and resulting ratio of the irradiance to the surface of the jet plasma.

The numerical values of the irradiance are plotted in Fig. 5.12a. At 1.3 GHz the highest values are measured. Irradiance decreases with a mean value of about 20% from 1.3 to 2.4 GHz and about 35% at 3.5 GHz. The relative error is indicated via a bar at every data point. The mean value of the measurements is shown via a fitted curve. Plots of the variance have been obtained due to lack of visibility. At 1.3 GHz the results at 5 and 10 W are switched due to a measuring error. This result is well within the relative measuring error window. These differences are caused by the changes of the spatial dimensions since the luminous surface is bigger at lower frequencies.
The ratio of irradiance and plasma volume is calculated and is plotted in Fig. 5.12b to visualize the influence of the plasma size on the illuminance. The ratio exhibits its highest values at the lowest input power. By increasing the power the ratio decreases. For constant power levels, the proportion is almost constant across all frequencies within the accumulated systematic error. This error is about 15%. This nearly constant ratio shows, that the frequency does not have an impact on the amount of power coupled into the plasma. If the ratio would decrease for certain frequencies, less power would be coupled into the plasma. For the jet, another

frequency range can be selected to adapt the plasma size to the desired application without sacrificing efficiency.
In the next section, the in-depth analysis of the plasma jet using optical emission spectroscopy is presented.

5.3.1.1 Optical Emission Spectroscopy of the Plasma Jet

In this sub-section the influence of the frequency, power, gas flow and gas composition on the size of different spectral bands of the plasma. All images have been scaled to the same size to allow a direct visual comparison of the effects.
The differences of a pure argon plasma generated by the jet is shown in Fig. 5.13. It displays the influence of the frequency and the power on the size of the plasma. All pictures are taken with a constant gas flow of 2 L min^{-1}. The size of the plasma increases with the input power and decreases with the frequency. Largest spatial extension is shown for 1.3 GHz and 15 W of input power. All pictures exhibit a corona-like effect around the plasma with an core of higher light intensity.
A size comparison of a pure argon plasma for the spectral bands around 310 (OH), 370 (N2), 696 (Ar) and 777 nm is shown. All images are taken with a constant input power of 10 W, a constant gas flow of 4 L min^{-1} at frequencies from 1.3 GHz to 3.5 GHz.
The corona-like effect of less light intensity is visible only for the OH-line around 310 nm and O-line at 777 nm. All other spectral images exhibit the area of higher light output in the core of the plasma. The color of the corona in Fig. 5.13 suggests other bands inside the visible area since the OH-line is located in the UV-range. At the time of the measurements, no other filters for additional measurement at other oxygen band was available.
The influence of the gas flow and different spectral ranges on the OH-band is presented in Fig. 5.15 for a constant input power of 10 W. Gas flow is swept from 1 L min^{-1} to 4 L min^{-1} and frequency from 1.3 GHz to 3.5 GHz. The plots of 4 L min^{-1} have been added to ease to comparison of the pictures.
At 1 L min^{-1} size of the plasma is almost constant in horizontal direction and extension only changes vertically. Almost no inner core is visible at this gas flow. By increasing the flow to 2 L min^{-1} the horizontal extent increases at all frequency while the vertical extent is decreased. At the end of the plasma, an area of increased brightness is recorded, which is connected via a slightly visible inner core to the

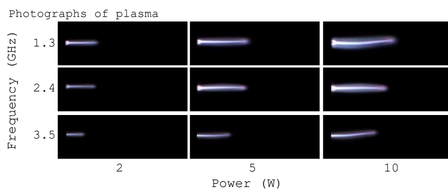

Figure 5.13: Plasma at different frequencies and input powers from 1.3 GHz to 3.5 GHz and 2 W to 10 W input power using pure argon as process gas.

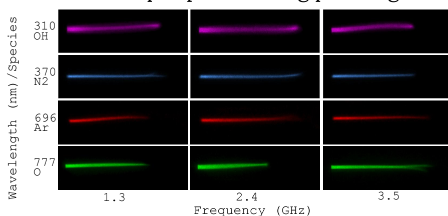

Figure 5.14: Different spectral components of a pure argon plasma at 310, 370, 696 and 777 nm using a constant input power of 10 W. Photographs are taken with a band-pass dichroic filter at each wavelength.

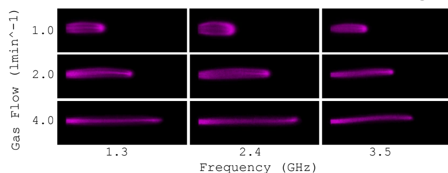

Figure 5.15: Frequency- and gas-flow-dependent behavior of a pure argon plasma from 1.3 GHz to 3.5 GHz and flows from 1 L min^{-1} to 4 L min^{-1} at the OH-band around 310 nm.

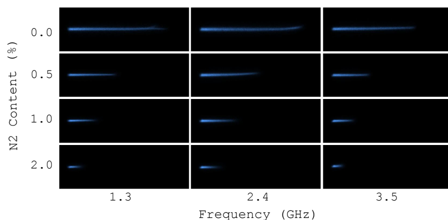

Figure 5.16: Dependency of the gas-mixture of argon and nitrogen at different frequencies and a constant gas-flow of 4 L min^{-1}. Percentage of nitrogen added to the plasma is indicated on the left side.

beginning of the plasma at the electrode. This area is also visible for the lower gas flows.
Another increase of the flow to $4\,\mathrm{L\,min^{-1}}$ leads to an increase of the horizontal size. At this gas flow, the vertical extent is the smallest, too. The brightness of the area at the end of the plasma is decreased but the core of the plasma is now more pronounced.
Fig. 5.16 displays the comparison of an argon-nitrogen mixture with an N2 content of 0.0% to 2.0% at frequencies from 1.3 GHz to 3.5 GHz. All pictures are taken using an input power of 10 W and a gas flow of $4\,\mathrm{L\,min^{-1}}$. The amount of argon and nitrogen has been adjusted for all relative compositions.
The longest elongation of the plasma is measured for pure argon. Vertical extension of the plasma is almost constant across all swept measurement parameters. Increasing the nitrogen percentage in the mixture leads to a reduction of the horizontal extent. The frequency-dependent reduction of the plasma size is also apparent for all combination of argon and nitrogen. Areas of higher light intensity are visible at the tip of the electrode where the electrical field is the highest. The brightness of this area increases with the decrease of the plasma size. Size is decreased with an of both frequency and nitrogen amount.
Size reduction of pure argon is mainly caused among other things by the lower wavelengths at higher frequencies ([116]). An ionization energy level of $1502.8\,\mathrm{kJ\,mol^{-1}}$ is required for pure argon. A single nitrogen atom has an ionization level of $1402.3\,\mathrm{kJ\,mol^{-1}}$ but this element mainly exists as dinitrogen (N_2). An additional energy amount of $945\,\mathrm{kJ\,mol^{-1}}$ is needed as bond-dissociation energy. Therefore the size of the plasma is reduced.
To counteract this effect, the input power signal could be superimposed by a modulated signal to improve the mixing of the gas. This has been presented in [32]. The efficacy of the lamp was improved by superimposing an amplitude modulated signal. More details on this can be found in [36]. Further investigations are therefore planned to characterize possible influences of a modulated signal on the frequency-dependence of a plasma and the gas mixture.

5.3.2 Frequency Dependency of the PC-Lamp's Optical Properties

Investigation on the differences of the optical properties is important for lighting applications since it is the main purpose of this type of plasma. In this section, the frequency-dependent optical properties of the PC-Lamp are presented.

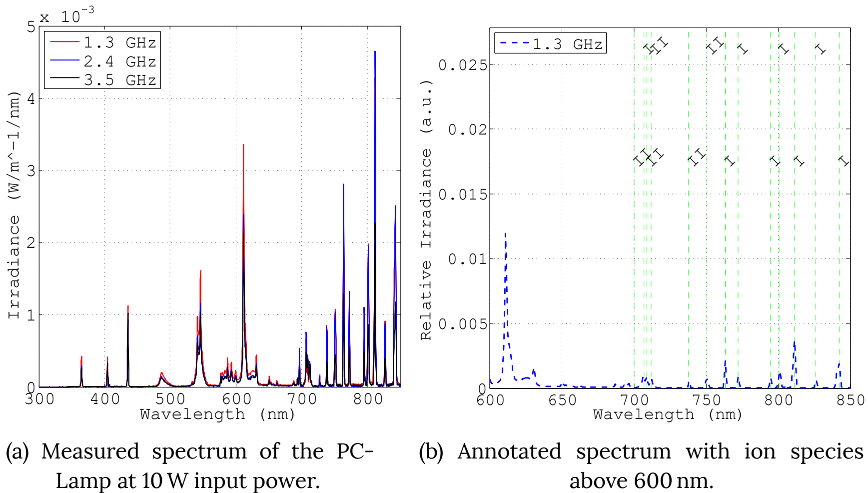

(a) Measured spectrum of the PC-Lamp at 10 W input power.

(b) Annotated spectrum with ion species above 600 nm.

Figure 5.17: Spectrum and annotated spectrum at 10 W input power.

The typical spectrum of the PC-Lamp can be found in Fig. 5.17a. Most spectral lines are located in the visible area from 380 nm to 780 nm with an additional continuum around 600 nm. Parts of the energy are lost in radiation above 780 nm, but can be utilized to determine the ion species of the contained argon and mercury. The spectrum is generated by a phosphor coating on the inside of the lamp. This coating is used to convert the UV-spectrum of the mercury into the visible area above 380 nm. More information about the conversion process from UV-light using phosphor coatings can be found in [123]. The different spectra exhibit changes in all parts of the spectrum. Lowering the frequency increases the peaks of the spectra. At lower power levels the absolute values are lower with comparable changes of the spectral values.

Phosphor coatings cannot convert all wavelength into visible light. Close to the infrared spectrum (near-IR, NIR[3]) spectral lines of the plasma are able to pass through the coating and thus be detected. Therefore only the spectral lines close to the IR range have been annotated in Fig. 5.17b for mercury, which is the main generator of spectral lines inside the PC-Lamp. In this plot single ionized ions including some HgII ions are visible.

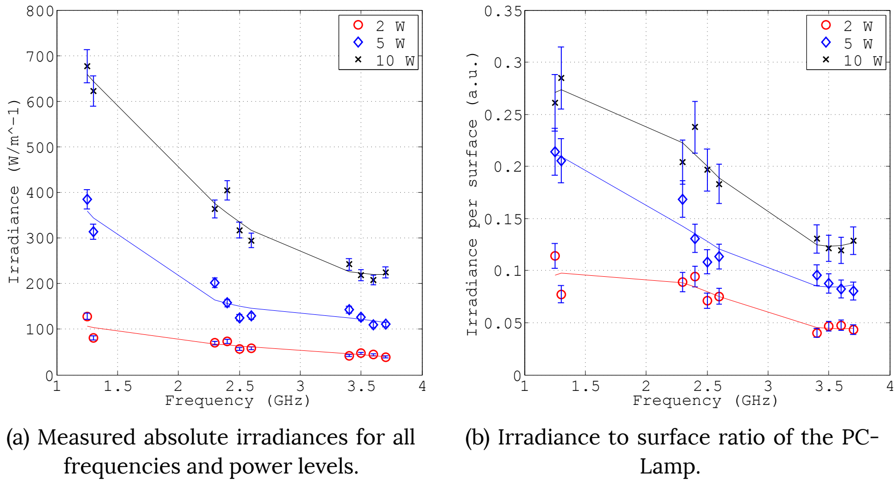

(a) Measured absolute irradiances for all frequencies and power levels.

(b) Irradiance to surface ratio of the PC-Lamp.

Figure 5.18: Comparison of optical measurement results for the PC-Lamp.

To compare the absolute irradiances, the measured results are plotted in Fig. 5.18a. At 1.3 GHz the highest values for all power levels are recorded. When switching the frequency to the 2.4 GHz band, the relative decrease is about 15%. By another increase to the band around 3.5 GHz another drop of around 20% compared to the frequencies around 2.4 GHz becomes visible.
As an indicator of the efficacy of the lamp, the irradiance output of the lamp normalized by the plasma size is calculated. It should identify possible influences of the chosen frequency on the efficacy of the lamp. A comparison of all frequencies and power levels is presented in Fig. 5.18b. The bands at 1.3 and 2.4 GHz exhibit an almost equal efficacy for all power levels. At 3.5 GHz the efficacy is slightly decreased

[3] The infrared spectrum starts at about 780 nm

by about 20% for a power level of 10 W. At lower power levels at this frequency, the efficacy is comparable to the lower bands.
The ratio of the irradiance and the surface show a better performance of the lamp at lower frequencies. Since the lamp is the biggest DUT in this thesis, the bigger spatial expansions of the lower frequencies are favored. By scaling the lamp to a smaller size, the efficacy at higher frequencies would increase.

5.3.3 Frequency Dependency of the Xenon Hollow Cylinder's Optical Properties

In this section, the frequency-dependent optical properties of the XHC prototype are analyzed. In contrast to the jet and the PC-Lamp, xenon is used as the plasma gas.

For the determination of the XHC's optical properties, the sampling time has to be increased since the optical output is lower compared to the PC-Lamp.

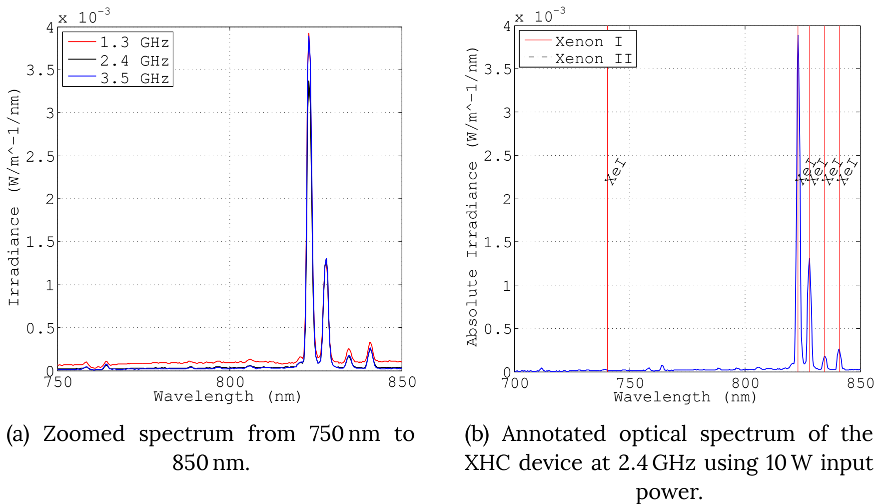

(a) Zoomed spectrum from 750 nm to 850 nm.

(b) Annotated optical spectrum of the XHC device at 2.4 GHz using 10 W input power.

Figure 5.19: Spectra at different frequencies and spectrum with annotated ion species for the XHC.

The resulting zoomed optical spectra from 750 nm to 850 nm are shown in Fig. 5.19a using an input power of 10 W.

Most of the spectral lines are developed above 750 nm with an increased output at lower frequencies. The most prominent lines are located around 830 nm. All spectra exhibit a low-pressure spectra with single spectral lines and no continuum. At 1.3 GHz the highest peaks are recorded, followed by 2.4 and 3.5 GHz with a relative change of 15% from 1.3 GHz to 2.4 GHz and 29.5% from 1.3 GHz to 3.5 GHz.

Only single ionized ions are visible on the spectrum as visualized in Fig. 5.19b. This indicates a low energy level of the xenon ions, which is also visible by the low irradiance of the device itself.

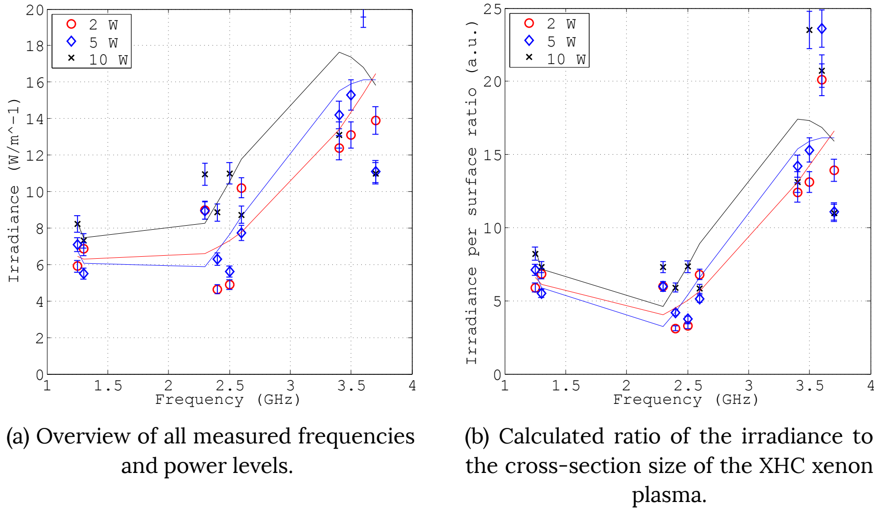

(a) Overview of all measured frequencies and power levels.

(b) Calculated ratio of the irradiance to the cross-section size of the XHC xenon plasma.

Figure 5.20: Irradiance and irradiance per surface ratio.

Irradiance is calculated from the measured spectra. A comparison of all data at all measured power levels and frequencies is shown in Fig. 5.20a. Again the highest peaks are located in the 1.3 GHz band. Since the recorded results exhibit a variation in which the power levels overlap, no proportional factor can be calculated. This is caused by the interference pattern inside the XHC burner. For all bands, the illuminances vary from 4 to a maximum of 14. Fig. 5.9 shows a possible reason for the higher optical output at 3.5 GHz since the amount of more intense light output increases with the frequency.

Combining the spectral measurements shows no proportional factor for different frequencies. In Fig. 5.20b the ratio of the optical output and the size of the plasma is plotted. As described in Sec. 5.2.3, the volume of the XHC is too small to allow any size comparison at input power levels above 2 W. At higher input power levels the electro-magnetic wave is reflected at the end of the volume resulting in an interference pattern, which depends on the size of the plasma itself. At 1.3 and

2.4 GHz the ratio of irradiance to the surface is almost constant. At 3.5 GHz it is nearly tripled at the same input power.

5.3.4 Summary of the Optical Properties Measurements

In this section, the frequency dependency of the optical properties for microwave plasma has been investigated and analyzed.
For all three devices under test, a dependency on the frequency has been observed. Like the spatial properties, the optical outputs are inversely proportional to the frequency and proportional to the power. To determine possible changes of the efficacy the optical outputs are normalized by the calculated spatial expansion of the plasma. For all devices an almost constant ratio resulting in a constant efficacy for all of the plasmas.
Optical emission spectroscopy measurements have been conducted for the plasma jet to show on single spectral areas. A monochromator in combination with dichroic has been used to measure the spectral lines of OH, N2, Ar, and N2. The influence of the gas mixture has been investigated. All spectral lines exhibit a frequency-dependent behavior.
All measurements and analysis in this section have been made during the work on this thesis.

5.4 Frequency Dependence of Microwave Plasma Thermal Properties

In this section, the thermal properties of microwave plasma are analyzed concerning their frequency-dependent characteristics.
It is important to know how the different frequencies influence the temperature, because of the different applications of the plasma. A plasma jet used as a cutting tool requires a higher temperature than a jet that is used for disinfecting human tissue. Other applications such as lamps benefit from different temperatures. For example, a lower electrode temperature in high pressured lamps is desired to prolong the lifetime. The work of [38] presents a new capacitively coupled microwave excited diffuse mode that profits from a lower electrode temperature. Thermal measurements of a microwave plasma in the GHz-region can be found in [124], [125] and [126].
The emission coefficient has to be set according to the material to measure the absolute temperature. This coefficient describes how much thermal radiation a body is emitting compared to an ideal thermal radiator. The emission coefficient of the camera was set to 0.72, corresponding to the emission of a copper surface at a temperature of 1000 K. For the enclosed plasma source the emission coefficient is set to 0.97, the coefficient of quartz glass.
Thermal properties are an indicator of how much power is coupled into the plasma. Thermal cameras make use of wavelengths in the infrared region to measure the temperature of an object. As explained in Section 5.1.2 none of the investigated plasma emits energy in the infrared area of the infrared camera.
There are several possibilities to determine the temperature of the plasma such as the Boltzmann plot method. It allows the calculation of plasma pressure and temperature using the emission coefficients of the process gas. These calibrated emission factors are available through the NIST atomic database. In [127] the Boltzmann method is described to determine the plasma properties of a high-pressure xenon lamp in an iterative way. The rotational temperature of the plasma jet is determined using optical emission spectroscopy of the hydroxyl line at 310 nm. For all other devices, the FLIR camera was the only measuring device, that could detect spectral data in the desired wavelength. This camera is not able to output discrete values at wavelengths necessary for the Boltzmann method.

Another approach makes use of a type K thermocouple, which would be positioned inside the plasma. Due to the small expansion of the plasma, it is not possible to measure the plasma's temperature. It is because of the interaction of the probe and the plasma, which would result in a distortion of the measurement. Former experiments showed a deviation when a metallic object is moved near the plasma torch. Moving a thermocouple into the enclosed plasma sources is also not possible. Another approach is to use a millimeter wave interferometer, which is explained in [128].
The systematic error of this measurement method[4] is determined by the inaccuracy of the camera itself, which is $\pm$ 2%.
All the measurements have been made during the works on this thesis.

[4]Thermal measurements using an IR-camera to monitor the surface contacting the plasma.

5.4.1 Frequency-Dependent Thermal Properties of the Plasma Jet

For a relative comparison of the thermal effects caused by the different powers and frequencies, the surface temperature of the inner conductor is measured. Since the power levels and gas flow for operating the plasma are absolute for each measurement, a direct comparison of the measurements is possible.
In addition the rotational temperature of the plasma jet at different frequencies and power levels is determined by fitting the OH line at 310 nm using the Boltzmann plot.

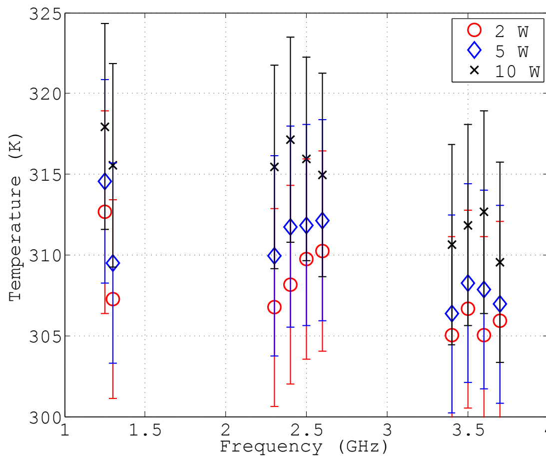

Figure 5.21: Recorded temperature of the jet's inner brass conductor for all measured frequencies and power levels.

Results of the jet's inner conductor temperature are plotted in Fig. 5.21. The thermal stress of the electrode is relatively low, with a maximum temperature of 318 K at 1.3 GHz and 10 W. By increasing the frequency to 3.7 GHz at the same level the temperature is reduced by about 8 K. This change in the thermal stress may be caused by the reduced plasma size at the higher frequencies. The smaller plasma exhibits a decreased thermal load and thus leading to lower temperatures. The thermal stress of the inner electrode for each power level and frequency are recorded at 298 K room temperature.

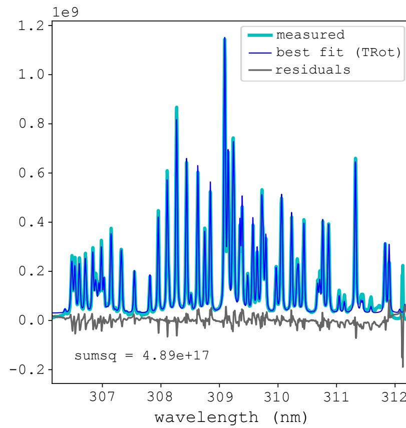

Figure 5.22: Measured and fitted OH-band around 310 nm to determine the rotational temperature T_{Rot}. Residuals display the difference between the measured and the fitted results.

By taking the measuring accuracy into account, an overlap of the power levels is visible. The measured values are too close to show a significant influence of the frequency or the power level. Therefore the only common property is the low thermal stress on the electrode. In addition the surface of the electrode is also cooled via the mass current of the argon.
Since the temperature is at about room temperature, most of the energy is coupled into the plasma, and the losses of the jet can be neglected.

5.4.1.1 Frequency-Dependence of the Rotational Temperature of the Plasma Jet

This sub-section describes the determination of the rotational temperature based on a fitting for the OH-band around 310 nm.
Fig. 5.22 the comparison of the measured spectra from 306 nm to 312 nm is plotted along with the fitted result for the rotational temperature T_{Rot}. This spectrum is recorded at 2.4 GHz and an input power of 10 W. Difference of the measurement to the fitting is presented, too. A maximum absolute different 0.2×10^9. The relative error across the whole band is about 3%. As mentioned above the accumulated measuring error is about 5% resulting in a combined relative error of 8% for the determination of the temperature.

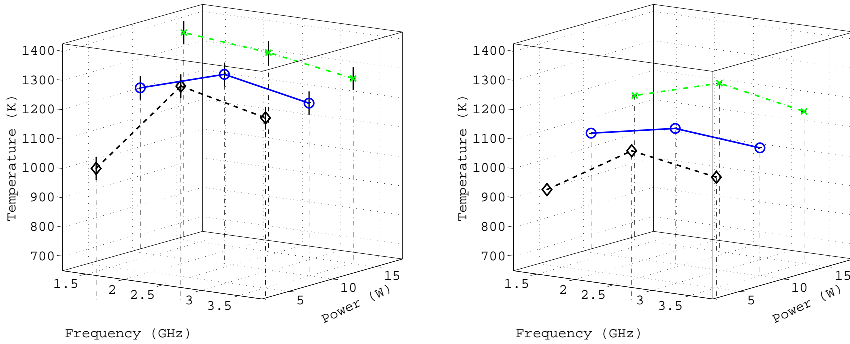

Figure 5.23: Fitted temperature for frequencies from 1.3 GHz to 3.5 GHz and input powers from 5 W to 15 W for a constant pure argon gas flow. Upper plot shows the results for a gas flow of $2\,\mathrm{L\,min^{-1}}$, the lower plot for $4\,\mathrm{L\,min^{-1}}$. Measuring accuracy of the input power is within a 5% window.

In Fig. 5.23 the determined rotational temperature at frequencies from 1.3 GHz to 3.5 GHz and power levels from 5 W to 15 W are presented. A constant gas flow of $2\,\mathrm{L\,min^{-1}}$ is plotted in the upper image, while the lower figure displays the results for a gas flow of $4\,\mathrm{L\,min^{-1}}$.
At 1.3 GHz and 15 W of input power, the maximum temperature of 1350 K is recorded. For both pictures the temperature increased with the input power. Temperature does not show a monotonic connection to the frequency.
Within the relative measuring accuracy of 8% a slight increase of the temperature towards higher frequencies is visible at the higher gas flow. A lower gas flow shows the reverse effect.
Higher temperatures are measured for the lower gas flow. This is due to the higher convection cooling by which the plasma is cooled down. At $4\,\mathrm{L\,min^{-1}}$ the temperatures are reduced by about 100 K.
The almost constant rotational temperature for a constant gas flow supports the assumption of a higher energy density at higher frequencies. This assumption is made in [116] and was based on the observation, that the size of the plasma decreases with frequency as well as the illuminance. The illuminance was normalized to the spatial extension of the plasma and it showed an almost constant ratio.

5.4.2 Frequency Dependency of the PC-Lamp's Thermal Properties

In a PC-Lamp, the mercury or an amalgam containing mercury require a minimum temperature for an efficient operation. This temperature is usually located around 370 K, but may not exceed 450 K due to the chemical resistance of the illuminants. Since the plasma of the PC-Lamp is maintained in an enclosed environment, the temperature can be read indirectly by the heating of the glass. To compare the different temperatures a settling period of about 5 min is applied before each thermal measurement.

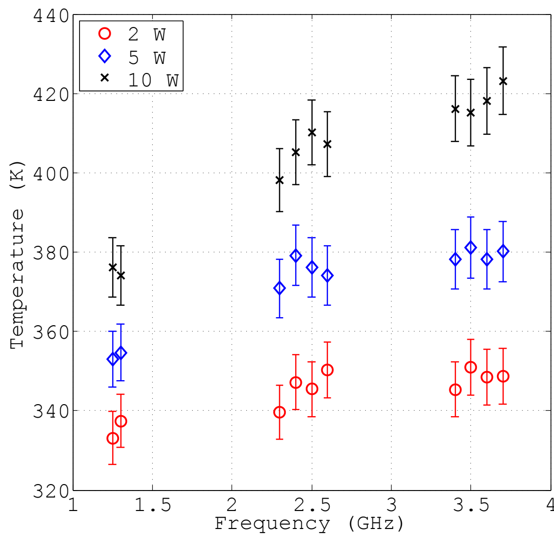

Figure 5.24: Comparison of the PC-Lamp glass surface temperature from 1.3 GHz to 3.5 GHz at power levels from 2 W to 10 W.

In Fig. 5.24 the comparison of all power levels and frequencies is visualized. The plot displays the maximum surface temperature of the glass. Temperature is proportional to both frequency and power. By changing the frequency from 1.3 GHz to 2.4 GHz the absolute temperature rises by 40 K. Another increase from 2.4 GHz to 3.5 GHz increases the temperature by 20 K. Within the frequency bands, the relative variance of the maximum temperature is less than 5 %. One reason for the increased temperatures is the spatial dimension which is described in Sec. 5.2.2. In

combination with the higher total temperature, an increase in the energy density towards higher frequencies is shown.
Regarding power, the indicated error bars show significant differences for temperatures above 2 W. At lower frequencies, the significance also exists, while at 2.4 GHz and 3.5 GHz the measuring accuracies overlap each other. But a general trend to a higher maximum temperature at higher frequencies is visible.
The surface size is reduced by an increase in the frequency. An increase in the temperature at higher frequencies shows, that the energy density is increased at higher frequencies. The same energy is coupled into the plasma but requires less space.

5.4.3 Frequency-Dependent Thermal Properties of the XHC

The XHC probe's temperature is also measured indirectly by recording the glass surface temperature. It exhibits a raise of the temperature with increased frequency.

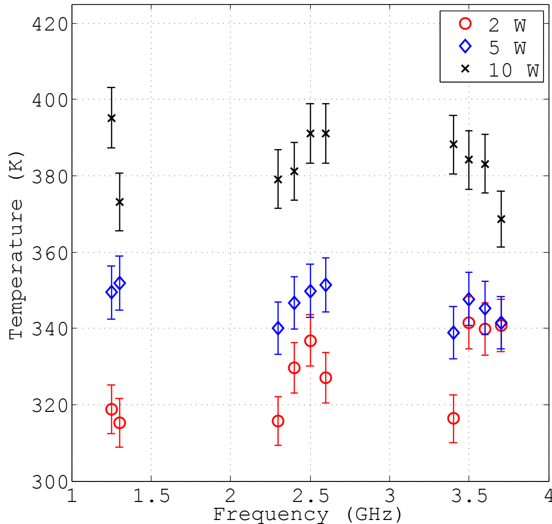

Figure 5.25: Temperature of the XHC device for all frequencies and power levels ranging from 320 K to 390 K.

As plotted in Fig. 5.25, the temperature is constant for each power level across the measured frequency spectrum, even by taking the error of the thermal camera into account. At 2 W the temperature differs from 320 K to 340 K, reaches values between 340 K to 360 K for 5 W and exhibits the highest values of 375 K to 395 K for 10 W. No proportional relative increase is measured so that the temperature within the system (plasma and network) is almost constant.
Compared to the PC-Lamp the temperature is linear for almost all power levels. Therefore the vaporized metal inside the PC-Lamp is causing more thermal stress on the glass. A higher temperature indicates a higher pressure inside the burner. By only using a single gas the pressure and the resulting temperature inside the device stay constant.

5.4.4 Summary of the Frequency-Dependent Thermal Measurement Results

In this section, the frequency-dependent thermal properties of three different microwave plasma sources have been investigated and analyzed.
It is shown, that the thermal stress on the plasma jet's electrode is low, indicating that most of the power is coupled into the plasma. This shows again the low losses of the coaxial networks.
Temperature of the phosphor-coated lamp is proportional to the frequency and power. Taking into account, that the spatial extension of the plasma is reduced at higher frequencies, the energy density increases with the frequency. Along with the observation, that the efficacy of the lamp is not reduced at higher frequencies this adds the possibilities to use higher frequencies for smaller lamps. Since the energy density is proportional to the frequency, higher frequencies are more recommended for smaller plasma lighting applications. A bigger size correlates with the usage of a lower frequency.
For the XHC no direct connection between the temperature and the frequency can be found. As expected the temperature is proportional to the input power.
In addition, the rotational temperature of the atmospheric pressure plasma jet using different process gases has been presented. Temperature of up to 1350 K hass been fitted to the measurements using the OH line at 310 nm. An increased gas flow cools the microwave plasma by about 150 K.
These first of this kind of measurements were made during this thesis.

5.5 Discussion of the Measurement Results

In this chapter, the spatial, optical and thermal properties of different microwave plasmas at various frequencies and power up to 15 W are investigated.
Using the custom written image registration routine in Matlab, the spatial properties of the different frequencies and power levels are analyzed and a significant change of the size is observed. The size is inversely proportional to the frequency, which means that the size is reduced at higher frequencies at the same power level. This behavior is caused by the change of the wavelength, which has been explained in Chapter 2. Relative changes of the size converge to the relative wavelength change.
A proportionality of the size and the power is observed resulting in an increase of the plasma size at higher input power levels. The energy level in the plasma is raised along with the power and thus generating more free charge carriers. This leads to an increase of the geometrical expansion. Comparisons of different sizes reveal that it is possible to achieve the same plasma size with a lower power at lower frequency, too.
Optical measurements have been conducted to analyze the involving species of the plasma. Spectral data are recorded and the involved ion species are determined. A maximum ionization level of three is recorded for the argon plasma of the jet. A significant frequency dependence of the optical properties is discovered. The amount of light output is proportional to the frequency. By normalizing the light output to the size of the plasma a constant ratio is found for the jet and the PC-Lamp.
An in-depth analysis of the jet's spectral properties using OES is presented including a visualization of the frequency dependence of the several spectral lines. The dependency on the gas flow, power and gas mixture has been analyzed, too. It is shown, that the frequency dependence persists for all variations.
For the thermal measurements, the amount and species of the ions is necessary, since the plasma could emit spectral lines inside the thermal cameras detector range. Since all ionization levels are below the ions emitting in the area of interest, the thermal measurements are not disturbed. No real changes of the temperatures are recorded for the jet. Significant changes are caused by the frequency and the power of the PC-Lamp. At input power levels above 5 W the temperature of the PC-Lamp increases to its highest values at 3.5 GHz and 10 W. The XHC shows a constant temperature over the frequency.

Rotational temperature of the plasma jet is fitted based on measurements using the OH line at 310 nm. Results are fitted and values of up 1350 K as well as a strong dependence on the frequency are discovered.
These results show a significant influence of the frequency on the size. In combination with the optical and thermal measurements, a constant normalized light output is calculated. The same power is coupled into the plasma at each frequency. Therefore the energy density of the plasma is increased at higher frequencies, which is supported by the thermal measurements The measurements and analyses presented in this chapter were all made during the work on this thesis and are the first of their kind.

Chapter 6

Conclusion

In this thesis the frequency-dependence of multi-physical microwave plasma properties has been investigated and analyzed.
For the first time the development workflow of bi-static networks for two electrode-less high-pressure lamps is presented. The main states of plasmas have been explained in detail along with the requirements for each of the states for the RF-network design. The electrode-less UV-Lamp has achieved high-pressure using a custom-built design, while the domestic high-pressure lamp has exhibited an efficacy of 135 $\mathrm{lm\,W^{-1}}$, which exceeds the efficacy of most of the LEDs.
The analyses of the frequency-dependent electrical effects on a plasma jet, a phosphor-coated lamp and a hollow cylinder filled with xenon have been shown. A capacitive dominated base point impedance is discovered, which has led to the introduction of a new lumped element and 3D-model for the fitting of the microwave plasma. The lumped element model consists of a lossy series resonance circuit, while the 3D-model has been capable of fitting the plasma only by the conductivity. Transmission parameters of an argon microwave plasma at atmospheric pressure have been determined and analyzed for the first time. For these measurements a single lossy capacitor has fitted the transmission values of S_{21}, while a new 3D-core/cone models has fitted the electrical and spatial properties of the plasma in the FEM simulator.

An investigation of the spatial, optical and thermal properties has been conducted for the first time. A simple CMOS camera and a custom image registration routine have revealed a significant influence of the frequency on the plasma spatial properties for all prototypes. The plasma size has been smaller at higher frequencies. In combination with the optical measurement results it has shown, that the energy has been proportional to the frequency. This has been supported by the optical emission spectroscopy measurement of the plasma jet, which has been investigated to determine the impact of the frequency on single spectral lines. Thermal properties have been analyzed along with the determination of the rotational temperature of the plasma jet and the influence of the frequency, power, gas flow and gas mixture. Temperatures of up to 1350 K are measured at only 15 W.
Summarizing the above, a strong frequency-dependence for all of the investigated multi-physical parameters has been measured and analyzed. High-pressure has been achieved for the first of its kind electrode-less UV-Lamp as well as a very good efficacy of a newly developed high-pressure lamp. New and simple lumped elements and 3D-models for the fitting of the electrical properties have been introduced and verified.
The analyses of the frequency-dependent effects have been performed in this thesis. These effects have revealed a strong dependence of the plasma properties on the frequency. Hence it has been shown, that a new degree of freedom has been added by choosing the frequency based on the application needs. This has been supported by the multi-physical investigations.

Bibliography

[1] S. Reif-Acherman, “Heinrich Geissler: Pioneer Of Electrical Science and Vacuum Technology [Scanning our Past],” Proc. IEEE, vol. 103, pp. 1672–1684, Sept. 2015.

[2] C. Feldmann, T. Jüstel, C. R. Ronda, and P. J. Schmidt, “Inorganic Luminescent Materials: 100 Years of Research and Application,” Adv. Funct. Mater., vol. 13, pp. 511–516, July 2003.

[3] C. D. Child, Electric Arcs; Experiments Upon Arcs Between Different Electrodes in Various Environments and Their Explanation. Hardpress, 2012.

[4] W. T. Anderson, “Xenon Compact Arc Lamps*,” J. Opt. Soc. Am., vol. 41, p. 385, June 1951.

[5] A. W. Trivelpiece and R. W. Gould, “Space Charge Waves in Cylindrical Plasma Columns,” J. Appl. Phys., vol. 30, pp. 1784–1793, Nov. 1959.

[6] Z. Zakrzewski, M. Moisan, and G. Sauvé, Surface-Wave Plasma Sources. Springer, Boston, MA, 1993.

[7] B. N. Chapman, Glow Discharge Processes: Sputtering and Plasma Etching. Wiley, 1980.

[8] A. Schütze, J. Y. Jeong, S. E. Babayan, J. Park, G. S. Selwyn, and R. F. Hicks, “A Review and Comparison to Other Plasma Sources,” IEEE Trans. Plasma Sci., vol. 26, no. 6, pp. 1685–1694, 1998.

[9] H. Heuermann, S. Holtrup, A. Sadeghfam, M. Schmidt, R. Perkuhn, and T. Finger, “Various Applications and Background of 10-200 W 2 . 45 GHz Microplasmas,” IEEE MTT-S Int. Microw. Symp. Dig. 2012, pp. 10–12, 2012.

[10] C. W. Tang and K. Y. Tong, “A Compact Large Signal Model of LDMOS,” Solid. State. Electron., vol. 46, no. 12, pp. 2111–2115, 2002.

[11] U. K. Mishra, L. Shen, T. E. Kazior, and Y. F. Wu, “GaN-Based RF Power Devices and Amplifiers,” Proc. IEEE, vol. 96, pp. 287–305, Feb. 2008.

[12] C. Oeguen, C. Schopp, U. Graeser, M. Schaaf, S. Holtrup, H. Heuermann, and R. Kling, “Electrodeless Mercury-Free Low-Pressure Lamps Driven by Microwaves,” LICHT 2014, Gemeinschaftstagung, Den Haag, NL, 2014.

[13] A. D. MacDonald and H. W. Bandel, Electrical Breakdown in the Atmosphere. Rome: PN, 1962.

[14] R. Foest, M. Schmidt, and K. Becker, “Microplasmas, an Emerging Field of Low-Temperature Plasma Science and Technology,” Int. J. Mass Spectrom., vol. 248, no. 3, pp. 87–102, 2006.

[15] V. R. Schoenbach K. H. and B. W. W, “Field Controlled Plasma Discharge Device,” 1995.

[16] K. H. Becker, Non-Equilibrium Air Plasmas at Atmospheric Pressure. Institute of Physics Publishing, 2005.

[17] K. D. Weltmann, E. Kindel, R. Brandenburg, C. Meyer, R. Bussiahn, C. Wilke, and T. von Woedtke, “Atmospheric Pressure Plasma Jet for Medical Therapy: Plasma Parameters and Risk Estimation,” Contrib. to Plasma Phys., vol. 49, pp. 631–640, Nov. 2009.

[18] H. Y. Kim, S. K. Kang, S. M. Park, H. Y. Jung, B. H. Choi, J. Y. Sim, and J. K. Lee, “Characterization and Effects of Ar/Air Microwave Plasma on Wound Healing,” Plasma Process. Polym., vol. 12, pp. 1423–1434, Dec. 2015.

[19] A. I. N. Press, “Plasma Jet Treatment of ve Polymers at Atmospheric Pressure: Surface Modi Cations and the Relevance for Adhesion,” J. Adhes., vol. 24, pp. 171–177, 2004.

[20] F. Deeba, A. Qayyum, and N. Mahmood, “Optical Emission Spectroscopy of 2.45 GHz Microwave Induced Plasma,” IBIMA Publ. J. Res. Spectrosc. J. Res. Spectrosc., vol. 2015, 2015.

[21] H. Suzuki, S. Nakano, H. Itoh, M. Sekine, M. Hori, and H. Toyoda, “Characteristics of an Atmospheric-Pressure Line Plasma Excited by 2.4GHz Microwave Travelling Wave,” Jpn. J. Appl. Phys., vol. 55, p. 01AH09, Jan. 2016.

[22] A. I. Al-Shamma’a, S. R. Wylie, J. Lucas, and C. F. Pau, “Design and Construction of a 2.45 GHz Waveguide-Based Microwave Plasma Jet at Atmospheric Pressure for Material Processing,” J. Phys. D. Appl. Phys., vol. 34, no. 18, pp. 2734–2741, 2001.

[23] J. Gregório, A. R. Hoskinson, and J. Hopwood, “Modeling of Microplasmas from GHz to THz,” J. Appl. Phys., vol. 118, no. 8, 2015.

[24] H. R. Humud, Q. A. Abbas, and A. F. Rauuf, “Effect of Gas Flow Rate on the Electron Temperature, Electron Density and Gas Temperature for Atmospheric Microwave Plasma Jet,” Int. J. Curr. Eng. Technol., vol. 5, no. 6, pp. 2277–4106, 2015.

[25] R. Williams and Y. Ikeda, “Real-Time Impedance Measurement and Frequency Control in an Automotive Plasma Ignition System,” in 2015 IEEE MTT-S Int. Microw. Symp. IMS 2015, pp. 1–4, IEEE, May 2015.

[26] D. Levko and L. L. Raja, “Effect of Frequency on Microplasmas Driven by Microwave Excitation,” J. Appl. Phys., vol. 118, p. 043303, July 2015.

[27] A. Alamatsaz and A. Venkattraman, “Operating modes of field emission assisted microplasmas in the microwave regime,” J. Appl. Phys., vol. 120, p. 123305, Sept. 2016.

[28] D. Levko and L. L. Raja, “Electron Kinetics in Atmospheric-Pressure Argon and Nitrogen Microwave Microdischarges,” J. Appl. Phys., vol. 119, p. 163303, Apr. 2016.

[29] G. Dilecce, “Optical Spectroscopy Diagnostics of Discharges at Atmospheric Pressure,” Plasma Sources Sci. Technol., vol. 23, p. 015011, Feb. 2014.

[30] Z. Chen, Z. Yin, Y. Huang, O. Stepanova, S. Gutsev, and A. A. Kudryavtsev, "More Efficient Microwave Argon Plasma Jet with a Symmetric Hairpin Copper Wire at Atmospheric Pressure," IEEE Trans. Plasma Sci., vol. 43, pp. 906–907, Mar. 2015.

[31] V. G. Brovkin, A. S. Pashchina, and N. M. Ryazanskiy, "Interaction of Microwave Radiation with an Erosion Plasma Jet," Tech. Phys. Lett., vol. 42, pp. 901–904, Sept. 2016.

[32] J. Voráč, L. Potočňáková, P. Synek, J. Hnilica, and V. Kudrle, "Gas Mixing Enhanced by Power Modulations in Atmospheric Pressure Microwave Plasma Jet," Plasma Sources Sci. Technol., vol. 25, p. 025018, Apr. 2016.

[33] V. A. Godyak, "Bright Idea, Radio-Frequency Light Sources," Ind. Appl. Mag. IEEE, vol. 8, no. 3, pp. 42–49, 2002.

[34] C. Schopp and H. Heuermann, "Electrodeless Low Pressure Lamp with Bi-Static Matching at 2.45 GHz," in Eur. Microw. Conf., (Nuremberg), pp. 881–884, 2013.

[35] S. Holtrup, A. Sadeghfam, H. Heuermann, S. Member, and P. Awakowicz, "Characterization and Optimization Technique for Lamps Using Hot S-Parameters," IEEE Trans. Microw. Theory Tech., vol. 62, no. 10, pp. 2471–2480, 2014.

[36] C. Schopp, H. Heuermann, and S. Holtrup, "Investigation on Efficacy Optimization of RF-Driven Automotive D-Lamps," in Eur. Microw. Conf. 2014 Connect. Futur. EuMW 2014 - Conf. Proceedings; EuMC 2014 44th Eur. Microw. Conf., (Rome), pp. 1154–1157, IEEE, Oct. 2014.

[37] R. P. Gilliard, M. Devincentis, A. Hafidi, D. O'Hare, and G. Hollingsworth, "Operation of the LiFi light emitting plasma in resonant cavity," IEEE Trans. Plasma Sci., vol. 39, pp. 1026–1033, Apr. 2011.

[38] S. Holtrup, Untersuchung von HID-Lampen Im Mikrowellen- Und SWDC- Betrieb. PhD Thesis, Ruhr-University Bochum, Bochum, 2015.

[39] M. Lieberman and A. Lichtenberg, Discharges and Materials Processing Principles of Plasma Discharges and Materials. Wiley-Interscience, 2005.

[40] J. Xue and J. A. Hopwood, "Microwave-Frequency Effects on Microplasma," IEEE Trans. Plasma Sci., vol. 37, no. 6, pp. 816–822, 2009.

[41] A. R. Hoskinson, S. Parsons, and J. Hopwood, "Gas Breakdown and Plasma Impedance in Split-Ring Resonators," Eur. Phys. J. D, vol. 70, p. 30, Feb. 2016.

[42] S. Dennison, A. Chapman, W. Luo, M. Lanagan, and J. Hopwood, "Plasma Generation by Dielectric Resonator Arrays," Plasma Sources Sci. Technol., vol. 25, p. 03LT02, June 2016.

[43] K. McKay, F. Iza, and M. G. Kong, "Excitation Frequency Effects on Atmospheric-Pressure Helium RF Microplasmas: Plasma Density, Electron Energy and Plasma Impedance," Eur. Phys. J. D, vol. 60, no. 3, pp. 497–503, 2010.

[44] N. Miura and J. Hopwood, "Internal Structure of 0.9 GHz Microplasma," J. Appl. Phys., vol. 109, no. 11, p. 113303, 2011.

[45] K. Ohkubo and K. Matsuura, "Study on High-Frequency Breakdown in 0.8-0.9 GHz," J. Appl. Phys., vol. 17, no. 117, 1978.

[46] M. Moisan, Microwave Excited Plasmas, Plasma Technology. Elsevier, 4th ed., 1992.

[47] P. Chabert and N. Braithwaite, Physics of Radio-Frequency Plasmas. Cambridge University Press, 2011.

[48] M. Laroussi and T. Akan, "Arc-Free Atmospheric Pressure Cold Plasma Jets: A Review," Plasma Process. Polym., vol. 4, no. 9, pp. 777–788, 2007.

[49] G. G. Lister, Y.-M. Li, and V. A. Godyak, "Electrical Conductivity in High-Frequency Plasmas," J. Appl. Phys., vol. 79, no. 12, pp. 8993–8997, 1996.

[50] C. Leu, M. Birle, S. Gossel, and F. Reichert, "Determination of Electric Conductivity of Hot Argon Gas Using a High-Frequency High-Voltage Generator," 20th Int. Conf. Gas Discharges their Appl. Orleans, Fr., pp. 722–725, 2014.

[51] A. D. Macdonald, "High-Frequency Breakdown in Air at High Altitudes," Proc. IRE, vol. 47, no. 3, pp. 1070–1073, 1959.

[52] L. Baars-Hibbe, Characterization and Applications of High Frequency Discharges in the Near-Atmospheric Pressure Range Using Micro-Structured Electrode Arrays. Cuvillier, 2005.

[53] G. A. Baraff and S. J. Buchsbaum, “Anisotropic Electron Distribution and the DC and Microwave Avalanche Breakdown in Hydrogen,” Phys. Rev., vol. 130, pp. 1007–1019, May 1963.

[54] P. Flesch and M. Neiger, “Investigations on the Influence of Pressure, Current and Electrode Gap in High-Pressure Mercury Lamps,” J. Phys. D. Appl. Phys., vol. 38, pp. 3792–3803, Oct. 2005.

[55] M. Czichy, T. Hartmann, J. Mentel, and P. Awakowicz, “Ignition of Mercury-Free High Intensity Discharge Lamps,” J. Phys. D. Appl. Phys., vol. 41, no. 14, p. 144027, 2008.

[56] M. Sparks, D. L. Mills, R. Warren, T. Holstein, A. A. Maradudin, L. J. Sham, E. Loh, and D. F. King, “Theory of Electron-Avalanche Breakdown in Solids,” Phys. Rev. B, vol. 24, pp. 3519–3536, Sept. 1981.

[57] E. E. Kunhardt and Y. Tzeng, “Development of an Electron Avalanche and Its Transition into Streamers,” Phys. Rev. A, vol. 38, pp. 1410–1421, Aug. 1988.

[58] H. Kim, J. Verboncoeur, and Y. Y. Lau, “Modeling RF Window Breakdown: From Vacuum Multipactor to RF Plasma,” IEEE Trans. Dielectr. Electr. Insul., vol. 14, pp. 774–782, Aug. 2007.

[59] J. Cooper, “Plasma Spectroscopy,” Reports Prog. Phys., vol. 29, pp. 35–130, 1966.

[60] H. Griem, Spectral Line Broadening by Plasmas. Elsevier Science, 1974.

[61] A. Kramida, Y. Ralchenko, J. Reader, and N. A. Team, NIST Atomic Spectra Database Lines Form. NIST, 2014.

[62] N. Britun, M. Gaillard, A. Ricard, Y. M. Kim, K. S. Kim, and J. G. Han, “Determination of the Vibrational, Rotational and Electron Temperatures in N2 and Ar–N2 RF Discharge,” J. Phys. D. Appl. Phys., vol. 40, pp. 1022–1029, Feb. 2007.

[63] N. Britun, T. Minea, S. Konstantinidis, and R. Snyders, "Plasma Diagnostics for Understanding the Plasma–Surface Interaction in HiPIMS Discharges: A Review," J. Phys. D. Appl. Phys., vol. 47, p. 224001, June 2014.

[64] J. Janča, L. Skrřička, and A. Brablec, "Simple and Quick Rotational Temperature Determination in N2-Containing Discharge Plasma," Plasma Chem. Plasma Process., vol. 13, pp. 567–577, Sept. 1993.

[65] J. R. Meyer-Arendt, "Radiometry and Photometry: Units and Conversion Factors," Appl. Opt., vol. 7, no. 10, pp. 2081–2084, 1968.

[66] Optical Society of America, Handbook of Optics. McGraw-Hill, 2004.

[67] C. DeCusatis and Optical Society of America, Handbook of Applied Photometry. AIP Press, 1997.

[68] H. Heuermann, Hochfrequenztechnik. Vieweg Verlag, second ed., 2009.

[69] T. C. Edwards and M. B. Steer, "Appendix A: Transmission Line Theory," in Found. Interconnect Microstrip Des., pp. 435–447, West Sussex, England: John Wiley {&} Sons, Ltd, Dec. 2013.

[70] J. Detlefsen and U. Siart, Grundlagen Der Hochfrequenztechnik, vol. 49. Oldenbourg, 2012.

[71] K. Simonyi, Theoretische Elektrotechnik : Mit 12 Tabellen. Barth, Ed. Dt. Verl. der Wiss, 1993.

[72] H. G. Booker, "The Elements of Wave Propagation Using the Impedance Concept," Electr. Eng. - Part III Radio Commun. Eng. J. Inst., vol. 94, pp. 171–198, May 1947.

[73] R. F. Bauer and P. Penfield, "De-Embedding and Unterminating," IEEE Trans. Microw. Theory Tech., vol. 22, no. 3, pp. 282–288, 1974.

[74] W. Rotman, "Plasma Simulation by Artificial Dielectrics and Parallel-Plate Media," IRE Trans. Antennas Propag., vol. 10, pp. 82–95, Jan. 1962.

[75] J. Brown, "Artificial Dielectrics Having Refractive Indices Less Than Unity," Proc. IEE - Part IV Inst. Monogr., vol. 100, pp. 51–62, Oct. 1953.

[76] A. Ghayekhloo and A. Abdolali, “Use of Collisional Plasma as an Optimum Lossy Dielectric for Wave Absorption in Planar Layers, Analysis, and Application,” IEEE Trans. Plasma Sci., vol. 42, pp. 1999–2006, Aug. 2014.

[77] M. A. M. A. . Lieberman and A. J. Lichtenberg, Principles of Plasma Discharges and Materials Processing. Wiley-Interscience, 2005.

[78] P. Chabert, “Electromagnetic Effects in High-Frequency Capacitive Discharges Used for Plasma Processing,” J. Phys. D. Appl. Phys., vol. 40, pp. R63–R73, Feb. 2007.

[79] K. D. Paulsen, D. R. Lynch, and J. W. Strahbehn, “Three-Dimensional Finite, Boundary, and Hybrid Element Solutions of the Maxwell Equations for Lossy Dielectric Media,” IEEE Trans. Microw. Theory Tech., vol. 36, pp. 682–693, Apr. 1988.

[80] S. Holtrup and H. Heuermann, “Fundamentals and Ignition of a Microplasma at 2.45 GHz,” Eur. Microw. Week 2009, pp. 1607–1609, 2009.

[81] T. Gasseling, D. Barataud, S. Mons, J. M. Nebus, J. P. Villotte, J. J. Obregon, and R. Quere, “Hot Small-Signal S-Parameter Measurements of Power Transistors Operating Under Large-Signal Conditions in a Load-Pull Environment for the Study of Nonlinear Parametric Interactions,” IEEE Trans. Microw. Theory Tech., vol. 52, no. 3, pp. 805–812, 2004.

[82] J. P. Dunsmore, Handbook of Microwave Component Measurements: With Advanced VNA Techniques. John Wiley & Sons, 2012.

[83] H. Heuermann and T. Finger, “2.45 GHz Plasma Powered Spark Plug by Thermal and EM-Optimization,” Ansys High Freq. Simul. Conf., 2014.

[84] H. Heuermann and A. Sadeghfam, “Analog Amplitude-Locked Loop Circuit to Support RF Energy Solutions,” in IEEE MTT-S Int. Microw. Symp. Dig., vol. 2016-Augus, pp. 1–4, IEEE, May 2016.

[85] T. J. Moir, “Analysis of an Amplitude-Locked Loop,” Electron. Lett., vol. 31, no. 9, p. 694, 1995.

[86] J. C. Biswas and V. Mitra, “High-Frequency Breakdown and Paschen Law,” Appl. Phys., vol. 19, pp. 377–381, Aug. 1979.

[87] J. Park, I. Henins, H. W. Herrmann, and G. S. Selwyn, "Gas Breakdown in an Atmospheric Pressure Radio-Frequency Capacitive Plasma Source," J. Appl. Phys., vol. 89, no. 1, pp. 15–19, 2001.

[88] A. Semnani, A. Venkattraman, A. A. Alexeenko, and D. Peroulis, "Frequency Response of Atmospheric Pressure Gas Breakdown in Micro/Nanogaps," Appl. Phys. Lett., vol. 103, no. 6, p. 063102, 2013.

[89] A. Grebennikov, "High-Efficiency Class E/F Lumped and Transmission-Line Power Amplifiers," IEEE Trans. Microw. Theory Tech., vol. 59, no. 6, pp. 1579–1588, 2011.

[90] W. J. Bell, "Proposed Model of Thermionically Assisted Breakdown and Implementation on Electrostatic Thrusters," Tech. Rep. US Naval Academy, Naval Postgraduate School, Monterey, California, 1991.

[91] W. M. Haynes, D. R. Lide, and T. J. Bruno, CRC Handbook of Chemistry and Physics: A Ready-Reference Book of Chemical and Physical Data. CRC Press, 1995.

[92] N. Marchand, "Transmission-Line Conversion Transformers," Electronics, vol. 17, pp. 142–145, 1944.

[93] J. H. Cloethe, "Graphs of Circuit Elements for the Marchand Balun," Microw. Journal, vol. 24, no. 5, pp. 125–128, 1981.

[94] S. Offermanns, "Electrodeless High-Pressure Microwave Discharges," J. Appl. Phys., vol. 67, no. 1, pp. 115–123, 1990.

[95] G.-S. Choi, Y.-S. Choi, J.-C. Lee, and D.-H. Park, "The Study on Discharge Characteristic in Mercury and Electrode Free Lamp by Spectrum Analysis," in 33rd IEEE Int. Conf. Plasma Sci. 2006. ICOPS 2006. IEEE Conf. Rec. - Abstr., pp. 123–123, 2006.

[96] D. O. Wharmby, "Electrodeless Lamps for Lighting: A Review," IEE Proc. A Sci. Meas. Technol., vol. 140, no. 6, p. 465, 1993.

[97] S. Kobayashi and A. Hatano, "High-Intensity Low-pressure Electrodeless Mercury-Argon Lamp for UV Disinfection of Wastewater," Environment, vol. 3, no. 1, pp. 71–76, 2005.

[98] M. Laroussi, Electrodeless Excimer UV Lamp. Old Dominion University Research Foundation, 2002.

[99] C. Ferrari, I. Longo, L. Socci, and M. Cavagnaro, "Coaxially Driven Microwave Electrodeless UVLamp," J. Electromagn. Waves Appl., vol. 28, no. 6, pp. 669–684, 2014.

[100] C. Schopp, T. Doll, U. Graeser, T. Harzheim, H. Heuermann, R. Kling, and M. Marso, "Capacitively Coupled High-Pressure Lamp Using Coaxial Line Networks," IEEE Trans. Microw. Theory Tech., vol. 64, pp. 3363–3368, Oct. 2016.

[101] M. Kando, T. Fukaya, Y. Ohishi, T. Mizojiri, Y. Morimoto, M. Shido, and T. Serita, "Application of an Antenna Excited High Pressure Microwave Discharge to Compact Discharge Lamps," J. Phys. D. Appl. Phys., vol. 41, p. 144026, July 2008.

[102] J. Voráč, J. Hnilica, V. Kudrle, and P. Dvořák, "Spatially Resolved Measurement of Hydroxyl (OH) Radical Concentration in a Microwave Plasma Jet by Planar Laser-Induced Fluorescence," Plasma Sources Sci. Technol., vol. 13, Jan. 2014.

[103] G. Derra, H. Moench, E. Fischer, H. Giese, U. Hechtfischer, G. Heusler, A. Koerber, U. Niemann, F.-C. Noertemann, P. Pekarski, J. Pollmann-Retsch, A. Ritz, and U. Weichmann, "Uhp Lamp Systems for Projection Applications," J. Phys. D. Appl. Phys., vol. 38, pp. 2995–3010, Sept. 2005.

[104] R. Heinz and Schulz, Grundlagen der Lichterzeugung von der Glühlampe bis zum Laser. Highlight Verlagsgesellschaft, 2014.

[105] M. L. Huber, A. R. Laesecke, and D. G. Friend, "The Vapor Pressure of Mercury," NIST Interagency/Internal Rep. - 6643, 2006.

[106] O. V. Mazurin, "Problems of Compatibility of the Values of Glass Transition Temperatures Published in the World Literature," Glas. Phys. Chem., vol. 33, pp. 22–36, Feb. 2007.

[107] J. G. Speight, N. York, C. San, F. Lisbon, L. Madrid, M. City, M. New, D. San, J. S. Singapore, and S. Toronto, Lange's Handbook of Chemistry. McGraw-Hill Inc., 1999.

[108] E. J. Wilkinson, “An N-Way Hybrid Power Divider,” IEEE Trans. Microw. Theory Tech., vol. 8, pp. 116–118, Jan. 1960.

[109] K. Kurokawa, “Design Theory of Balanced Transistor Amplifiers,” Bell Syst. Tech. J., vol. 44, pp. 1675–1698, Oct. 1965.

[110] J. L. Dawson, “Power Amplifier Linearization Techniques: An Overview,” Work. RF Circuits 2.5G 3G Wirel. Syst., p. 200, 2001.

[111] H.-J. Eul and B. Schiek, “A Generalized Theory and New Calibration Procedures for Network Analyzer Self-Calibration,” IEEE Trans. Microw. Theory Tech., vol. 39, pp. 724–731, Apr. 1991.

[112] G. Matthaei, L. Young, and E. M. T. Jones, Microwave Filters, Impedance-Matching Networks, and Coupling Structures, vol. 1964. Artech House Books, 1980.

[113] H. Heuermann, “Calibration of a Network Analyzer without a Thru Connection for Nonlinear and Multiport Measurements,” IEEE Trans. Microw. Theory Tech., vol. 56, pp. 2505–2510, Nov. 2008.

[114] C. Schopp, F. Nachtrodt, H. Heuermann, U. W. Scherer, D. Mostacci, T. Finger, and W. Tietsch, “A Novel 2.45 GHz/200 W Microwave Plasma Jet for High Temperature Applications Above 3600 K,” J. Phys. Conf. Ser., vol. 406, p. 012029, 2012.

[115] A. Stephan, H. Heuermann, and M. Prantner, “Cutting Human Tissue with Novel Atmospheric-Pressure Microwave Plasma Jet,” in 2016 46th Eur. Microw. Conf., pp. 902–905, IEEE, Oct. 2016.

[116] C. Schopp, H. Heuermann, and M. Marso, “Multi-Physical Study of an Atmospheric Microwave Argon Plasma Jet,” IEEE Trans. Plasma Sci., vol. 45, no. 6, pp. 932–937, 2017.

[117] A. Ferrero and U. Pisani, “Two-Port Network Analyzer Calibration Using an Unknown ’Thru’,” IEEE Microw. Guid. Wave Lett., vol. 2, pp. 505–507, Dec. 1992.

[118] B. Osgood, The Fourier Transform and its Applications. McGraw Hill, 2009.

[119] D. Marr and E. Hildreth, "Theory of Edge Detection," Proc. R. Soc. London B Biol. Sci., vol. 207, no. 1167, pp. 187–217, 1980.

[120] T. Meyer and I. M. Tkachenko, "High-Frequency Electrical Conductivity and Dielectric Function of Strongly Coupled Plasmas," Beiträge aus der Plasmaphys., vol. 25, no. 5, pp. 437–448, 1985.

[121] J. W. Coburn and M. Chen, "Optical Emission Spectroscopy of Reactive Plasmas: A Method for Correlating Emission Intensities to Reactive Particle Density," J. Appl. Phys., vol. 51, no. 6, pp. 3134–3136, 1980.

[122] M. V. Malyshev and V. M. Donnelly, "Diagnostics of Inductively Coupled Chlorine Plasmas: Measurement of Electron and Total Positive Ion Densities," J. Appl. Phys., vol. 90, no. 3, pp. 1130–1137, 2001.

[123] W. M. Yen, S. Shionoya, and H. Yamamoto, "Phosphor Handbook," CRC Press, vol. 23, no. 1, p. 1584, 2007.

[124] K. M. Green, M. Cristina Borrás, P. P. Woskov, G. J. Flores, K. Hadidi, and P. Thomas, "Electronic Excitation Temperature Profiles in an Air Microwave Plasma Torch," IEEE Trans. Plasma Sci., vol. 29, pp. 399–406, Apr. 2001.

[125] M. C. Quintero, A. Rodero, M. C. García, and A. Sola, "Determination of the Excitation Temperature in a Nonthermodynamic-Equilibrium High-Pressure Helium Microwave Plasma Torch," Appl. Spectrosc., vol. 51, no. 6, pp. 778–784, 1997.

[126] S. C. Snyder, L. D. Reynolds, G. D. Lassahn, J. R. Fincke, C. B. Shaw, and R. J. Kearney, "Determination of Gas-Temperature and Velocity Profiles in an Argon Thermal-Plasma Jet by Laser-Light Scattering," Phys. Rev. E, vol. 47, pp. 1996–2005, Mar. 1993.

[127] J. Zalach and S. Franke, "Iterative Boltzmann Plot Method for Temperature and Pressure Determination in a Xenon High Pressure Discharge Lamp," J. Appl. Phys., vol. 113, no. 4, p. 043303, 2013.

[128] X. P. Lu and M. Laroussi, "Electron Density and Temperature Measurement of an Atmospheric Pressure Plasma by Millimeter Wave Interferometer," Appl. Phys. Lett., vol. 92, no. 5, p. 051501, 2008.